Residual stress evaluation in innovative manufacturing techniques: FSW and FDM

LIBERATORIA PER L'ARCHIVIAZIONE DELLA TESI DI DOTTORATO

Al Magnifico Rettore
del Politecnico di Bari

Il/la sottoscritto/a **CAZZATO ALBERTO** nato/a a **GALLIPOLI** il **22/02/1988**

residente a **PRESICCE (LE)** in via **ROMA, 201** e-mail **cazzatoalberto@gmail.com**

iscritto al III° anno di Corso di Dottorato di Ricerca in **INGEGNERIA MECCANICA E GESTIONALE** ciclo **XXIX** ed

essendo stato ammesso a sostenere l'esame finale con la prevista discussione della tesi dal titolo:

RESIDUAL STRESS EVALUATION IN INNOVATIVE MANUFACTURING TECHNIQUES: FSW AND FDM

DICHIARA

1) di essere consapevole che, ai sensi del D.P.R. n. 445 del 28.12.2000, le dichiarazioni mendaci, la falsità negli atti e l'uso di atti falsi sono puniti ai sensi del codice penale e delle Leggi speciali in materia, e che nel caso ricorressero dette ipotesi, decade fin dall'inizio e senza necessità di nessuna formalità dai benefici conseguenti al provvedimento emanato sulla base di tali dichiarazioni;
2) di essere iscritto al Corso di Dottorato di ricerca in **INGEGNERIA MECCANICA E GESTIONALE** ciclo **XXIX**, corso attivato ai sensi del "*Regolamento dei Corsi di Dottorato di ricerca del Politecnico di Bari"*, emanato con D.R. n.286 del 01.07.2013;
3) di essere pienamente a conoscenza delle disposizioni contenute nel predetto Regolamento in merito alla procedura di deposito, pubblicazione e autoarchiviazione della tesi di dottorato nell'Archivio Istituzionale ad accesso aperto alla letteratura scientifica;
4) di essere consapevole che attraverso l'autoarchiviazione delle tesi nell'Archivio Istituzionale ad accesso aperto alla letteratura scientifica del Politecnico di Bari (IRIS-POLIBA), l'Ateneo archivierà e renderà consultabile in rete (nel rispetto della Policy di Ateneo di cui al D.R. 642 del 13.11.2015) il testo completo della tesi di dottorato, fatta salva la possibilità di sottoscrizione di apposite licenze per le relative condizioni di utilizzo (di cui al sito http://www.creativecommons.it/Licenze), e fatte salve, altresì, le eventuali esigenze di "embargo", legate a strette considerazioni sulla tutelabilità e sfruttamento industriale/commerciale dei contenuti della tesi, da rappresentarsi mediante compilazione e sottoscrizione del modulo in calce (Richiesta di embargo);
5) che la tesi da depositare in IRIS-POLIBA, in formato digitale (PDF/A) sarà del tutto identica a quelle **consegnate**/inviate/da inviarsi ai componenti della commissione per l'esame finale e a qualsiasi altra copia depositata presso gli Uffici del Politecnico di Bari in forma cartacea o digitale, ovvero a quella da discutere in sede di esame finale, a quella da depositare, a cura dell'Ateneo, presso le Biblioteche Nazionali Centrali di Roma e Firenze e presso tutti gli Uffici competenti per legge al momento del deposito stesso, e che di conseguenza va esclusa qualsiasi responsabilità del Politecnico di Bari per quanto riguarda eventuali errori, imprecisioni o omissioni nei contenuti della tesi;
6) che il contenuto e l'organizzazione della tesi è opera originale realizzata dal sottoscritto e non compromette in alcun modo i diritti di terzi, ivi compresi quelli relativi alla sicurezza dei dati personali; che pertanto il Politecnico di Bari ed i suoi funzionari sono in ogni caso esenti da responsabilità di qualsivoglia natura: civile, amministrativa e penale e saranno dal sottoscritto tenuti indenni da qualsiasi richiesta o rivendicazione da parte di terzi;
7) che il contenuto della tesi non infrange in alcun modo il diritto d'Autore né gli obblighi connessi alla salvaguardia di diritti morali od economici di altri autori o di altri aventi diritto, sia per testi, immagini, foto, tabelle, o altre parti di cui la tesi è composta.

BARI, 27/02/2017 Firma 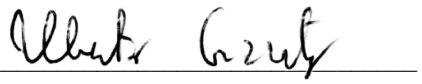

Il/La sottoscritto, con l'autoarchiviazione della propria tesi di dottorato nell'Archivio Istituzionale ad accesso aperto del Politecnico di Bari (POLIBA-IRIS), pur mantenendo su di essa tutti i diritti d'autore, morali ed economici, ai sensi della normativa vigente (Legge 633/1941 e ss.mm.ii.),

CONCEDE

- al Politecnico di Bari il permesso di trasferire l'opera su qualsiasi supporto e di convertirla in qualsiasi formato al fine di una corretta conservazione nel tempo. Il Politecnico di Bari garantisce che non verrà effettuata alcuna modifica al contenuto e alla struttura dell'opera.
- al Politecnico di Bari la possibilità di riprodurre l'opera in più di una copia per fini di sicurezza, back-up e conservazione.

BARI, 27/02/2017 Firma 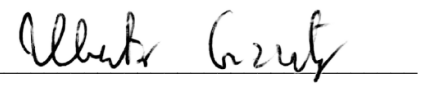

Politecnico di Bari

Department of Mechanics, Mathematics and Management
MECHANICAL AND MANAGEMENT ENGINEERING
Ph.D. Program
SSD: ING-IND/14–MECHANICAL DESIGN AND MACHINE CONSTRUCTION

Final Dissertation

Residual stress evaluation in innovative manufacturing techniques: FSW and FDM

by

Alberto Cazzato

Referees:

Prof. Franco Furgiuele

Prof. Vito Dattoma

Supervisors:

Prof.ssa Caterina Casavola

Dr. Vincenzo Moramarco

Coordinator of Ph.D. Program:

Prof. Giuseppe Pompeo Demelio

XXIX cycle, 2014-2016

Abstract

Nowadays, the speed whereby innovative manufacturing techniques are developed is more and more increasing and new technologies or developments of already existing processes are achieved in a smaller time. Though these innovative technologies have to face and resolve new difficulties and issues related to the novelty of the processes, however, many times they have to tackle old problems known for more than a century.

One of these problems is the residual stresses issue. Residual stresses are “frozen” stresses that exist in materials or structures, essentially due to the manufacturing processes, independently that any external load has been applied on the structure or materials. Combining with the external loads, the effects of residual stresses may be either beneficial or detrimental, depending upon the magnitude, sign, and distribution of the stress.

In this thesis, two innovative techniques in different fields that have to face to residual stress issues have been addressed: Friction Stir Welding and Fused Deposition Modelling.

In the Friction stir welding (FSW), the material is not led to fusion and this helps to decreases the residual stresses values. However, because FSW is mainly a mechanical welding process, due to the high force involved in the weld and, thus, the rigid clamping used, the residual stresses are not low in general. Indeed, the constraints avoid the contraction of the materials during cooling in both longitudinal and transverse directions producing residual stresses.

In the Fused deposition modelling (FDM), the model is built as a layer-by-layer deposition of a feedstock material. Due to this approach, the part cools down layer by layer during the deposition and, consequently, there is thermal variation and different cooling rates from one layer to the other. This produces internal stresses between layers, uneven shrinkage, de-layering problems, warping, and the relatively associated problems especially with large parts.

In order to carry out this study, the two lines of investigation are basically divided as follow.

For residual stress in Friction stir welding, the experimental setup to measure the temperature field on both FSW and LAFSW during the welding process has been developed. This allows to capture the whole temperature fields during the welding process and to study the influence on the temperature of the distance laser spot - FSW tool and of the laser source power. Moreover, the experimental measurements of residual stresses in new developed FSW techniques and materials, i.e. Laser Assisted FSW, the in-process cooled FSW, and lap-joint of aluminium-titanium have been carried out. Finally, the thermographic experimental results and the residual stresses measurements have been employed to validate the numerical models for FSW and LAFSW. These models can predict the temperature and residual stresses changing the process parameters and clamping configuration.

For residual stress in fused deposition modelling, a preliminary study on the mechanical behaviour of FDM parts has been done in order to prove that FDM parts show an orthotropic behaviour on both static and dynamic loads. These studies are useful in order to have a better knowledge of the FDM parts and establish the appropriate behaviour of the material to employ in order to create the numerical model to carry out the residual stress calculation. This model allows to correlate the experimental displacements measured by Electronic Speckle Pattern Interferometry (ESPI) during hole drilling and the residual stresses.

Sommario

Oggi, la velocità con cui vengono sviluppate tecniche di produzione innovative è sempre più crescente e nuove tecnologie o sviluppi di processi già esistenti vengono raggiunti in un tempo minore. Sebbene, queste nuove tecnologie debbano affrontare e risolvere i nuovi problemi e le questioni relative alla novità dei processi stessi, tuttavia molte volte, devono affrontare anche vecchi problemi noti da più di un secolo.

Uno di questi problemi è quello delle tensioni residue. Queste ultime sono stati tensionali "congelati" che esistono in materiali o strutture, essenzialmente a causa dei processi di fabbricazione, indipendentemente che qualsiasi carico esterno sia stato applicato alla struttura o al materiale. Combinandosi con i carichi esterni, gli effetti delle tensioni residue possono essere sia positivi che negativi, a seconda della grandezza, dal segno e dalla distribuzione delle sollecitazioni.

In questa tesi, sono state studiate due tecniche innovative in due diversi campi che devono affrontare i problemi relativi alle tensioni residue: Friction Stir Welding (FSW) e Fused Deposition Modelling (FDM).

Poiché il materiale nella FSW non raggiunge il punto di fusione, si può pensare che i valori delle tensioni residue possano essere bassi. Tuttavia, poiché la FSW è principalmente un processo di saldatura meccanico, a causa delle elevate forze in gioco e delle importanti forze di serraggio utilizzate, le tensioni residue non possono essere considerate basse in generale. Infatti, i vincoli imposti alle piastre da saldare, impediscono la contrazione del materiale durante il raffreddamento generando tensioni residue.

Nella tecnica FDM, il modello è costruito come una deposizione strato per strato del materiale base. A causa di questo approccio, la parte stampata si raffredda strato dopo strato durante la deposizione e, di conseguenza, si creano variazioni termiche e diverse velocità di raffreddamento da un livello all'altro. Questo produce tensioni interne tra gli strati, ritrazione irregolare, problemi di destratificazione, deformazioni e i problemi ad esse associati in particolare con pezzi di grandi dimensioni.

Per effettuare questo studio, le due linee di indagine sono state divise sostanzialmente come segue.

Per quanto riguarda le tensioni residue nella saldatura FSW, è stato sviluppato il setup sperimentale per misurare il campo di temperatura durante il processo di saldatura sia nella FSW e che nella Laser Assisted FSW. Questo permette di avere una mappa di temperatura a campo intero durante il processo di saldatura. Questo ha permesso di studiare l'influenza sulla temperatura della distanza spot laser – utensile FSW e della potenza della sorgente laser. Inoltre, sono state effettuate le misure sperimentali delle tensioni residue in nuove tecniche derivate dalla FSW e in nuovi materiali per la FSW, cioè LAFSW, l'in-process cooled FSW e giunti a sovrapposizione alluminio-titanio. Infine, i risultati sperimentali termografici e della misura delle tensioni residue sono stati impiegati per validare i

modelli numerici per FSW e LAFSW. Questi modelli sono in grado di prevedere la temperatura e le tensioni residue cambiando i parametri di processo e il setup dei vincoli.

Per quanto concerne le tensioni residue nella FDM, è stato eseguito prima uno studio preliminare sul comportamento meccanico dei pezzi FDM al fine di dimostrare che questi mostrano un comportamento ortotropo sia a carichi statici che dinamici. Questi studi sono stati utilizzati al fine di avere una migliore conoscenza delle parti FDM e stabilire il comportamento appropriato da impiegare al fine di creare il modello numerico per eseguire il calcolo delle tensioni residue. Questo modello permette di correlare gli spostamenti sperimentali misurati dall'Electronic Speckle pattern Interferometry (ESPI) durante la foratura e le tensioni residue.

Contents

List of Figures

List of Tables

1. Introduction

Nowadays, the speed whereby innovative manufacturing techniques are developed is more and more increasing and new technologies or developments of already existing processes are achieved in a smaller time. Though these innovative technologies have to face and resolve new difficulties and issues related to the novelty of the processes, however, many times they have to tackle old problems known for more than a century.

One of these problems is the residual stresses issue. Residual stresses are “frozen” stresses that exist in materials or structures, essentially due to the manufacturing processes, independently that any external load has been applied on the structure or materials. Combining with the external loads, the effects of residual stresses may be either beneficial or detrimental, depending upon the magnitude, sign, and distribution of the stress.

Many catastrophic accidents in the history, such as bridge and ship failure, are due to the residual stresses issue in direct manner or in phenomenon related to these. For example, probably, they were a factor in the collapse of the Silver Bridge in West Virginia, United States in December 1967 or in the failure of Liberty Ship "Schenectady" of United States that suddenly broke in two in January 1943.

1.1. Motivation of the research

In the present thesis, two innovative techniques in different fields that have to face to residual stress issues will be addressed: Friction Stir Welding and Fused Deposition Modelling.

The Friction stir welding (FSW) has been developed by The Welding Institute (TWI) in 1991 and nowadays it has become an important welding technique to join materials that are difficult to weld by traditional fusion welding technology. This relevant characteristic is due to the nature of solid-state welding process of FSW. Indeed, the material is not led to fusion and the joint is the result of the rotation and movement along the welding line of the tool that causes softening of material due to frictional heat and the stirring of the same. In FSW, the temperature does not reach the fusion value of the materials and this helps to decreases the residual stresses values. However, due to the higher force involved in the weld and, thus, the rigid clamping used, the residual stresses are not low in general in this technique. The constraints avoid the contraction of the materials during cooling in both longitudinal and transverse directions, thereby resulting in generation of longitudinal (parallel to welding direction) and transverse stresses (normal to welding direction). As the presence of high residual stress values influence the post-weld mechanical properties, e.g. fatigue properties, it is really important to investigate the residual stress distribution in the FSW welds.

The Fused deposition modelling (FDM) is an additive rapid prototyping process invented by S. Scott Crump co-founder of Stratasys Inc. in 1989. In this process, the model is built as a layer-by-layer deposition of a feedstock material. Due to this approach, it is possible to build a part with almost any shape, both internal and external. Though the layer-by-layer deposition is a plus for FDM technique, it should be considered that the part cools down layer by layer during the deposition and, consequently, there is thermal variation and different cooling rates from one layer to the other. This produces internal stresses between layers, uneven shrinkage, de-layering problems, warping, and the relatively associated problems especially with large parts. Often the warpage can prevent the finalization of the objects due to unsticking problems from the bed. Consequently, it is of great importance to study the residual stress in FDM in order to solve the related problem and in view to determine the correct parameters for the FDM process.

1.2. Objectives and proposed research topics

As discussed in the previous section, the main research objective is the study of the residual stress in two innovative manufacturing techniques: friction stir welding and fused deposition modelling. In order to carry out this study, the two lines of investigation are basically divided as follow:

1. Residual stress in Friction stir welding:
    - Develop of the experimental setup to measure the temperature field on both FSW and LAFSW during the welding process;
    - Study of the influence on the temperature of the distance laser spot - FSW tool and of the laser source power;
    - Development of the FSW and LAFSW numerical models that can predict the temperature and residual stresses. Validation of these models on the basis of the thermographic experimental results and residual stress measurements;
    - Study, through the numerical model, the influence of the clamps configuration on residual stresses in FSW;
    - Experimental measurements of residual stresses in new developed techniques and materials, i.e. Laser Assisted FSW, the in-process cooled FSW and lap-joint of aluminium-titanium.
2. Residual stress in Fused deposition modelling:
    - Preliminary study on the mechanical behaviour of FDM parts. This is divided into two main section. In the first, the Classical Laminate Theory (CLT) is employed to describe the FDM parts behaviour, in the second, a study on tensile-impact of FDM specimens is carried out. The final aim is to prove that FDM parts show an orthotropic behaviour on both static and dynamic loads. These studies are useful in order to have a better

knowledge of the FDM parts and establish the appropriate behaviour of the material to employ in the residual stress calculation;

- Development of the numerical model that correlate the experimental displacements measured by Electronic Speckle Pattern Interferometry (ESPI) during hole drilling and the residual stresses;
- Measurement of the residual stress in FDM parts employing the hole-drilling method.

1.3. Chapters Abstracts

The thesis consists of nine chapters. The next chapter contains an overview of residual stresses and summed up the techniques to carry out the measurements. A deep explain will be done for the two experimental methods employed in this thesis: X-Ray diffraction and hole-drilling method combined with ESPI. Chapter 3 is an introduction to Friction stir welding process. The main characteristics, process parameters, advantages, shortcomings and improvements of FSW will be explain in this chapter. The experimental setup to measure the temperature fields and the numerical models for the prediction of the temperatures will be presented in chapter 4. The core of FSW residual stress measurements of this thesis will be presented in chapter 5 and prediction will be reported in chapter 6. In chapter 5, the experimental results on the measurements in Laser Assisted FSW, Al-Ti FSW lap joint and in the in-process cooled FSW will be presented.

In chapter 6, the presentation of FSW and LAFSW numerical model to predict residual stresses will be done. In addition, a study of the residual stress variation due to the change of the clamping configuration will be carried out.

The part of this thesis that concern the FDM will be opened by the chapter 7. In this, the main characteristics, process parameters, materials, advantages and shortcomings will be presented. In chapter 8, a preliminary study on the mechanical behavior of FDM parts both on static and dynamic loads will be presented. This study is necessary in order to have a better comprehension of the mechanical behavior that will be used in the numerical model explained in the following chapter 9. In this beyond the numerical model presentation, the experimental setup to calculate the residual stress through the hole-drilling and the results of the measurements will be presented. The dissertation will be concluded in chapter 10, where a summary of the results will be made.

2. Residual stresses: an overview

Residual stresses are “frozen” stresses that exist in materials or structures independently that any external load has been applied on the structure or materials [1]. These stresses are self-equilibrating and thus, the local tensile and compressive areas sum to create zero force and moment resultants within the whole volume of the material or structure. Combining with the external loads, the effects of residual stresses may be either beneficial or detrimental, depending upon the magnitude, sign, and distribution of the stress.

In this chapter an overview of the residual stresses issues and measurement techniques has been reported. The chapter starts from the definition and the origins of residual stress and continue with a review of all the traditional and innovative measurement techniques. A deeper presentation has been reported for the residual stresses techniques employed in this work: hole drilling and X-Ray diffractometry.

2.1. Definition of residual stresses

The residual stresses are those stresses that remain in a material after manufacturing processes in absence of external forces or thermal gradients. Residual stresses are classified by the length scale over which they equilibrate [2] (Figure 2.1). Type I are macro residual stresses that extend over distances larger than the grain size. These are the common residual stresses that appear in manufactured components. Type II are micro residual stresses that extend between grains. The Type I stresses is one of the cause of Type II micro-stresses. Finally, Type III are residual stresses that occur at the atomic scale around dislocations and crystal interfaces. Types II and III are often grouped together as micro-stresses. The Type I macro stresses are the target of most of the measurement techniques presented in this chapter, though, for some of the diffraction methods, the presence of Type II stresses can influence the measure of the Type I stresses.

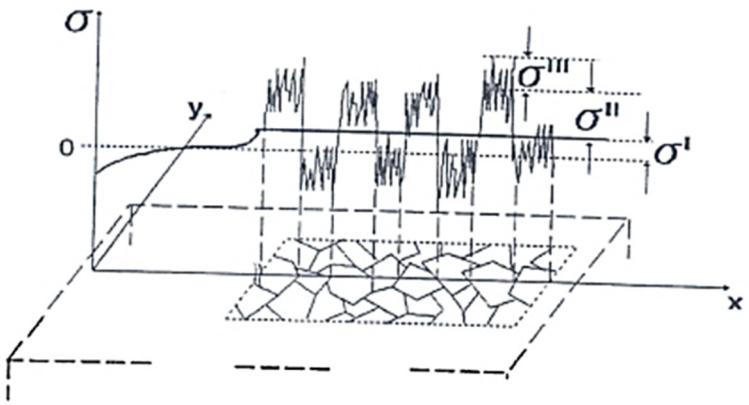

Figure 2.1 Type I, II and III categorizations of residual stresses [3]

It is also important to consider the concept of the characteristic volume in residual stresses measurements. This can be used to describe the volume over which a given type of residual stress

averages to zero. Most material removal techniques, e.g. hole drilling, remove large volumes of material over which Type II and III stresses average to zero. In these techniques, only the macro residual stresses can be measured [4]. In conclusion, comparing results from different techniques, the issue of the sampling volume and spatial resolution of each measurement method in relation to the type of residual stress being measured should be considered (Figure 2.2).

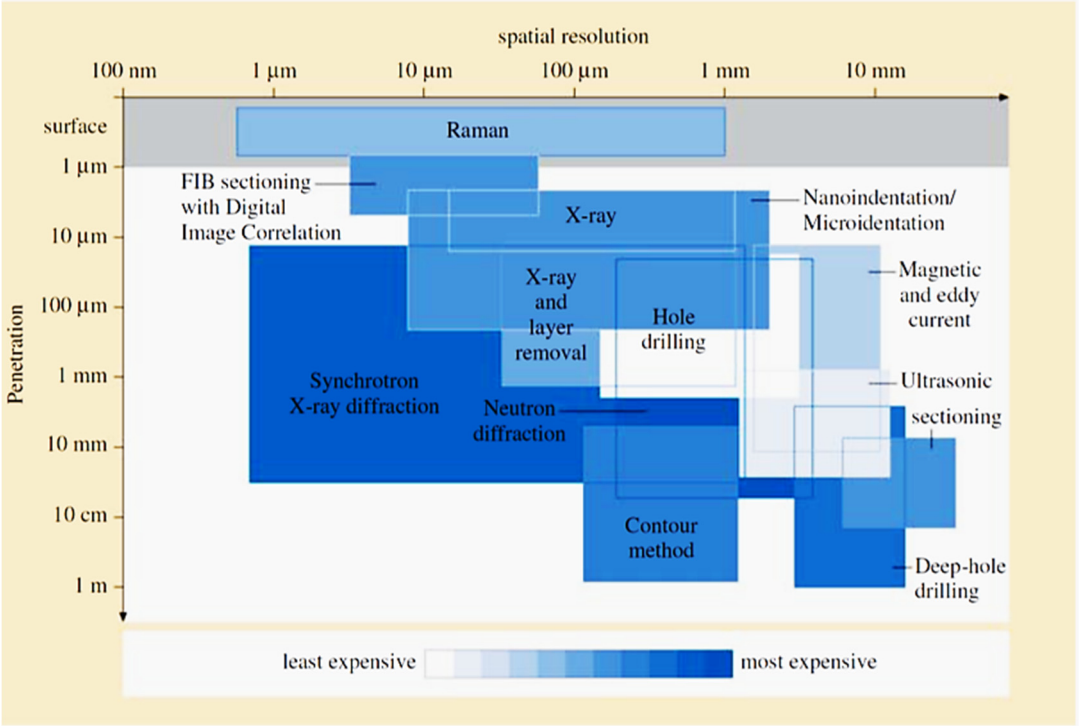

Figure 2.2 Penetration vs. spatial resolution for various residual stress measurement methods [5]

2.2. Origins of residual stresses

Residual stresses are developed during almost all manufacturing processes that involve material deformation, heat treatment, machining or processing. Further, stresses can also develop during the life of the component as an elastic response to incompatible local strains within the component, for example, due to non-uniform plastic deformations. The surrounding material must then deform elastically to preserve dimensional continuity, thereby creating residual stresses [5]. The origins of residual stresses in a component can be classified as:

- Mechanical

These residual stresses are the result of manufacturing processes that produce non-uniform plastic deformation. For example, in manufacturing processes that change the shape of a material such as forging, rolling, bending, drawing and extrusion. Moreover, they can be generated also in service during surface deformation, as in ball bearings and railway rails. In some cases, they can be introduced deliberately to develop a particular stress profile, usually compressive, in a component (shot peening, toughening of glass or cold expansion of holes).

- Thermal

Thermally generated residual stresses are the consequence of non-uniform heating or cooling operations. Examples occur in manufacture during welding, casting, quenching. In particular, the quenching of steel or aluminum alloys leads to surface compressive stresses, balanced by tensile stresses in the inner core of the component.

- Chemical

Material phase transformation, density changes, precipitation can develop residual stresses in the materials. Examples occur in chemical surface treatments, coatings, precipitation hardening in alloys and polymerization in plastics [4]

The magnitude of the residual stresses can be sufficiently large to cause local yielding and plastic deformation and can severely affect component performance. Moreover, because of their self-equilibrating character, the presence of residual stresses may not be apparent and so they may be ignored during engineering design [6]. However, in terms of material strength, the residual stresses are as an addition to the external loading stresses. Therefore, the contribution of the residual stresses can be beneficial or harmful, dependent on the sign and location of the residual stresses. For example, tensile residual stresses in the surface of a component are generally undesirable since they can contribute to fatigue failure and stress-corrosion cracking. Instead, compressive residual stresses in the surface layers are usually beneficial. This is because in fatigue life, the failure mechanism is by crack growth and most cracks are at the surfaces level. Thus, the compressive residual stresses act to bias the loading stresses towards compression and avoid the crack growing.

For this reasons, it is a big issue the knowledge of the internal stress state that it have to be deduced from measurements or modelling predictions [4].

2.3. Measurement techniques

In general, the measure of stresses cannot be carried out directly on the component. The measurements are indirect and a proxy such as strain or displacement is measured, from which stresses are interpreted. The “locked-in” character of residual stress makes the problem more complicate because the residual stresses must be relieved in some way that the sensor can register the change in strain or displacements [6]. For example, in the techniques reported in section 2.3.1, 2.3.3 and 2.3.7, the residual stresses are relieved removing the material containing those residual stresses. The procedure creates the complication that the stress-containing material is destroyed and the measurements must therefore be made on the adjacent remaining material. This separation between residual stresses and measurement locations creates mathematical issues that require specialized stress evaluation methods [7, 8].

The non-destructive measurement techniques, described in Sections 2.3.4, 0 and 2.3.6, avoid material removal and thus, a comparison between some characteristics of the material in the actual configuration and the same characteristics in a known "stress-free" reference allows carrying out the measurements. Achieving such reference states can be quite challenging to do reliably.

A consequence of all these challenges is that measurements of residual stresses do not typically reach the accuracy or reliability possible when working with applied stresses. However, the various residual stress measurement methods are now quite mature and the accuracy gap is often not very large.

Nowadays, a wide variety of residual stresses measurement techniques has been developed. The following sections give some basic information about the techniques explaining the advantages and the issues of each technique.

2.3.1. Hole drilling

The hole-drilling method is the most widely used technique for measuring residual stresses in materials. It is convenient to use, it is standardized (ASTM E837 [9]), relatively simple, and quick, it has good accuracy and reliability. The method is considered as "semi-destructive" because the test procedure involves some damage to the specimen but the damage is often tolerable or repairable.

The principle of the hole-drilling method involves drilling a small hole in the sample where the residual stresses have to be evaluated. This removal of material causes the redistribution of the residual stresses around the hole and, consequently, the deformation of the surface near the hole. The Figure 2.3 illustrates the deformations around a hole drilled into material with tensile residual stresses.

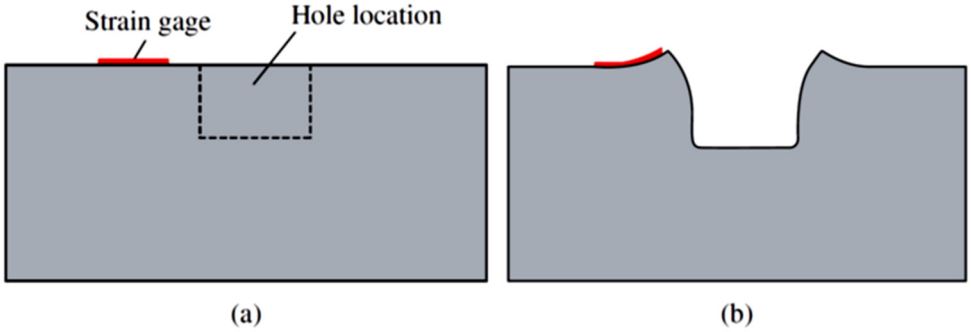

Figure 2.3 Cross-sections around a hole drilled into tensile residual stresses. (a) Before and (b) After [10]

The deformation of the surface area near the hole can be quantify using strain gage or optical techniques (i.e. Electronic Speckle Patter Interferometry). From these deformations and employing formulae and calculations derived from experimental and Finite Element Analysis, the residual stress can then be calculated.

In practical terms, a hole is drilled in the sample at the centre of a strain gauge rosette (Figure 2.4). Hole-drilling rosettes typically contain three radial strain gages arranged in rectangular format (0° − 45° − 90° or 0° − 135° − 270°) to identify the three in-plane stress components σ_x, σ_y and τ_{xy}. The Figure 2.4 shows a range of residual stress strain gauge rosette geometries currently available. Type A is a general-purpose design appropriate for most measurement needs. Type B, having all three strain gages placed on the same side of the hole location, is useful for making measurements near to an obstacle. However, this rosette pattern should be used only for this purpose because this pattern increases the sensitivity to hole eccentricity errors. The last one, the type C rosette, is a design useful to measure small residual stresses having six strain gauges.

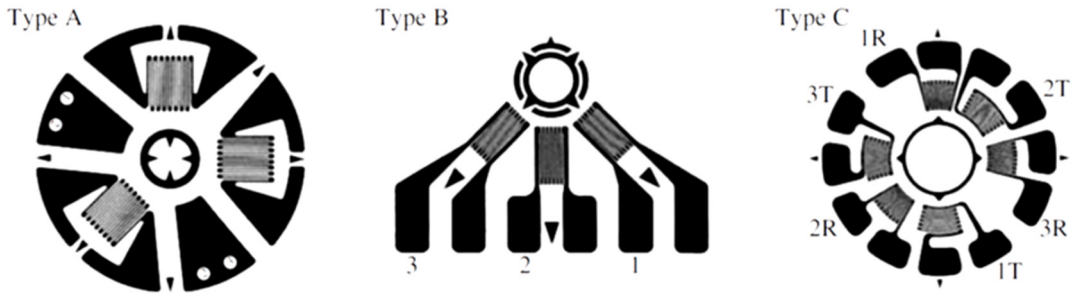

Figure 2.4 Typical commercially available hole drilling gauge geometries [9]

Modern strain gages can carry out accurate and stable strain measurements, which is an essential feature because hole-drilling strains tend to be small, typically low hundreds of micro-strains, sometimes less than one hundred. These issues related to potential errors and uncertainties on the dimensions of the hole (concentricity and diameter) and specimen preparation can affect the residual stress calculation.

Early hole-drilling measurements were used to identify uniform stresses but, nowadays, the availability of finite element calculations enables accurate stress profile measurements using the incremental hole-drilling method [7]. However, in practical terms, there are great issues making measurements beyond a depth equivalent to the drill diameter, because no additional strain can be measured in a reliably way. Moreover, the basic hole drilling analysis assumes that the material is isotropic, linear elastic and the residual stress values do not exceed half the yield strength of the material.

Despite some issues, the hole drilling technique is the most employed technique to measure the residual stresses in materials. In recent years, the base technique continues to be developed including the introduction of new rosette designs and the development of full field measurements techniques (electronic speckle pattern interferometry, Moiré interferometry, and holography) [11-14].

In this work, the hole drilling method has been employed in combination with ESPI to measure the residual stresses, in the next section a brief overview of the use of ESPI and hole-drilling will be presented.

2.3.2. Hole drilling and ESPI

In the last years, several optical techniques have been introduced as an alternative to strain gauge rosette in surface deformation measurement due to the hole-drilling method. Camera-based optical techniques have the advantage to carry out full-field measurements with very high sensitivity, to provide a stronger statistic, to eliminate error due to hole eccentricity and, finally, to reduce the cost of the single test. Instead, strain gages provide strain measurements in only three discrete areas. The Figure 2.5 compares the localized information provided by strain gages (the three-square areas) and the richer information available from full-field displacement measurements.

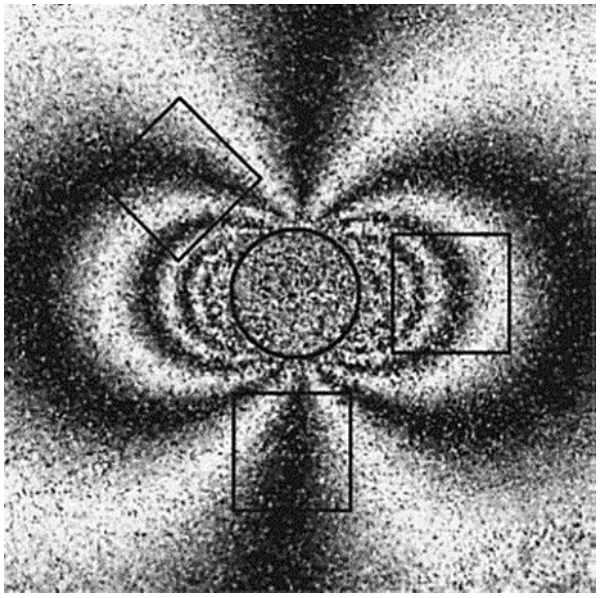

Figure 2.5 Comparison of strain gage and full-field ESPI data [10]

Roughly three optical techniques that have been applied to hole drilling residual stress measurements, i.e. Moiré Interferometry, Digital Image Correlation (DIC) and Electronic Speckle Pattern Interferometry (ESPI). Among these, the latter is the most interesting because it can work with a plain specimen surface, without attachment of the diffraction grating needed for Moiré measurements or paint the surface as in DIC. The main drawback of this technique is the necessity to isolate the system from vibrations in order to obtain fringe pattern with good contrast. In Figure 2.6 the experimental setup for ESPI measurements in hole drilling method has been reported.

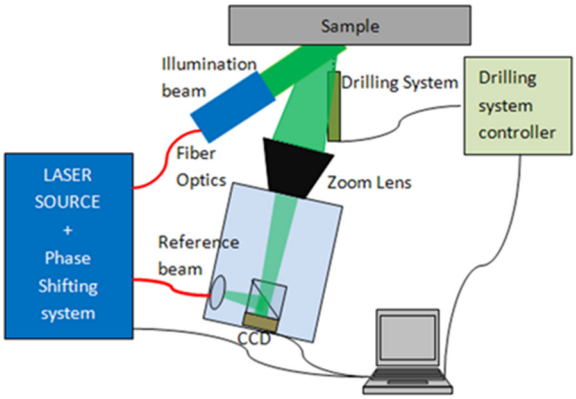

Figure 2.6 Scheme of experimental setup for ESPI measurements in hole drilling method

In the setup, a diode pumped solid-state laser source shines the sample and generates the speckle pattern. The laser beam is divided in two parts by a beam-splitter and delivered to two optical fibres. The beam emerging out from the first fibre is collimated and then directed towards the sample at a given angle. The beam emerging from the second fibre, instead, is directed towards the CCD matrix of the camera and acts as a reference beam. The CCD camera itself is placed at a given angle with respect to the normal to the sample. Light diffused by the sample interferes on the CCD matrix with the reference beam.

In order to obtain the phase, a four-step temporal phase shifting algorithm is adopted [15, 16]. This means that four reference images are taken initially having a $\pi/2$ phase difference among each other. Another set of four images is, analogously taken for each drill increment. These intensity patterns are subtracted from the reference intensity pattern recorded on the sample before starting the drilling procedure. This operation allows obtaining fringe patterns encoding the information about the displacement experienced by the sample along the sensitivity vector.

Employing the integral method [7] and the displacement data, the residual stresses in the materials at each drill increment can be calculated. In chapter 0 a deeper explanation on how to relate the experimental displacements and the residual stresses will be carried out.

2.3.3. Ring coring

The ring-core method is very similar to the hole-drilling method but the measurement area is the inner part of an annular groove. Figure 2.7 compares the geometry of the hole drilling and ring-core methods. The two methods are mathematically identical but the only differences are in the numerical constants used for the residual stress evaluations. Compared to the hole drilling method, the ring-core has the advantage of producing larger relieved strains and has a better capability to measure very large residual stresses. However, the hole-drilling method is the more commonly used procedure because it is easier to use and damage the specimens less than the ring-core method [5].

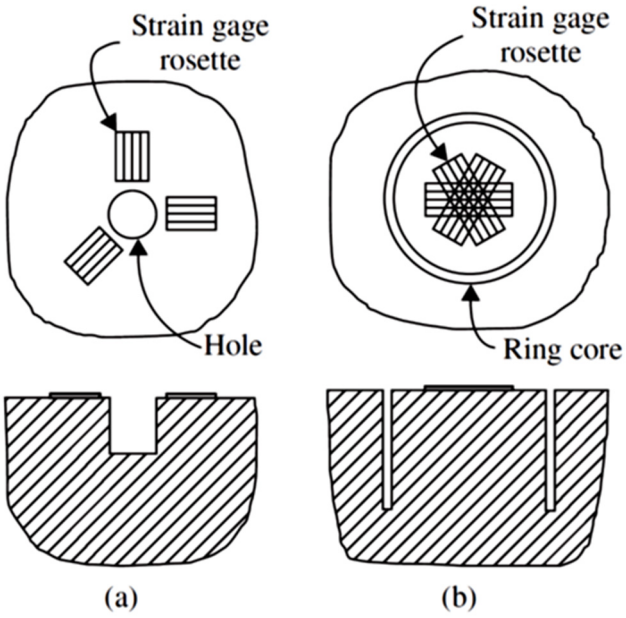

Figure 2.7 Comparison between (a) Hole drilling and (b) ring-core [10]

2.3.4. X-Ray diffraction

The X-ray diffraction (XRD) can be considered as non-destructive technique to measure, basically, surface stresses. It can be combined with chemical layer removal technique in order to measure a stress profile within the materials. In this case, the method becomes destructive. The main issue in XRD is the limitation imposed on the test piece size and geometry. The size can be a problem, because the entire part must fit into the diffractometer (Figure 2.8). In addition, the geometry has to be such that an X-ray can both hit the measurement area and the detector without hitting obstructions.

Figure 2.8 Example of commercial diffractometer for residual stress measurements

The XRD measures the strain in the crystal lattice and determines the associated residual stress from the elastic constants assuming a linear elastic distortion of the appropriate crystal lattice

plane [17]. Diffraction of X-rays occurs when the radiation interacts with atoms that are arranged in a regular array, i.e. in crystals. The radiation is absorbed and then reradiated with the same frequency such that strong emissions occur at certain orientations and minimal emissions at other orientations. The angles at which the strong emissions occur are described by Bragg's Law:

$$n\lambda = 2d \sin\theta \tag{2.1}$$

where n is an integer, λ is the wavelength of the electromagnetic radiation, d is the distance between the diffracting planes (inter-atomic lattice spacing) and θ is the Bragg angle [5]. The Figure 2.9 illustrates the quantities shown in equation 2.1.

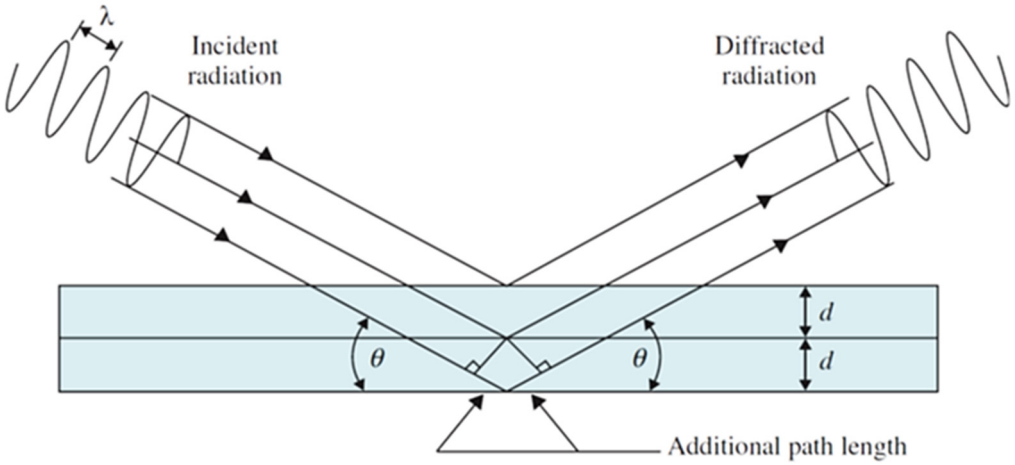

Figure 2.9 Radiation diffraction within a crystal structure [5]

The equation 2.1 shows the relationship between the diffraction pattern and the inter-planar spacing within the material. When there is the presence of residual stresses in the material, elongations and contractions are produced within the crystal lattice changing the inter-planar spacing from the stress-free value. These changes in *d* can be measured as a shift in the diffraction pattern. Measuring this shift, the change in the inter-planar spacing can be evaluated and thus the strain within the material can be calculated [17].

In the XRD method, the X-radiation only penetrates a few microns. Due to this small penetration depth, the assumption that the stress normal to the surface is zero can be done, i.e. the volume under investigation can be considered in a state of plane stress. This condition allows the simplification of the stress-strain equations and there is no need for a precise determination of the unstressed lattice plane dimension.

In the following part of this section, a brief summary of the mathematical background to determine the residual stresses by XRD has been reported. The orthogonal coordinate systems used in the following explanations are defined in Figure 2.10.

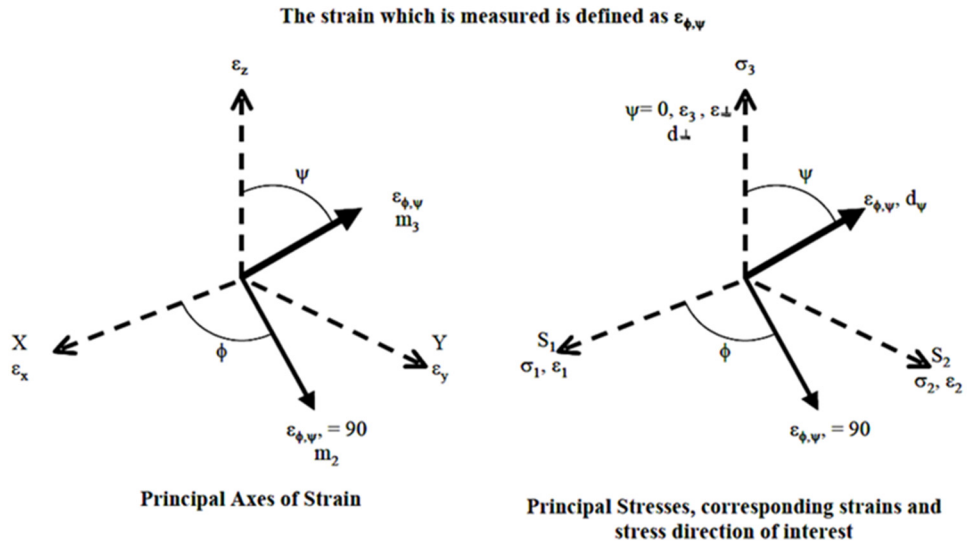

Figure 2.10 Coordinate system used for calculating surface strain and stresses where ε_z and σ_3 are normal to the specimen surface [17]

Though σ3 = 0 because the measurement is carried out on the surface, the strain ε_z does not equal to zero. This strain ε_z can be experimental evaluated by measuring the peak position 2θ, and solving equation 2.1 for a value of d_n. Knowing the unstrained inter-planar spacing d_0 then ε_z can be calculated as:

$$\varepsilon_z = \frac{d_n - d_0}{d_0} \tag{2.2}$$

Thus, the strain within the surface of the material can be measured by comparing the unstressed lattice inter-planar spacing (obtained by a measurement on the non-deformed material) with the strained inter-planar spacing. Equation 2.2 provides the expression of ε_z for measurements performed normally to the surface. By altering the tilt of the specimen within the diffractometer, measurements of planes at an angle ψ can be made (Figure 2.11) and thus the strains along that direction can be calculated using:

$$\varepsilon_{\varphi\psi} = \frac{d_{\varphi\psi} - d_0}{d_0} \tag{2.3}$$

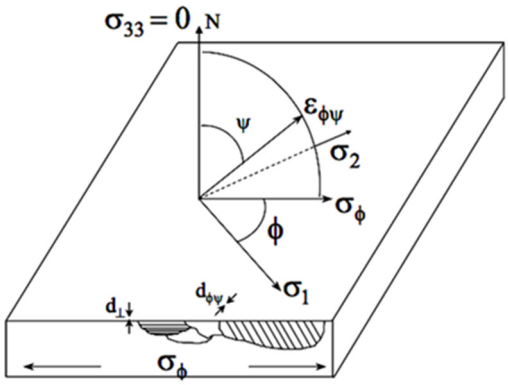

Figure 2.11 Schematic showing diffraction planes parallel to the surface and at an angle φψ [17]

The Figure 2.11 illustrates how planes that are angled than the surface are measured by tilting the specimen so that the planes are brought into a position where they satisfy Bragg's Law.

However, usually it is more useful to know the engineering stresses that are linked to previous calculated strains. From Hooke's law:

$$\sigma_y = E\varepsilon_y \tag{2.4}$$

However, a tensile force producing a strain in the X-direction produces also strains in the transverse directions. Assuming that the stresses are biaxial, then the ratio of the transverse to longitudinal strains is Poisson's ratio, ν:

$$\varepsilon_x = \varepsilon_y = -\nu\varepsilon_z = \frac{-\nu\sigma_y}{E} \tag{2.5}$$

assuming that $\sigma_z = 0$ then:

$$\varepsilon_z = -\nu(\varepsilon_x + \varepsilon_y) = -\frac{\nu}{E}(\sigma_x + \sigma_y) \tag{2.6}$$

combining equations 2.2 and 2.6

$$\frac{d_n - d_0}{d_0} = -\frac{\nu}{E}(\sigma_x + \sigma_y) \tag{2.7}$$

In equation 2.7, only the sum of the principal stresses can be obtained, and however, the precise value of d_0 is still required. In order to measure a single stress acting in some direction in the surface σ_φ, the elasticity theory for an isotropic solid can be applied and the strain along an inclined line (m_3 in Figure 2.10) is

$$\varepsilon_{\varphi\psi} = \frac{1+\upsilon}{E}(\sigma_1 \cos^2\varphi + \sigma_2 \sin^2\varphi)\sin^2\psi - \frac{\nu}{E}(\sigma_1 + \sigma_2) \tag{2.8}$$

considering the strains in terms of inter-planar spacing and using the strains to evaluate the stresses:

$$\sigma_\varphi = \frac{E}{(1+\nu)\sin^2\psi}\left(\frac{d_\psi - d_n}{d_n}\right) \tag{2.9}$$

This equation allows to calculate the stress in any chosen direction from the inter-planar spacing employing two measurements: one carried out in a plane normal to the surface and the other in the plane containing the direction of the stress to be measured.

Several methods can be used to evaluate the stresses within a material using this diffractometer technique but the most commonly used method is the $\sin^2\psi$ method. This has the advantage that inclined measurements are made at a number of ψ tilts (Figure 2.10) rather than at only one. The inter-planar spacing, or 2θ peak position, is measured and plotted as a curve similar to that shown in Figure 2.12. Starting from this, the stress is derived from the slope of the line and using some basic knowledge of the elastic properties of the material. Thus, the stress is given by:

$$\sigma_\varphi = \left(\frac{E}{1+\nu}\right)m \tag{2.10}$$

where m is the slope of the d vs. $\sin^2\psi$ curve and assumes a zero stress at $d = d_n$ [18, 19].

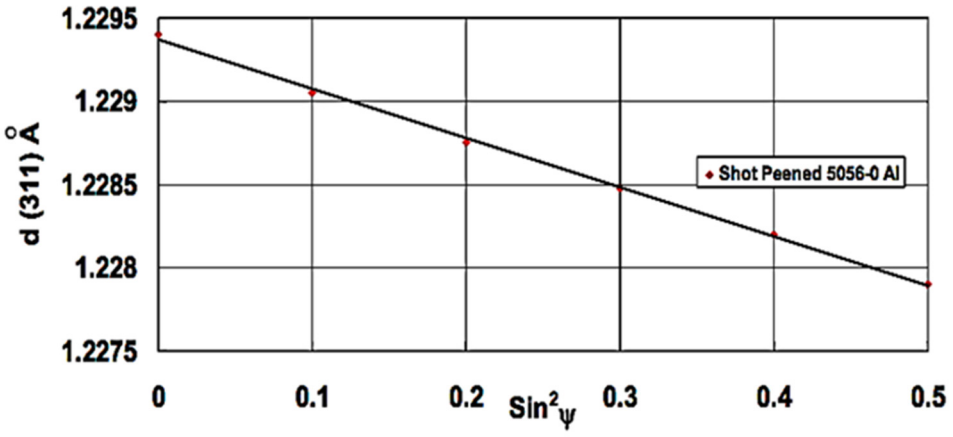

Figure 2.12 Example of a d vs $\sin^2\psi$ plot [17]

Solutions that are more complex exist for non-ideal situations where, for example, there is the presence of shear stresses or an inhomogeneous stress state within the material (Figure 2.13). Such solutions are available in the commercial software packages.

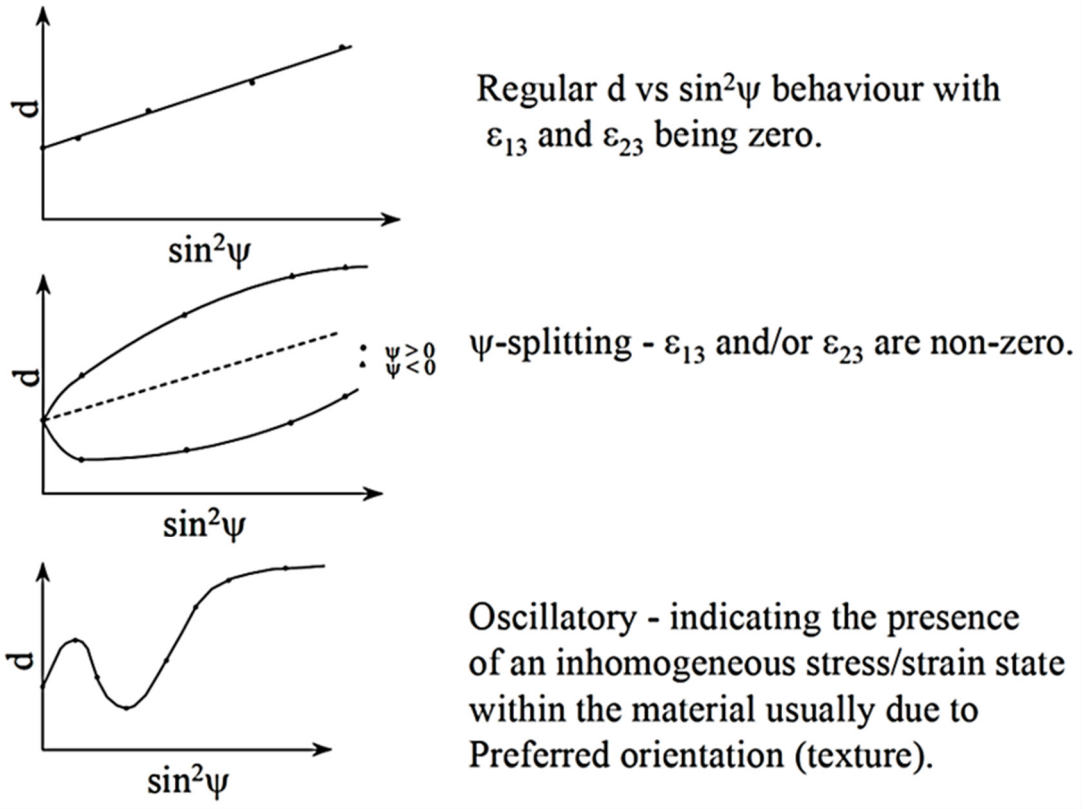

Figure 2.13 Further examples of d vs $\sin^2\psi$ plots [17]

2.3.5. Synchrotron X-ray diffraction

As XRD also this method employs X-rays as the traditional XRD method, however, the X-rays are much higher energy and, consequently, they penetrate much deeper into the materials. Typically, the X-Ray can reach around 50 mm in aluminium [20, 21]. Because the higher energy

radiation penetrates many tens or even hundreds of mm into a material, the stress condition cannot be considered under plane stress, as in XRD, and the full three-dimensional stress condition must be considered. Thus, strain is determined by subtracting the unstressed lattice parameter from the actual stressed parameter. This issue results in the necessity for the unstressed lattice parameter to be precisely known and, usually, this requirement can introduce significant uncertainty into the strain measurement. This is because the unstressed lattice parameter can be affected by many material parameters such as, alloy content, phase composition and other factors.

Despite this issue and the other limitations that are the same of neutron diffraction (see section 2.3.6), the measurement is quicker than conventional X-ray diffraction. With measurements times of a fraction of a second, it is possible to obtain detailed strain maps of components in few hours of beam time [4].

2.3.6. Neutron diffraction

Neutron diffraction (ND) uses penetrating radiation as the previous described diffraction methods, however, neutrons have a very large penetration depths. Neutron diffraction can carry out measures of the elastic strains induced by residual stresses throughout the thickness in the 0.1−1.5 m range with a spatial resolution less than one millimetres. Such capabilities allow the measurement of residual stresses inside of components without the necessity of sectioning or layer removal. However, the accuracy of ND techniques requires that the unstressed lattice spacing of the measured crystallographic planes be precisely known since the stress state is tri-axial at depth. As for the synchrotron method, the unstressed lattice spacing at the point of strain measurement must be known but is not easily measured. Additional limitations are that each strain measurement requires several minutes to over an hour, a single stress determination in one small gage volume of the component (one mm^3) requires at least three strain measurements, and the measurements are very expensive.

However, this method with the capacity to carry out measures over the whole surface and depth has made neutron diffraction a particularly useful technique for the validation of theoretical and numerical models [5].

2.3.7. Curvature and layer removal

The curvature and layer removal techniques are a relatively easy technique that is often used to measure the residual stresses in a specimen with simple geometries. When some layers are removed from a flat plate containing residual stresses, the plate starts to bend because the stresses become unbalanced. Clearly, the curvature depends from the original residual stresses distribution present in the removed layers and from the elastic properties of the remained plate. Measuring the curvature after successive layer removals, the distribution of the stresses in the original plate can then be calculated.

Many techniques can be employed in order to measure the curvature of the specimen, such as optical techniques, laser scanning and strain gauges. Layer removal is applicable only to plate samples and is suitable for measuring in-bulk macro-stress measurements. Stresses at or very near the surface cannot be measured by this technique [4].

2.3.8. Magnetic methods

The most widely known and applied magnetic residual stress measurement method is the Magnetic Barkhausen Noise (MBN) [22]. As the ferromagnetic properties of steels and other ferromagnetic materials are sensitive to the internal stress state the MBN can be related to residual stress state. The MBN analysis involves measuring the number and magnitude of magnetic re-orientations made by the magnetic domains in a ferromagnetic material during magnetization reversal. These reorientations are observed as pulses that are random in amplitude, duration, and temporal separation therefore roughly similar to a noise. Though most steels and some ceramics are ferromagnetic and produce MBN, many engineering materials are not ferromagnetic and so MBN is not applicable to them. Moreover, the MBN technique has a limited range of stress sensitivity (roughly ±300 MPa) and a few millimetres depth of measurement [5].

The sensitivity of this technique to other properties of metallic materials has consequently the need for calibration with a nearly identical specimen. This issue severely compromises the reliability, accuracy, and applicability of MBN technique [5].

2.3.9. Ultrasonic methods

The ultrasound acoustic methods have the possibility to determine material properties such as crystallographic orientation, grain size, phase composition, and stresses. For the latter, the velocity of some mode of ultrasonic wave is measured. However, the velocity of ultrasound is not only related to stresses, but also, to many other micro-structural characteristics such as grain size, crystallographic texture, and so on. The effect of these other characteristics compromises the accuracy of ultrasonic stress measurement method. However, they have the advantage of being able to measure in the bulk of the material and are therefore well suited to routine inspection operations. Additionally, the instrumentation is portable and quick to implement and to carry out the measure [4].

3. Friction Stir Welding: background and state of the art

3.1. General background

Friction stir welding (FSW) has been developed by The Welding Institute (TWI) in 1991 and nowadays it has become an important welding technique to join materials that are difficult to weld by traditional fusion welding technology [23]. This relevant characteristic is due to the nature of solid-state welding process of FSW. In fact, the material is not led to fusion and the joint is the result of the rotation and movement along the welding line of the tool that causes softening of material due to frictional heat and the stirring of the same. The basic concept of FSW is remarkably simple. A non-consumable rotating tool with a specially designed pin and shoulder is inserted into the edges of sheets or plates to be joined and traversed along the line of joint (Figure 3.1).

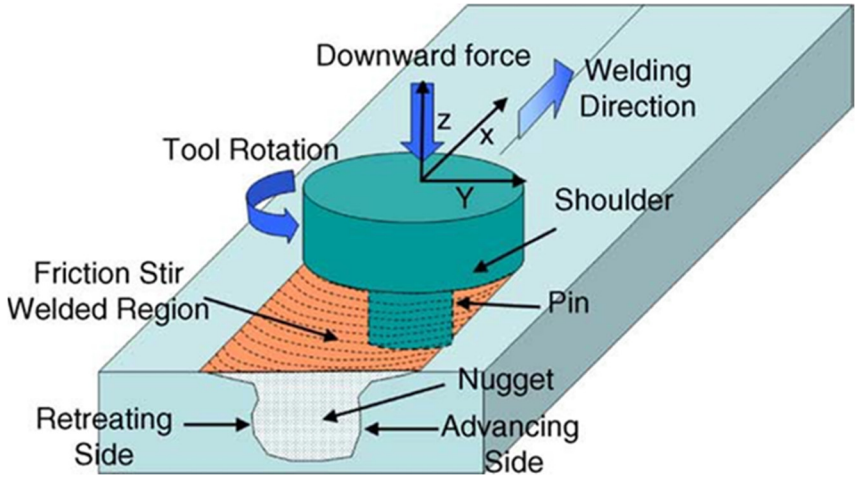

Figure 3.1 Scheme of friction stir welding process [23]

During FSW process, the material undergoes a severe plastic deformation at elevated temperature. This generates a fine and equiaxed recrystallized grains structure that produces good mechanical properties [23-25]. Recently, this characteristic of create fine grains has been employed in order to deliberately develop microstructural modifications in a monolithic workpiece. This technique is known as friction stir processing (FSP) and has been developed by Mishra et al. [26, 27]

FSW is considered as the most important development in metal joining in the last years and it can be considered as a ‘‘green’’ technology. Indeed, FSW consumes less energy compared to the conventional welding techniques, e.g., it requires only 2.5% of the energy needed for a laser weld. Moreover, no cover gas, flux and filler metal are used making the process environmentally “green” and friendly [23].

3.1.1. Process

The welding process is divided in four main steps: rotating, plunge and dwell, translation and exit. The tool starts to rotate before the plunge phase (Figure 3.2a). During the plunge phase, the tool

penetrates into the material and, subsequently, it is held in position for a few seconds while still rotate (Figure 3.2b). This phase is called dwell time and the aim of this step is to heat and, thus soften the material before welding. Then the tool moves along the joint line carrying out the weld (Figure 3.2c). Finally, the tool is pulled out from the material (Figure 3.2d).

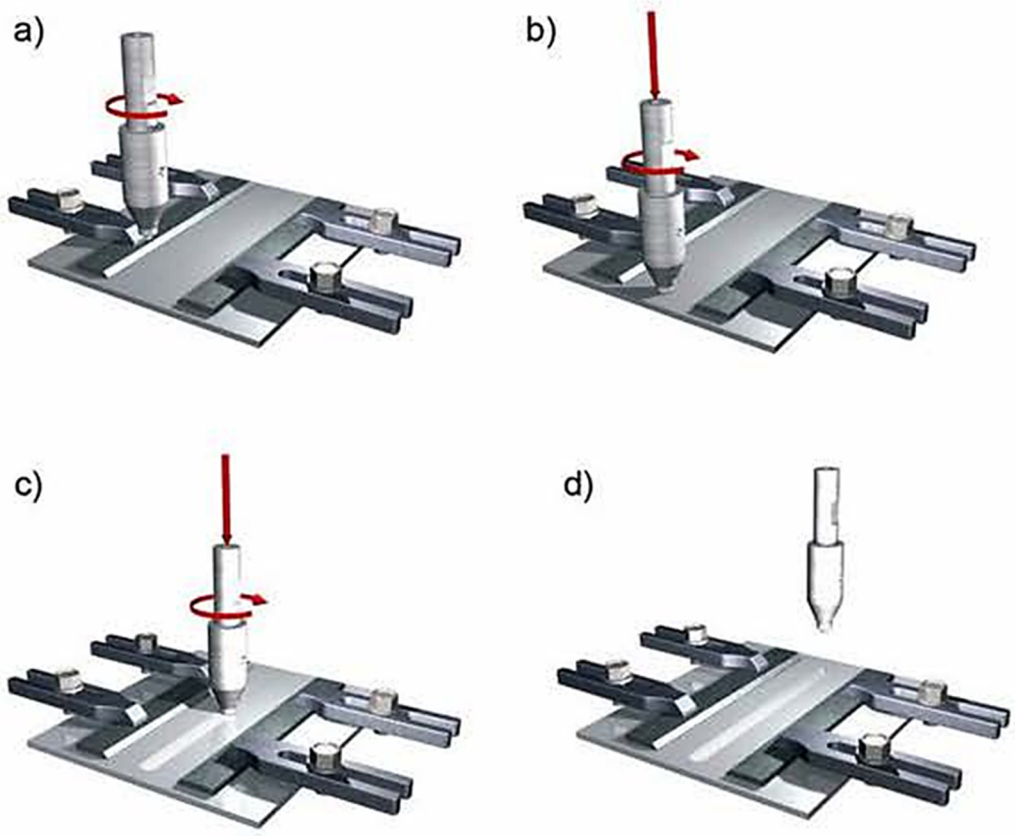

Figure 3.2 Scheme of FSW process steps: a) Rotating tool before plunging, b) Plunging and then tool shoulder touches the work piece surface producing frictional heat, c) Rotating tool traverses along the work piece, d) Pulling out from the workpiece

The tool (Figure 3.1) has two main functions: heat the workpiece and move the material to produce the joint. The heat is produced mainly by the shoulder friction with the top surface of the workpiece. This softens the material to be welded. Moreover, the shoulder prevents expulsion of the material and guides the flow of the material during welding. The tool pin, in addition to being the secondary source of heat generation, provides the stirring action to the materials of the two plates to be joined [23].

FSW is mainly a mechanical process and the forces involved in this type of work are relevant. Thus, the workpiece is placed on a thick backing plate and is clamped rigidly by strong fixture to eliminate any degrees of freedom.

3.1.2. Materials

The First industrial applications of the FSW were on aluminium alloys and light alloy in general that are difficult the weld by traditional techniques [23]. Nowadays, this technology has been employed with magnesium, copper and copper alloys, nickel, thermoplastics, titanium, steel and dissimilar materials [28-34].

- *Aluminium*

The FSW first applications were originally to weld aluminium grades that are considered difficult to weld by arc welding techniques or considered unweldable, e.g. 2XXX and 7XXX series. The main problem is the volatility of many of the alloying elements used to strengthen the aluminium that can be oxidised or burned off during fusion welding. After the solidification of the welded zone, the material in this area is no longer the same grade of starting material. Moreover, the aluminium and its alloys show important volume changes during the melting and re-solidification processes. This can cause important issues such as distortion of the components and solidification cracking due to the stresses involved. Friction stir welding, being a solid-state, mechanical process, does not show these problems and can produce good and low-distortion welds in all aluminium alloys [23].

- *Magnesium*

Magnesium is quite difficult to weld using fusion techniques. The FSW can produce excellent, low-cost and high-integrity welds with magnesium alloys [23, 28].

- *Copper and copper alloys*

The high thermal and electrical conductivity of copper have long made it a difficult material to weld, particularly in thick sections. As FSW does not melt the workpiece and applies mechanically generated heating very locally, it was seen as a potentially useful process for welding copper. Nowadays, the FSW can weld relatively easily a 50mm-thick copper welding to made canisters for nuclear waste. Other applications in copper alloys include the welding of copper cooling plates and the fabrication of brass components, such as propellers and impellers, for marine applications. Moreover, many nickel aluminium bronze propellers for naval applications have been friction stir processed in order to reduce the incidence of fatigue cracking at the blade root and, due to the improvements in surface properties, to decrease cavitation and noise [23, 29].

- *Thermoplastics*

FSW of thermoplastics is more complex than the FSW of metals because these have long chain molecules rather than individual atoms. Consequently, the flow characteristics have very different behaviour compared to metals. Process parameters and tool designs for the FSW of polymeric materials are therefore quite different from those required for metals [31].

- *Titanium*

Many of the common titanium alloys are generally weldable by conventional technique, but usually there are problems with workpiece distortion and poor weld quality. Moreover, some of the most advanced titanium alloys, e.g. Ti-6246 and Ti-17, can be difficult or even impossible to weld by fusion techniques. The FSW offers the possibility of a cost-effective method of producing high-quality and low-distortion welds in titanium plate. The welding feasibility of this material by means FSW has been proven by successfully joining CP Ti, Ti-6Al-4V, and Ti-15V-3Al-3Cr-3Sn. However, the FSW of titanium alloys is still in development and there are some limitations and issues that have to be taken into account and solved in the future [23, 32].

- *Steel and ferrous alloys*

Nowadays, FSW of steels has reached a level of technical maturity. Indeed, welds length up to 30 metres can be attained in a wide range of engineering steels. These welds demonstrate excellent mechanical properties and their corrosion and fatigue properties will exceed those of traditional fusion welds. Though steel and ferrous alloys can be welded with traditional fusion techniques, FSW shows some benefits such as: reduced distortion, lower defect rates, enhanced weld properties (mechanical and corrosion) and reduced energy consumption. Moreover, there are less health risk for the operator because there is no exposure to weld fume, hexavalent chromium, ultraviolet light, radiofrequency radiation or molten metal. Finally, the ability to weld steels that are difficult or impossible to weld by other techniques is a plus that cannot be neglected [23, 33].

- *Dissimilar materials*

Traditionally, joining dissimilar materials is a big issue with common fusion welding techniques because of the intermetallic elements formation. As FSW is a solid-state process that mechanically mixes metals together to form a bond between them, it can be used to join dissimilar metals in a straight way. This is most easily achieved when the metals to be joined have similar thermal properties and plasticisation temperatures. As an example, copper, silver and gold can be successfully joined [23, 34].

3.1.3. Advantages, issues and applications

The FSW shows many advantages linked to the solid-state welding process itself. The key benefits of FSW can be divided in metallurgical, environmental and energy benefit. The following points summarized these advantages [23]:

1. *Metallurgical benefit*
    - Solid phase process
    - Low distortion of workpiece
    - Good dimensional stability and repeatability
    - No loss of alloying elements

- Excellent metallurgical properties in the joint area
- Fine microstructure
- Absence of cracking
- Replace multiple parts joined by fasteners

2. *Environmental benefit*
   - No shielding gas required
   - No surface cleaning required
   - Eliminate grinding wastes
   - Eliminate solvents required for degreasing
   - Consumable materials saving, such as rugs, wire or any other gases
3. *Energy benefit*
   - Improved materials use (e.g., joining different thickness) allows reduction in weight
   - Only 2.5% of the energy needed for a laser weld
   - Decreased fuel consumption in light weight aircraft, automotive and ship applications

One of the main issue of FSW is that the amount of heat conducted into the workpiece determines the quality of the weld. The heat flux should be high enough to keep the maximum temperature in the work piece to 80-90% of the melting temperature of the workpiece material to avoid any welding defects [35]. This is not a problem welding low melting point materials, such as aluminium and copper, but it is a great issue welding titanium or steel. Moreover, the heat conducted back into the tool determines the life of the tool and, consequently, the life of the tools welding high melting point materials is very short.

Many industrial sectors have been understood the FSW advantages and have been adopted for commercial purposes. Here has been reported some of the industrial sectors and their relative applications [36]:

- *Shipbuilding and marine industries*: some of the applications included panels for decks, helicopter landing platforms and aluminium extrusions. Other applications in shipbuilding, are the fabrication of brass components, such as propellers and impellers;
- *Automotive industry*: in automotive sector, FSW has been employed to replace fusion welding techniques. Using this technique, has been manufactured tail light panels, automotive suspension arms etc.;
- *Aerospace industry*: longitudinal butt welds in Al alloy fuel tanks for space vehicles have been FSW and successfully employed;
- *Railway Industry*: commercial applications include building container bodies, railway tankers, etc.

3.1.4. Welding parameters

Two are the main parameters in FSW: tool rotation rate [rpm] in clockwise or counter clockwise direction and tool traverse speed [mm/min]. The rotation of tool controls the stirring and mixing action of the material and the tool translation moves the stirred material from the front to the back of the pin. Higher tool rotation rates generate an increase of temperature due of higher friction heating and result in more intense stirring and mixing of material, but the frictional coupling of tool surface with workpiece controls and governs the heating. Consequently, there is not a monotonic increase in heating with increasing tool rotation rate because the coefficient of friction at interface will change with the tool rotation rate.

Another process parameter is the tool tilt with respect to the workpiece surface. The tilt of tool towards trailing direction ensures that the shoulder holds the stirred material and move material from the front to the back of the pin in the better way. Further, the insertion depth of pin into the workpieces (in position control mode) or the downward force on the tool (in force control mode) are important for producing good welds. When these parameters are not correct, the shoulder of tool may not contact the workpiece surface or create excessive flash around the welds.

In addition, preheating or cooling can also be important for some FSW processes. For example, in materials with high melting point such as steel or titanium, the heat produced by friction and stirring may be not sufficient to soften and plasticize the material around tool. In these cases, preheating or an additional external heating source (see section 3.3), e.g. laser or inductive techniques, can help the material flow and widen the process window. On the other hand, in materials with lower melting point such as aluminium or magnesium, cooling the welding phase can be used to reduce extensive growth of recrystallized grains and obtain better welds [23].

3.1.5. Joints design

The easiest joint configurations for FSW are butt and lap joints (Figure 3.3a and Figure 3.3d). However, many other configurations can be produced by combination of butt and lap joints. For example edge butt (Figure 3.3b), T butt joint (Figure 3.3c), multiple lap joint (Figure 3.3e), T lap joint (Figure 3.3f) and, finally, fillet joint (Figure 3.3g).

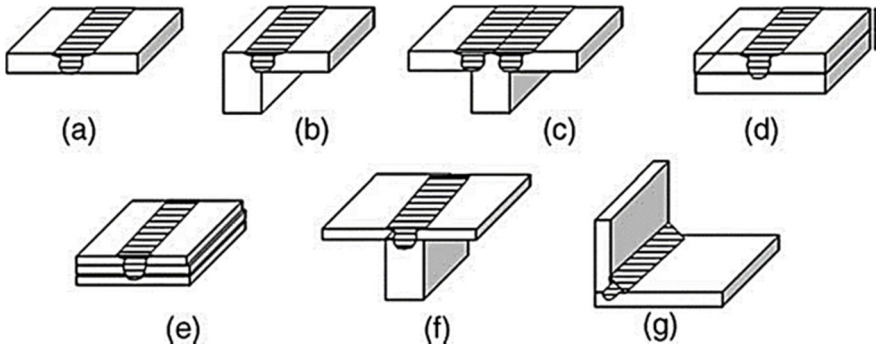

Figure 3.3 Joint configurations for friction stir welding: (a) square butt, (b) edge butt, (c) T butt joint, (d) lap joint, (e) multiple lap joint, (f) T lap joint, and (g) fillet joint [23]

One of the most important advantage of FSW is that no preparation is needed for FSW of butt and lap joints. Two clean metal plates can be easily joined together without any issue related the surface conditions of the plates [23].

3.1.6. Microstructural evolution

Based on microstructural characterization, three distinct zones have been identified in the FSW (Figure 3.4): nugget zone, thermo-mechanically affected zone (TMAZ), and heat-affected zone (HAZ).

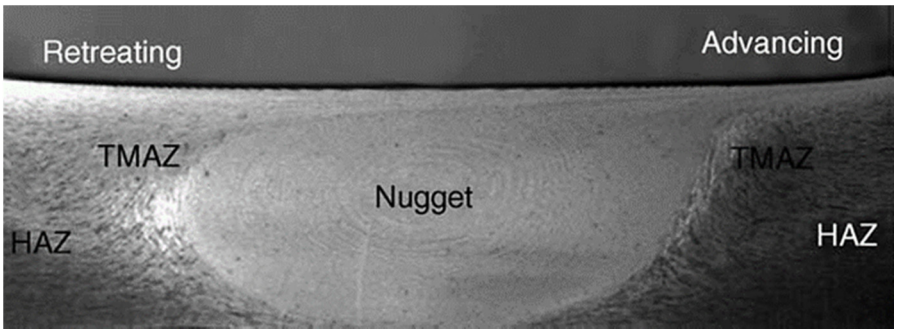

Figure 3.4 Typical macrograph showing various microstructural zones [23]

- *Nugget zone*

The intense plastic deformation and frictional heating during FSW result in generation of a recrystallized fine-grained microstructure within stirred zone. This region is usually referred to as nugget zone or dynamically recrystallized zone (DXZ). The interface between the nugget zone and the parent metal is relatively diffuse on the retreating side and quite sharp on the advancing side. Under some FSW conditions, onion ring structure was observed in the nugget zone [23].

- *Thermo-mechanically affected zone*

In the FSW process there is a unique phenomenon that is the creation of a transition zone between the parent material and the nugget zone, known as thermo-mechanically affected zone (TMAZ). As the TMAZ experiences both temperature and deformation during FSW, it is characterized by a highly-deformed structure with elongated grains in an upward flowing pattern around the nugget zone. Although the TMAZ underwent plastic deformation, recrystallization did not occur in this zone due to insufficient deformation strain [23].

- *Heat-affected zone*

After the TMAZ there is the heat-affected zone (HAZ). This zone, as in other welding processes, experiences a thermal cycle and does not undergo any plastic deformation. The HAZ retains the same grain structure as the parent material, however, the thermal exposure to high temperature exerts a significant effect on the precipitate structure [23].

3.2. Principles of heat transfer and material flow in FSW

Due to the FSW process, the stirred zone is subjected to an intense plastic deformation and a severe temperature increase. Consequently, a microstructural evolution that includes grain size and grain boundary is activated. As the mechanical properties of the welds are strictly related to the microstructure of the material, a deep understanding of mechanical and thermal processes during FSW is needed for optimizing process parameters.

3.2.1. Heat transfer and temperature distribution

Many factors can influence the thermal profiles and heat flux in FSW process. The main point is that the tool shoulder dominates the heat generation during the FSW process and, as this technique is a solid-state welding process, the maximum temperature within the weld zone is below the melting point of the material. Moreover, the maximum temperature decreases with increasing traverse speed at a constant tool rotation rate and increases with increasing tool rotation rate at a constant tool traverse speed. Finally, the maximum temperature occurs at the top surface of weld zone and, also, a slightly higher temperature on the advancing side of the joint has been noted. This is probably due to the tangential velocity vector direction that sums with the forward velocity vector of the tool [23]

Various theoretical models have been proposed so far to understand the heat generation and transfer [23, 37]. In general, these models include frictional heating and adiabatic heating. For the first contribution, the frictional heating, it should depend on the surface velocity and coefficient of friction. Thus, the temperature generation should increase from centre of the tool shoulder to the edge of the tool shoulder. Moreover, also the pin should provide some frictional heating. The second contribution, the adiabatic heating, should be maximum at the pin and tool shoulder surface and should decrease away from the interface.

Actually, the theoretical models do not often integrate all these contributions because they are really complex issues. For example, Sharma and Mishra [23] have observed that the frictional condition change from ‘stick’ at lower tool rotation rates to ‘stick/slip’ at higher tool rotation rates. Set the speed of the tool that determine this change from ‘stick’ to ‘stick/slip’ is quite difficult. Moreover, more complex is to determine the area of the tool that is in a condition of ‘stick’ and the areas that are in the condition of ‘slip’ [23].

Schmidt et al. [37, 38] have developed an analytical model that take into account the choice of sticking and sliding contact conditions. The expressions for the heat generation in the different condition, i.e. sticking, sliding, and partial sliding/sticking conditions, are:

$$Q_{total,sticking} = \frac{2}{3}\pi\frac{\sigma_{yield}}{\sqrt{3}}\left(\left(R_{shoulder}^3 - R_{probe}^3\right)(1+\tan\alpha) + R_{probe}^3 + 3R_{probe}^2 H_{probe}\right) \quad (3.1)$$

$$Q_{total,sliding} = \frac{2}{3}\pi\mu p\omega\left(\left(R_{shoulder}^3 - R_{probe}^3\right)(1+\tan\alpha) + R_{probe}^3 + 3R_{probe}^2 H_{probe}\right) \quad (3.2)$$

$$Q_{total} = \frac{2}{3}\pi\left(\delta\frac{\sigma_{yield}}{\sqrt{3}} + (1-\delta)\mu p\right)\omega\left(\left(R_{shoulder}^3 - R_{probe}^3\right)(1+\tan\alpha) + R_{probe}^3 + 3R_{probe}^2 H_{probe}\right) \quad (3.3)$$

where Q is the heat generation [W], σ_{yield} the yield strength [Pa], ω the tool angular rotation speed [rad/s], $R_{shoulder}$ the tool shoulder radius [m], R_{probe} the tool probe radius [m], α the tool shoulder cone angle [rad], H_{probe} the tool probe height [m], p the contact pressure [Pa] and δ is the contact state variable [37].

In the next chapter, this model will be employed to calculate the rate of heat generation during FSW simulation in a Finite Element model that will be described in a deeper way later.

3.2.2. Material flow

The material flow during FSW is quite complex and, nowadays, the understanding of deformation process is limited. Indeed, many factors can influence the material flow during FSW welding process, e.g. tool geometry, welding parameters, material types, and workpiece temperature. The metal flow in friction stir welding can be modeled as a metalworking process [23] in terms of five conventional metal working zones: preheat, initial deformation, extrusion, forging, and cool down (Figure 3.5a and b).

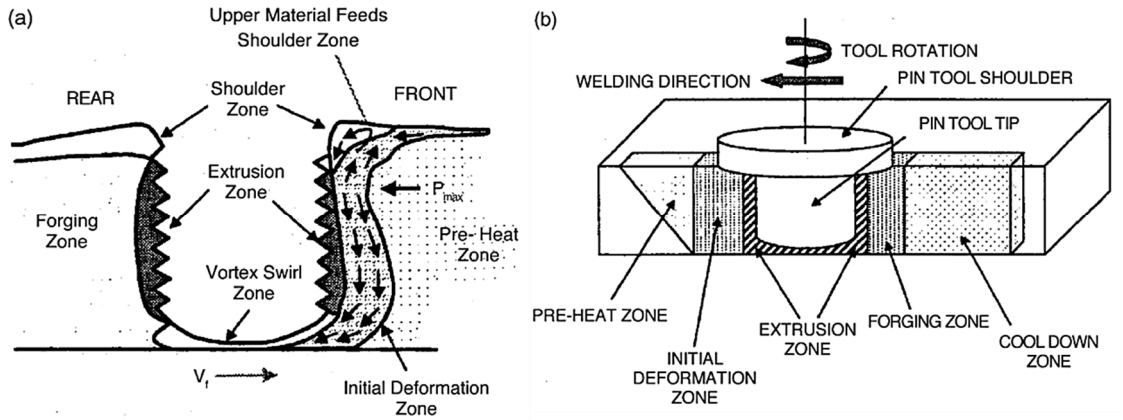

Figure 3.5 FSW metal flow modelling as a metalworking process [23]

In the preheat zone, the temperature rises due to the frictional heating of tool and adiabatic heating caused by the deformation of the material. In this zone the heating is governed by the thermal properties of the material and the traverse speed of the tool. As the tool moves forward, the material in this zone is forced to flow upwards into the shoulder zone and downwards into the extrusion zone. However, some material is captured in the swirl zone under the pin tip where a vortex flow is created by the rotating tool. In the extrusion zone with a finite width the material flows around the pin from the front to the rear. The dimension of this zone is related to the temperature that allows the material to flow. After the extrusion zone, there is the forging zone, where, the material from the front of the tool is forced into the cavity left by the forward movement of the pin. The shoulder of the tool helps to constrain material in this cavity and also

applies a downward forging force. Moreover, the material on the surface of the weld is dragged from the retreating side toward the advancing side. Behind the forging zone there is the cooling zone where the material cools under passive cooling conditions [23].

3.3. Improvements of FSW

One of the most important issue in FSW is the difficulty to weld hard material, e.g. titanium and steel. This because, the FSW of hard and high melting point materials, requires high thermal and mechanical loads on the tool. An immediate conclusion could be that the use of an external source to pre-heat and soften the hard materials during the FSW should reduce the load requirement on the tool. This should lead to improve the tool performance and life, extend the FSW process window and increase the welding efficiency and quality. With this clear objectives, several variants of FSW have been developed over the past few years. The new variants focused on assisting the FSW process by heating the workpieces by means of an auxiliary energy source. In this section, a brief summary of the improvements of the base technique has been reported. No standard terminology is employed to refer the new variants of FSW. Terms such as ‘assisted’, ‘enhanced’ or ‘modified’ are used to define this new variants [39].

The objective of the water cooled FSW is totally different compared to the ‘assisted’ techniques. This improvement has the scope to improve the mechanical characteristics of the joints on materials that are ‘traditional’ for FSW [40, 41], e.g. aluminium.

3.3.1. Electrically assisted FSW

In Electrically assisted FSW (EAFSW), an electric current is supplied to the workpieces in order to heat the material during the welding by producing the Joule heating effect and the electroplastic effect [39]. The Joule effect generates additional heat that pre-heats the workpieces and the electroplastic effect (EPE) causes additional material softening without a substantial preheating. The EPE describes the material softening phenomenon induced by current during plastic deformation of metals. Previous studies [42-44] have reported that the movement of electrons due to applied current can dynamically change the material behaviour in plastic straining range without a substantial temperature increase. These additional effects increase the heat generated during the FSW process and help the tool to advance in easier way and to carry out a better weld. Generally, there are two ways to exert the electrical current on the workpieces: one is employing the FSW tool and second is applying directly on the workpiece. Thus, the experimental setup for the first case (Figure 3.6a) consists of a FSW machine and an arrangement for resistance heating, where, the tool forms an integral part of the electric circuit and the current passes into the workpieces via the tool [39, 45]. In the second case (Figure 3.6b), the current is supplied into the workpieces without the direct involvement of the tool in the circuit but, however, this may be passively involved in the circuit during the welding [39, 46].

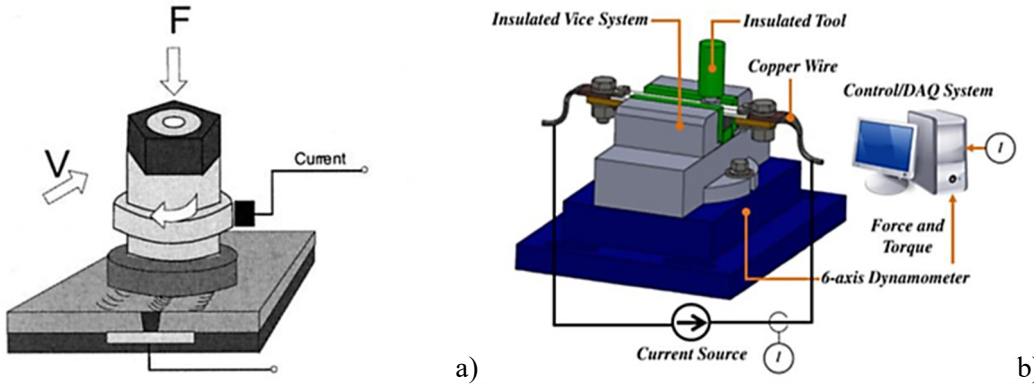

Figure 3.6 Schemes of EAFSW with tool integrated in the electric circuit (a) [45] and without (b) [46]

As the mechanical power and the applied electrical power in EAFSW are not related, this allows a wider possibility to select the correct parameters to carry out a better weld and preserve the tool from the wear. The EAFSW shows many advantages compared to the traditional FSW. In the plunge phase, there is a reduction of the plunge force because the EAFSW has higher temperatures at the surface and at the bottom of the workpiece. This should improve the wear resistance of the tool and, thus, increase the tool life and also the performance. Moreover, the welding speed and the downward force can be, respectively, higher and lower than the FSW values. This is because, in EAFSW, the needed temperature profile to obtain a good weld, can be achieved also at higher speed and lower downforce due to the thermal support of electric current [47].

However, though the EAFSW is yet in the development stage and few study deals with this subject, the advantage of this technique compared to FSW in increase welding speed, reduce downward force and tool wear are clear [39].

Finally, the most important drawback of the EAFSW process is that it is applicable only to conducting materials.

3.3.2. Induction assisted FSW

The Induction Assisted FSW (IAFSW) is a non-contact method of pre-heating the welding zone ahead the FSW tool. The induction heating occurs when an electrically conductive material is placed in a varying electromagnetic field. This field induces an electric current inside the material and, due to the Joule effect, the heating of the material. In the IAFSW, the induction coil travels linearly along the weld line and it is positioned at a distance 20 mm ahead of the welding tool. In Figure 3.7, an example of setup for IAFSW has been reported.

The IAFSW process has been employed to weld aluminium alloys, such as Al6082, and high strength ferrous alloys. In the IAFSW of Al 6082, the forces on the tool can be reduced up to 50% and the welding speed can be doubled carrying out good welds. Also in high strength ferrous alloys, the IAFSW carried out the process with a reduction in the plunge force and the welding force of, respectively 30% and 35% [39].

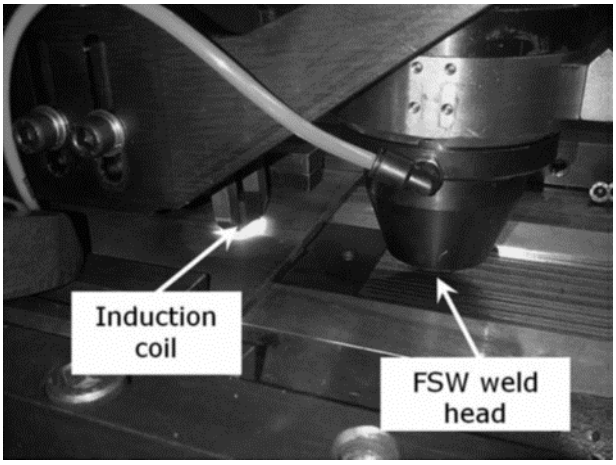

Figure 3.7 Example of setup for IAFSW [39]

Moreover, the IAFSW should reduce the distortion due to the residual stress and improve the plastic deformation. This should eliminate the heavy clamping systems and reduce the size of the FSW machine because the materials can be easily deformed. The drawbacks of this technique are the difficulty and problems related to the control of the current flow, the spark generation and the heating of all the conductive materials involved in the current path. Finally, the IAFSW process is applicable only to conducting materials [39].

3.3.3. Laser assisted FSW

Laser assisted FSW (LAFSW) is the most widely used and studied variant of FSW [39]. In this technique, a defocused laser beam precedes the FSW tool during welding at a distance between 10 to 40 mm, increasing the temperatures reached in front of the tool and allowing an easier advancement of the same. In Figure 3.8 a scheme of the LAFSW setup has been reported. The commonly used laser sources are diode laser, Nd:YAG fibre optic laser and CO2 laser. The laser spot is activated just before the plunging stage or at the start of the welding phase of FSW [39].

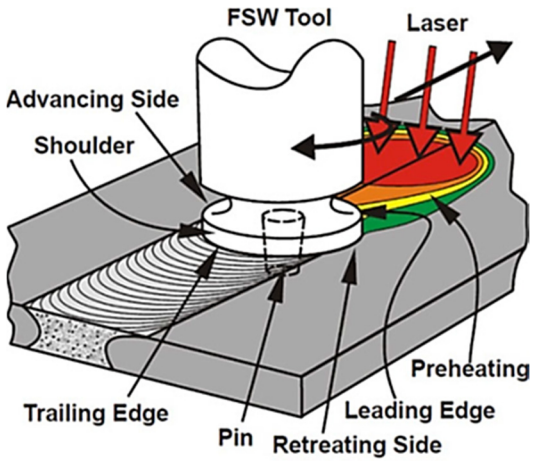

Figure 3.8 Scheme of the LAFSW setup [39]

The assistance of the laser in FSW is an attractive way to preheat the material with a conventional FSW setup. This technique has been employed to weld a variety of light alloys, high strength

alloys and dissimilar alloys. The higher heat input allows a better material plasticisation and grain refinements that improve the material flow and the mechanical properties. The better plasticisation should help also to reduce the downward axial force, the tool wear and increase welding speed. Finally, due to the lower process forces also the deflections in the machine and on the fixture are decreased and this allows a reduction of the machine dimension [39].

3.3.4. In-process cooled FSW

The in-process cooling of the FSW joint during the weld phase has the objective to reduce extensive growth of recrystallized grains and dissolution of strengthening precipitates in the stirred zone for the materials, such as aluminium or magnesium, that have low melting point. Several techniques have been developed to in-process cooling FSW [48, 49]. The main difference among these is the mean employed to cool down the welded zone, e.g. air or water flow (Figure 3.9).

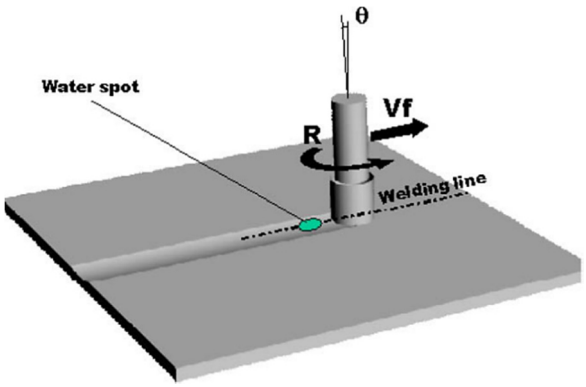

Figure 3.9 Scheme of water in-process cooling of FSW [41]

In general, an improvement is observed in the mechanical resistance (UTS) of the joint that are in-process cooled by an external cooling during the FSW process. This improvement can be explained because a significant decrease of the extension of the altered zones, the HAZ and TMAZ is observed at the increasing of the effectiveness of the cooling medium employed [48]. Moreover, as the HAZ is the weakest location of the weld since it experiences the greatest coarsening and transformation of metastable precipitates, cooling during FSW results in a fall in temperature that leads to grain size reduction and the hardness improvement [41].

3.4. Residual Stresses

Due to the complex thermal and mechanical process of fusion welding, residual stresses can develop in the weld and surrounding region. These are due to the localized application of heat in combination with the applied constraints. In FSW the residual stresses, as it is a solid-state welding process, are generally considered low in value. However, due to the higher force involved in the weld and, thus, the rigid clamping used in FSW, the residual stresses are not low in general. The constraints avoid the contraction of the weld nugget and heat-affected zone during cooling in

both longitudinal and transverse directions, thereby resulting in generation of longitudinal (parallel to welding direction) and transverse stresses (normal to welding direction). As the presence of high residual stress values influence the post-weld mechanical properties, e.g. fatigue properties, it is very important to investigate the residual stress distribution in the FSW welds.

Some studies have been carried out on residual stresses in FSW [23, 50-53]. In most of these, some similar conclusions can be highlighted. First, the residual stresses in FSW welds are lower compared to those generated during fusion welding but they are not negligible at all. The low residual stress in the FSW welds has been attributed to the lower heat input during FSW and recrystallization accommodation of these stresses [23]. Second, the longitudinal residual stresses are higher than the transverse ones, independent on pin diameter, tool rotation rate and traverse speed. Third, both longitudinal and transverse residual stresses exhibited an ‘‘M’’-like distribution across the weld (Figure 3.10). Moreover, a higher residual stress peak is detected in the advancing side.

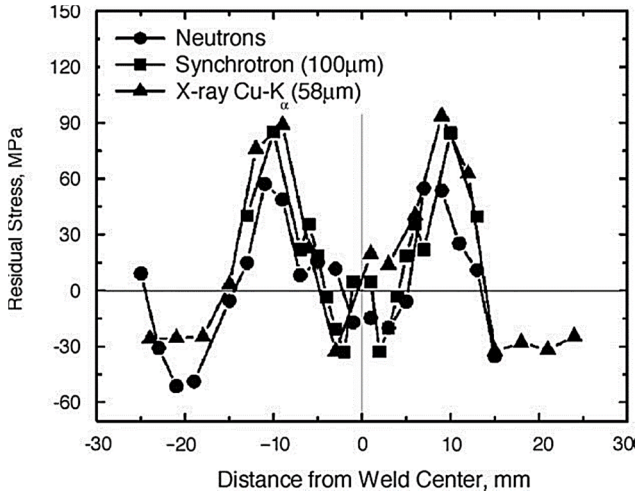

Figure 3.10 Longitudinal residual stress distribution in FSW 6013Al-T4 welds determined by different measurement methods [23]

The Figure 3.10 shows that maximum tensile residual stresses are located at the edge of the tool, i.e., in the HAZ. Moreover, compressive residual stresses are measured in the parent metal adjacent to the HAZ. Fourth, the residual stresses distribution across the welds is similar on the top and root sides of the weld. Fifth, because the maximum residual stress is located at the edge of the tool, large-diameter tool widened the M-shaped residual stress distribution. With decreasing welding speed and tool rotation rate, the magnitude of the tensile residual stresses decreased.

Finally, the maximum value of residual stresses observed in various FSW of aluminium alloys are below 100 MPa [23]. As this residual stress magnitude is significantly lower than yield stress of aluminium alloys, there is a significant reduction in the distortion of FSW components and an improvement in mechanical properties.

4. Temperature field in FSW and laser assisted FSW processes

The temperature distributions and the thermal histories have an important role in FSW and LAFSW. They determine whether the welding process will produce a good weld influencing the residual stresses, the microstructure, and the strength of welds. Several studies have measured temperatures in FSW using thermocouples [54-56] but only a few have been involved in experimental analysis using thermography [57] and still less on laser assisted friction stir welding. Xu et al. [54], using thermocouples, found that the temperature distribution during the tool inserting is only related to the rotational speed and that the temperature increases with increasing the rotational speed or decreasing the transverse speed during the stable phase of welding. They also found that the tensile strength and yield strength of joints increase with increasing the rotational speed, while the percentage of elongation decreases. Hwang et al. [55] conducted a study on temperature distribution using thermocouples and find out that the temperatures on the advancing side are slightly higher than those on the retreating side. Also Maeda et al. [56] have applied thermocouples on both top and bottom surface of the work plates and have found an asymmetric temperature distribution between the advancing side and the retreating side.

Although experimental measures are fundamental to understand the thermal phenomenon in the FSW process and LAFSW, they present some limitations, (e.g. economic costs or internal temperature measurements). For this reason, the implementation of numerical models that can predict the temperature distributions have an important role to estimate the correct weld parameters in order to improve mechanical properties of the welded joints and reducing the amount of trials and errors.

4.1. Thermographic analysis of FSW and laser assisted FSW

In this section, the experimental setup employed to measure the temperature field on both FSW and LAFSW will be shown. Moreover, the influence on the temperature of the distance laser spot - FSW tool and of the laser source power will be investigated.

4.1.1. Thermographic experimental setup

A NEC H2640 infrared camera with configurable ranges between -40 °C to 2000 °C, a resolution of 0.06°C, an accuracy of ±2°C and a spectral range of 8–13 μm has been used to acquire the temperature during the welding process. The experimental setup of the thermal camera has been reported in Figure 4.1.

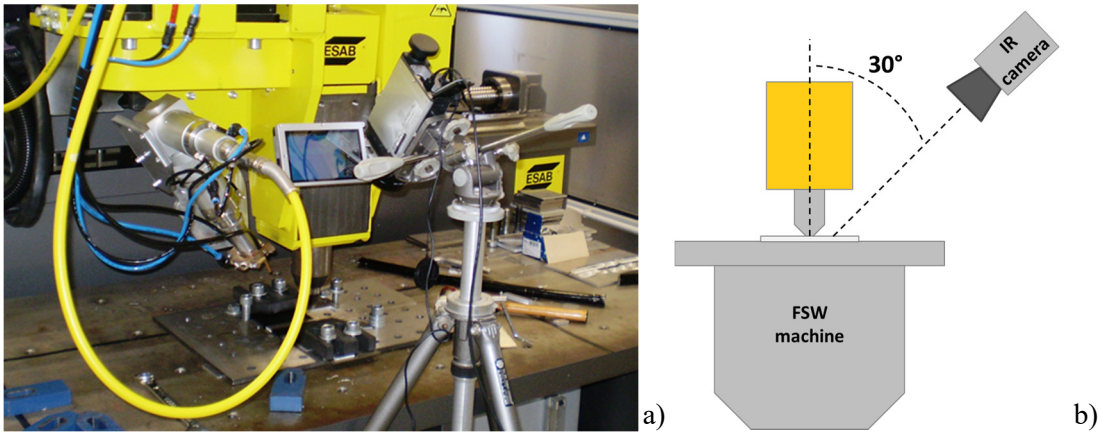

a) b)

Figure 4.1 Experimental setup (a) and setup scheme (b)

The angle between the camera and FSW tool axis has been set to 30°. Due to reflection problems and low emissivity of aluminium, the specimen has been painted with matte black acrylic spray paint. An emissivity ε = 0.95 has been set on the camera.

In general, when the specimens have to be mechanically tested after the welding process, the central zone of the specimen has not been painted to avoid paint inclusion into the welded joint. This allows to acquire correctly the temperature near the tool, but not influencing the mechanical characteristics of the joints. However, when there is the necessity to acquire the temperatures in front of the tool, e.g. in Laser assisted friction stir welding, the specimens have been completely painted and bead-on-plate welds have been done (Figure 4.2). Consequently, no mechanical tests have been done on this typology of specimens.

Temperature measurements has been carried out on the retreating side of the welded plate, because the configuration of the FSW machine prevents access to both sides.

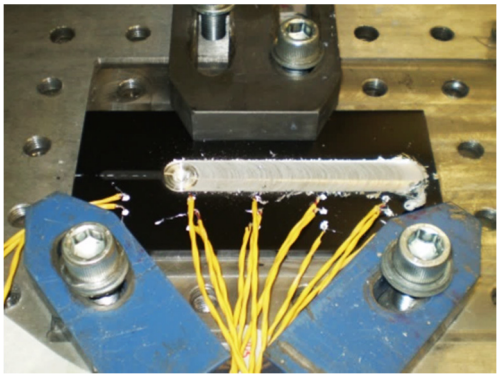

Figure 4.2 Bead-on-plate specimen example

4.1.2. Materials and methods

In order to investigate the influence of the distance laser spot-FSW tool (Figure 4.3) and of the laser source power on the temperature reached in the front zone tool, some tests on the traditional FSW and on three configurations of LAFSW bead on plate have been carried out. During the tests, the temperature fields and thermal histories have been recorded by the infrared camera.

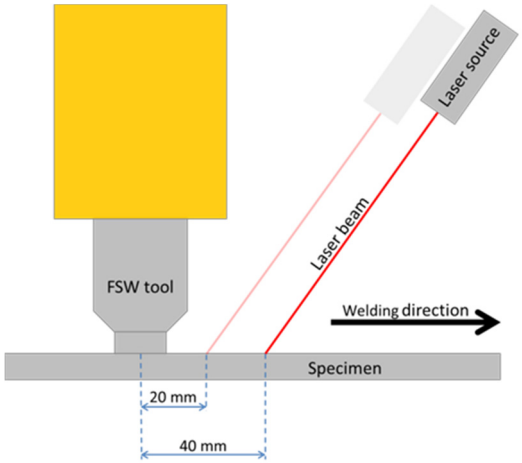

Figure 4.3 Location scheme of the laser source

The trials have been conducted on aluminium 5754 H111 sheets, 200 mm length, 100 mm width and 6 mm thick. The chemical composition, the thermo-physical properties, and mechanical characteristics at room temperature (20°C) of aluminium 5754 H111 have been reported in Table 4.1 and Table 4.2.

Table 4.1 Chemical composition Al5754

Al [%]	**Si** [%]	**Fe** [%]	**Mn** [%]	**Mg** [%]
96.1 - 95.5	0.4	0.4	0.5	2.6-3.2

Table 4.2 Physical and mechanical characteristics

Parameter	**value**
Density [kg/m^3]	2650
Melting temperature [°C]	600
Thermal conductivity [W/m·K]	138
Thermal expansion coefficient [1/K]	$23.9 \cdot 10^{-6}$
σ_y [MPa]	103.4
σ_u [MPa]	215
Vickers Hardness (HV)	55

A 4 kW Ytterbium fiber laser coupled with a 4 kW FSW machine has been employed to carry out the welds. Table 4.3 lists the process parameters set in the experimental tests for the FSW and the LAFSW. Only laser power or laser spot – FSW tool distance have been changed while tool rotation, dwell time and traverse speed have been kept constant.

Table 4.3 Process parameters

Designation	**Laser power** [W]	**Dist. laser – FSW tool** [mm]	**Traverse speed** [cm/min]	**Dwell Time** [s]	**Rotational speed** [rpm]
FSW	-	-	20	3	500
500W/40	500	40	20	3	500
1000W/40	1000	40	20	3	500
500W/20	500	20	20	3	500

The test with laser power 1000W and 20 mm distance has not been performed because the temperature reached in this case exceeded the temperatures range of the thermo-camera.

4.1.3. Results and discussion

The Figure 4.4 shows the thermographic comparison, in four different instants, between the welded specimens. The end of the dwell time is t_1, t_2 and t_3 are intermediate phases and t_4 is the instant before extracting the tool.

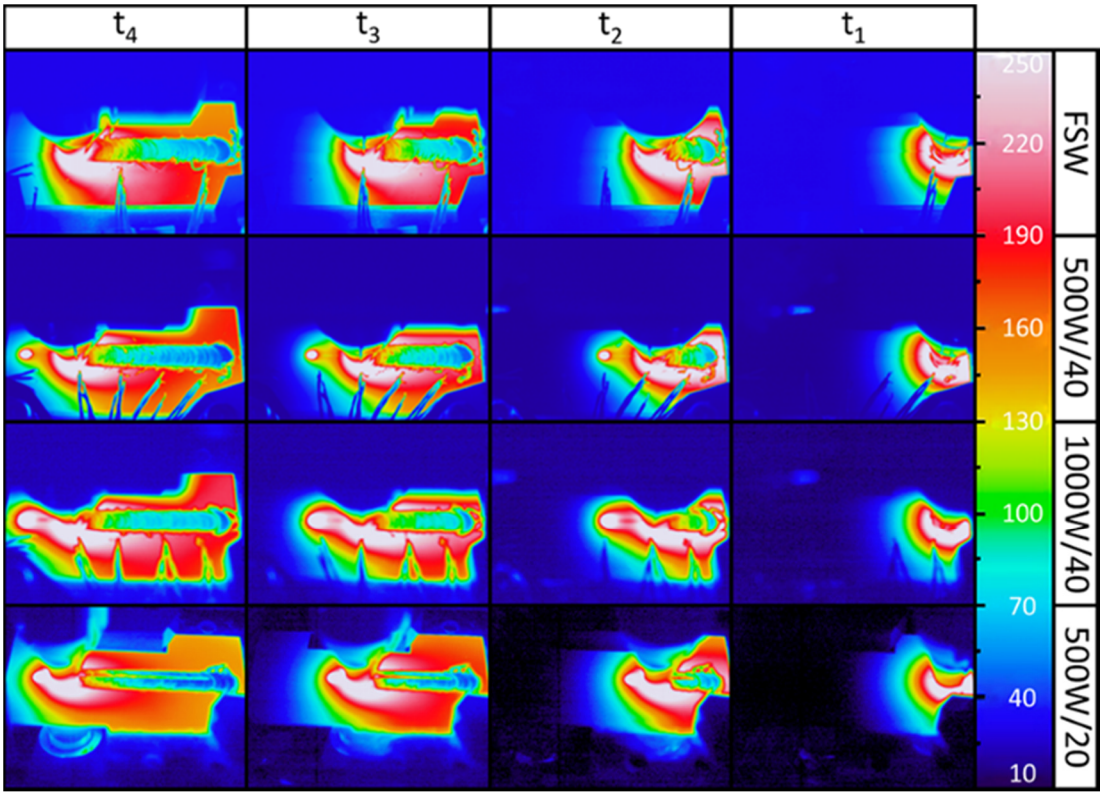

Figure 4.4 Comparison between the thermography results of the welded specimens in four different instants

The white area in the Figure 4.4 describes the zone of the specimens where the temperature exceeds 250 °C. This value has been chosen because it is slightly above the temperature (200 °C) reached by the FSW in the area of the tool (Figure 4.5). In this way, it has been visually identified the area in front of the tool which is influenced by laser. Furthermore, the temperature on the bead is due to the variation of the emissivity after the transit of FSW tool. This is due to the paint removal and change of roughness of the surface of the specimens. The figure shows that for the 500W/40 and less for 1000W/40 the temperature between laser spot and FSW tool decreases rapidly at values under 250 °C. This implies that the pre-heating effect of the laser is vanished. This is due to the high conductivity of aluminium and the excessive distance of the FSW tool from the laser spot. The graphic reported in Figure 4.5 highlights this behaviour. Along the welding line, the effect of 500 W and 1000 W laser power at a distance of 40 mm, in the zone near the tool (indicated by A), produces a slight increase of temperature than the traditional FSW.

Instead, reducing the distance of the laser spot to 20 mm produces, also with 500 W laser power, a considerable increase of temperature in the front zone of the tool.

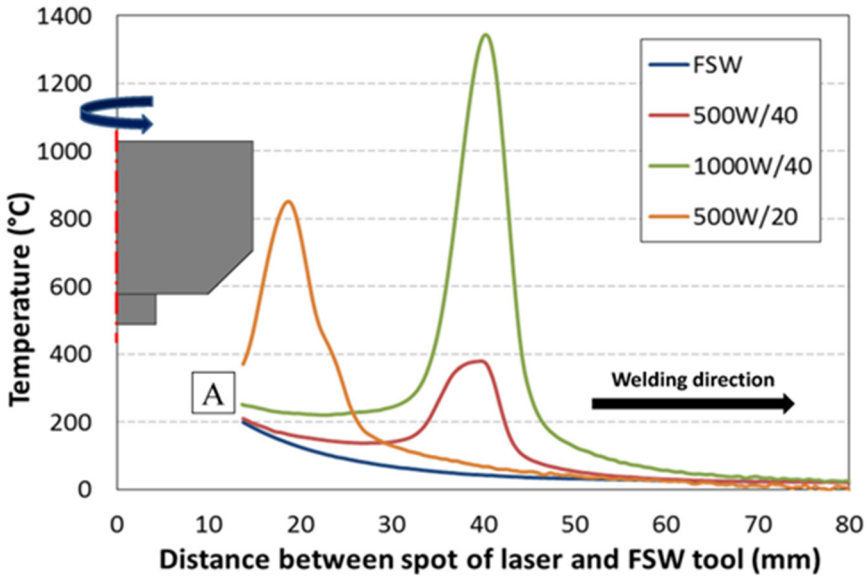

Figure 4.5 Temperature comparison along welding line in front of FSW tool

4.2. Numerical prediction of temperature fields in FSW and LFSW

In this section, it will be shown the main characteristics and working principles of the FSW and LAFSW numerical models and the validation of the numerical models based on the thermographic experimental results.

4.2.1. FSW Model description

To simulate the FSW thermal history, a three-dimensional transient thermal model has been developed using the finite elements commercial code ANSYS 14.5. Due to the symmetry of the problem, just a half plate model has been implemented, in order to decrease the elements number and reduce computational time. The model has been meshed using 6000 SOLID90 elements [58]. In order to describe more accurately the thermal behaviour near the tool area and to take into account the higher gradient of temperature, a thicker mesh has been used near the plane of symmetry (Figure 4.6). The natural convection between aluminium and air on the top surface and on the lateral side of the specimen is equal to 20 $W/m^2°C$. Furthermore, the conduction between the bottom surface of the specimen and the backing plate has been simulated with a convection coefficient of 300 $W/m^2°C$. The numerical value of this one has been selected in the way to match as well as possible the maximum temperature of the numerical model with experimental data.
Because the SOLID90 element does not accept at the same time thermal loads and convection, it has not been possible to insert the convection heat transfer on the welded area. The radiation heat loss has been neglected because temperature hardly exceeds 500°C in the FSW of aluminium alloys [59].

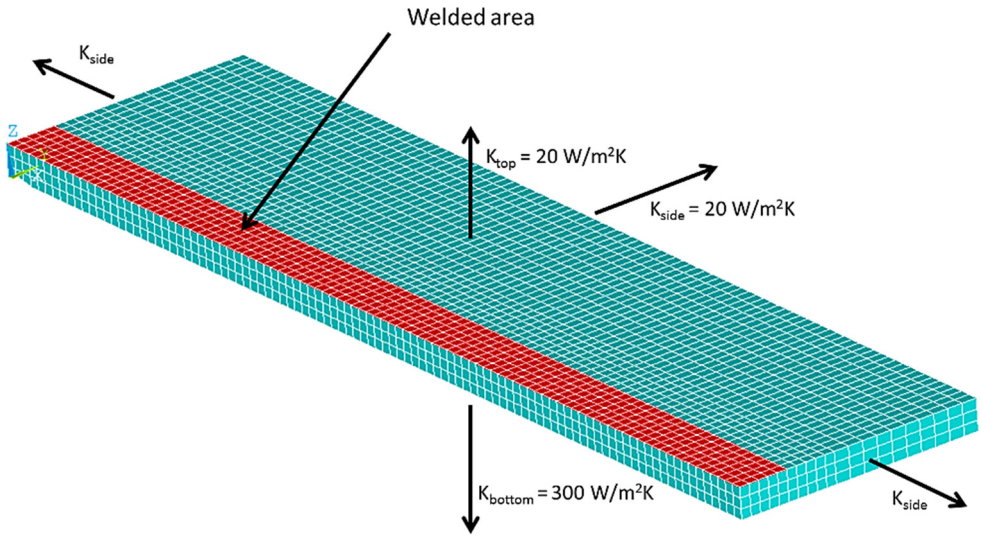

Figure 4.6 FSW model mesh and convection coefficient

The AA5754 thermo-physical material properties (i.e. thermal conductivity and specific heat) have been implemented as a function of temperature (Table 4.4). Due to a lack of literature data, the density of the material has been kept constant with the temperature.

Table 4.4 Temperature dependent material properties of AA5754 [60]

Temperature [°C]	**Density** [kg/m3]	**Specific heat** [J/kg·K]	**Thermal conductivity** [W/m·K]
20	2650	891.6	138
100		950	147.2
200		988.4	152.7
300		1015.2	162.7
400		1045.6	152.7
500		1106.6	158.75

The welding process has been simulated by a moving thermal source along the welded zone. According to Schmidt et al. [37, 38], the analytical expression used for simulate FSW tool heat generation is the previously reported equation 3.2. Here, it is reported modified replacing the pressure p by the downward force F_n and the area of the tool shoulder:

$$Q = \frac{2}{3}\mu\omega\frac{F_n}{R_{shoulder}^2}\left(\left(R_{shoulder}^3 - R_{probe}^3\right)(1+\tan\alpha) + R_{probe}^3 + 3R_{probe}^2 H_{probe}\right) \quad (4.1)$$

The equation 4.1 takes in account the specific tool geometry: $Rs_{houlder}$ and R_{probe} are the tool shoulder and probe radius while α and H_{probe} are the tool shoulder cone angle and probe height (Figure 4.7). The other parameters are related to FSW process: μ and F_n are respectively the friction coefficient and the normal plunge force while ω is the rotational speed. According with Schmidt et al. [37, 38], the friction coefficient μ was set equal to 0.3. The tool geometrical parameters are: $R_{shoulder}$ 10.75 mm, R_{probe} 3 mm, α = 0° and H_{probe} 5.8 mm.

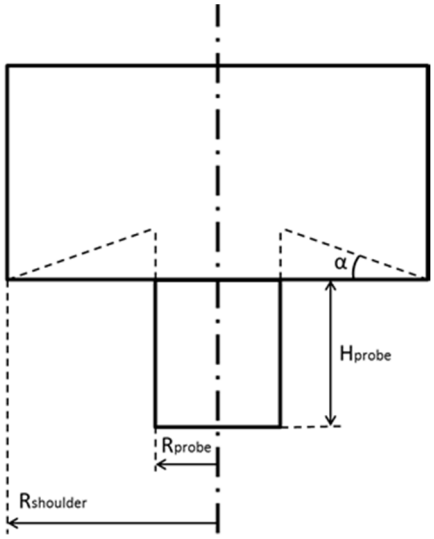

Figure 4.7 Tool scheme

The normal force F_n has been set equal to 20000 N in accordance with that measured during the experimental tests in the steady state conditions. Finally, the penetration and the tool pullout phase have been described in the numerical model as a linear increment of the FSW heat source in the time. The penetration speed has been set in 0.637 mm/s in the model on the base of experimental observation and the corresponding penetration time is 6.7 s. The numerical description of this behavior finds evidence in the experimental data.

4.2.2. Laser assisted FSW model description

The LAFSW numerical simulation is based on the previously described FSW model. However, beyond the adding of the laser source, some other improvements have been done, e.g. the adding of a backing plate in order to simulate in a better way the cooling phase.

The thermal analysis has been carried out on bead on plate configuration in order to calculate the temperatures during the weld. These simulated temperature values have been compared to those experimental measured during the bead on plate welding process in order to validate the model.

The same temperature dependent thermo-physical properties of the previous described model have been used (Table 4.4) and, also in this case, only half plate has been simulated to reduce the computational time. In Table 4.5 the LAFSW process parameters have been reported.

Table 4.5 Process parameters of LAFSW

Traverse speed [cm/min]	**Dwell Time** [s]	**Rotational speed** [rpm]	**Tilt angle** [°]	**Laser power** [W]	**Distance Laser spot-FSW tool** [mm]	**Plunge Force** [N]
20	3	500	2	500	40	20000

A gradual thicker mesh of SOLID90 elements has been adopted near the welding line to describe more accurately the thermal behaviour where the temperature gradient is higher (Figure 4.8). The natural convection between aluminium and air has been set to 20 W/m^2°C on the top surface and

on the lateral side of the specimen. In this model, in different way of the previous, the conduction between the specimen and the backing plate has been simulated (Figure 4.8). A thermal contact conductance coefficient of 450 W/m^2°C has been introduced between the bottom face of the specimen and the backing plate. This value has been chosen in the way to match the maximum temperature of the numerical model with experimental data. The backing plate is a 400 mm x 400 mm x 10 mm FE360 steel plate.

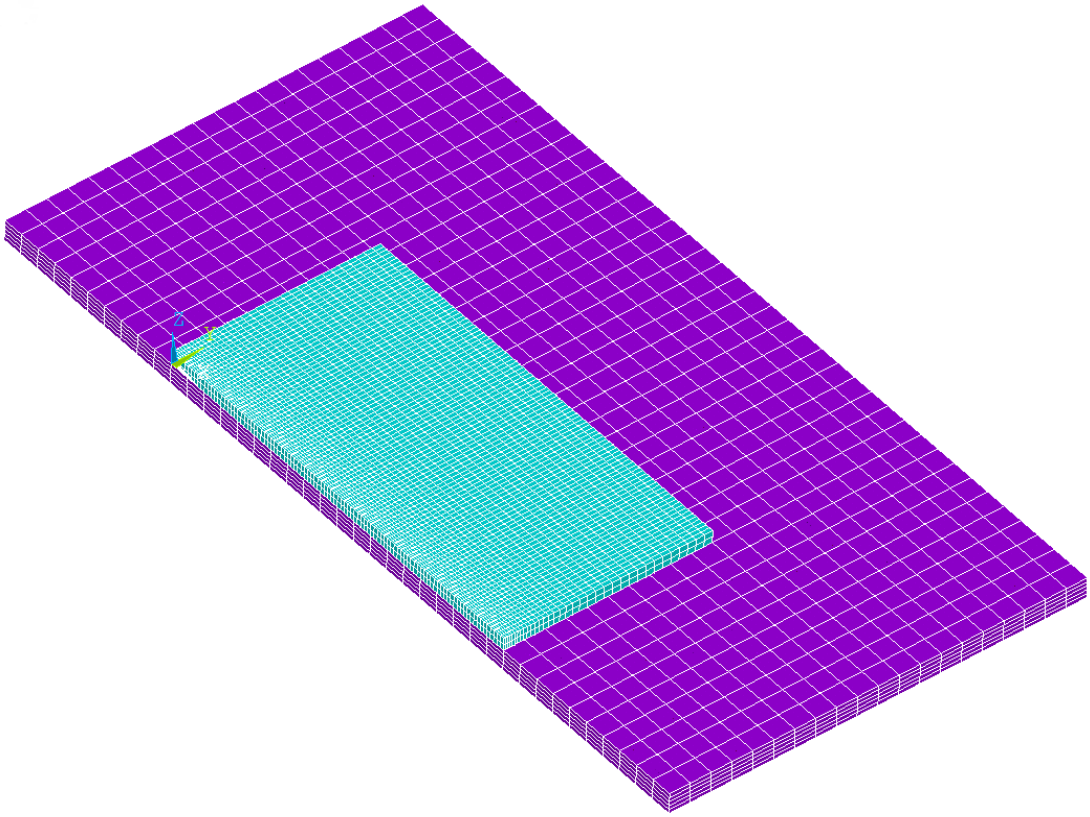

Figure 4.8 LAFSW scheme of model mesh

In Table 4.6, the thermo-mechanical properties of the FE360 steel backing plate have been reported.

Table 4.6 Backing plate thermos-mechanical properties

Parameter	**Value**
Young's Modulus [GPa]	210
Density [kg/m^3]	7750
Thermal conductivity [W/m·K]	48.9
Thermal expansion [m/m·°C]	$12.5 \cdot 10^{-6}$
Specific heat [J/kg·K]	103.4
Poisson's ratio	0.29

As in the previous FSW model, the welding process has been modelled as a uniform thermal source with a radius equal to $R_{shoulder}$ that moving along the welding line. The analytical expression

used for simulate FSW tool heat generation is the same of the previously described FSW model (equation 4.1) and the same tool has been employed to carry out the weld. However, in this model, while F_n has been set to 20000 N as the previous FSW model, the friction coefficient μ has been set equal to 0.237 according to the experimental tests. Finally, the laser source has been simulated as a uniform heat source of 2 mm radius that moves together to FSW tool.

4.2.3. Results and discussion

In this section the results and the validation of the FSW and LAFSW models will be presented.

- FSW model

The verification and validation of the previous described FSW model has been carried out on bead on plate welds. In Figure 4.9 has been reported a scheme of the points that have been analysed. Three different steps have been studied and reported in the later graphs. In each step the tool has been aligned at the measured points and the temperature has been acquired in both numerical and experimental data. The start moment corresponds to the welding initial step when the FSW tool has just started the weld and it is about 30 mm from the right edge of the plate. The middle step has been selected in order to be in the half of the specimen. Finally, the end step is located at 30 mm from the left of the plate. For each step the temperature of four different points has been acquired, the firsts three points have been spaced of 10 mm from each other, the last one has been positioned at the edge of the specimen. It has not been possible to collect experimental data nearer the center line for the presence of the FSW tool and the processing burrs that modifies the emissivity of the surface and thus the temperature.

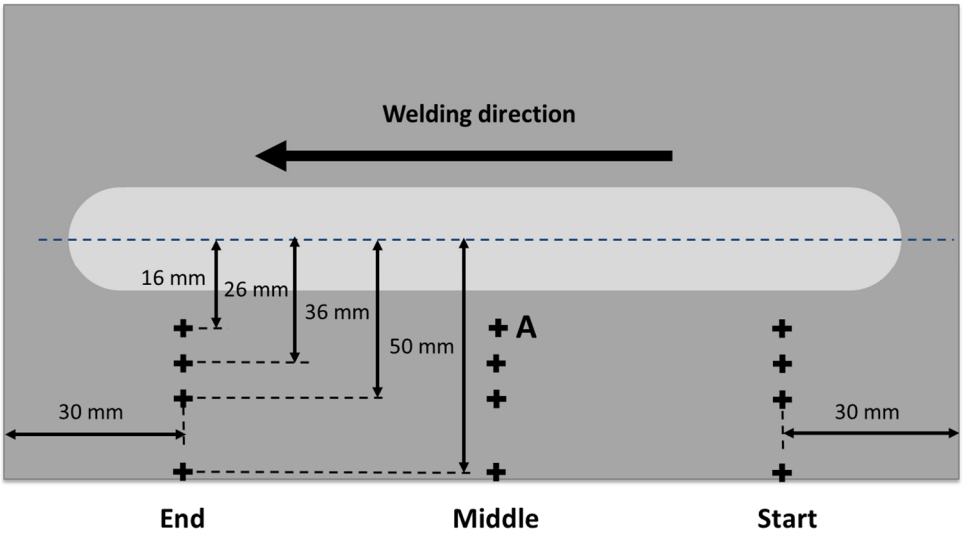

Figure 4.9 Location scheme of experimental measured points

The peak temperature reached at a specific position during welding is a very important issue that determines the material microstructure and also the mechanical properties of the joints. Therefore, the graphs of the maximum temperatures versus distance from the weld line have been plotted in

Figure 4.10, Figure 4.11 and Figure 4.12 describing the start, middle and end step. In these have been plotted both numerical and experimental data to compare and validate the model. Generrally, these show that the temperature decreases moving away from the welding line and that the numerical model fits the experimental data with low errors. In fact, in the start step (Figure 4.10) the maximum error between experimental and numerical data is 5.9%, in the middle step it is 6.2% (Figure 4.11) and in the end step, Figure 4.12, the error is 6.3%. The temperatures in the start step are generaly lower than that the other two phases (that are almost the same) and this implies that, after the start step, a steady heat transfer could be reached in the FSW process. The temperature gradient is maximum in the area near the tool while, moving away from this, it decrease. For example, for the middle step, the temperature gradient near the tool is 9.1°C/mm while, at the edge of the plate, it is 2.35 °C/mm.

In order to accurately validated the numerical model, in Figure 4.13 it has been plotted the temperature vs. time of the experimental data and the numerical model. This represents the temperatures of a central point distant 16 mm from the centre (point A in Figure 4.9). The comparison shows generally a good agreement between the numerical results and the experimental data with some discrepancies in the cooling phase. This is due to the use of heat convection instead of heat conduction to simulate the interface between the specimen and backing plate and also the assumption of a constant temperature of the "simulated" backing plate. Actually, the temperature of the worktable rises during welding and this decreases the cooling rate of the weld. The maximum error between experimental and numerical data is 37.1% at the end of the cooling phase.

The permanence time at high temperatures and the cooling rate at a given point during welding is an important issue that conditions the mechanical properties, material microstructure formation and induces distortion in the ended welded structure [59]. In order to determine the permanence time at high temperature and because the typical aluminium temperature of recrystallization is between 200°C and 300°C, a temperature of 250°C has been chosen for discussion. This time, in the analysed case, is about 12 s. This value increase for lower speed of welding and then there is more time for the specimen to conduct the heat to the surrounding materials. This situation could lead to a larger heat affected zone and weld nugget.

The maximum temperature reached in the point A is 325.8 °C. This value is the same for both numerical and experimental data as result of the method used to determine the heat flow between specimen and backing plate. Finally, the model is validated and its results are good considering all the parameters, such as coefficient of convection, friction coefficient, variability of normal force, that are difficult to take into account.

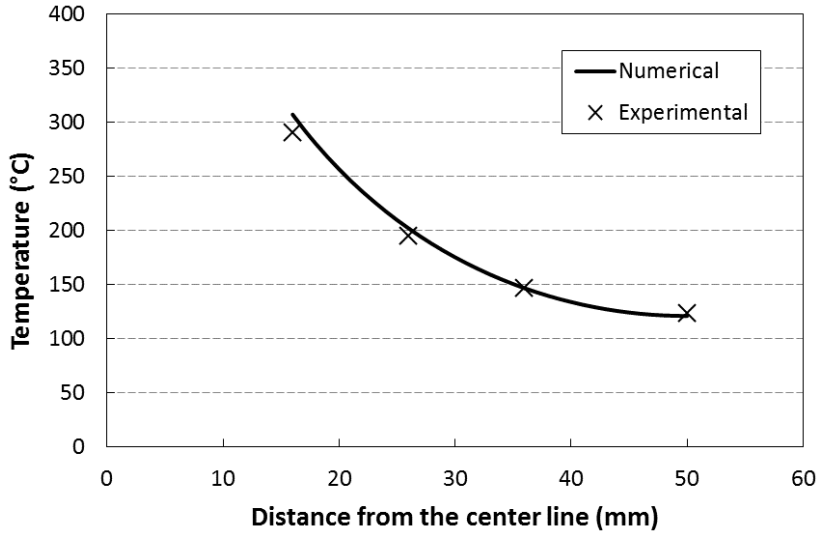

Figure 4.10 Temperature trend in the start phase

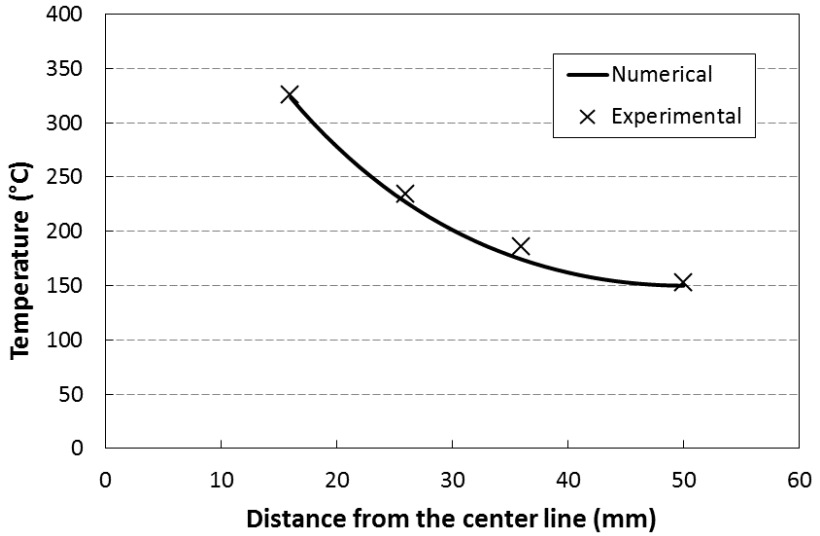

Figure 4.11 Temperature trend in the middle phase

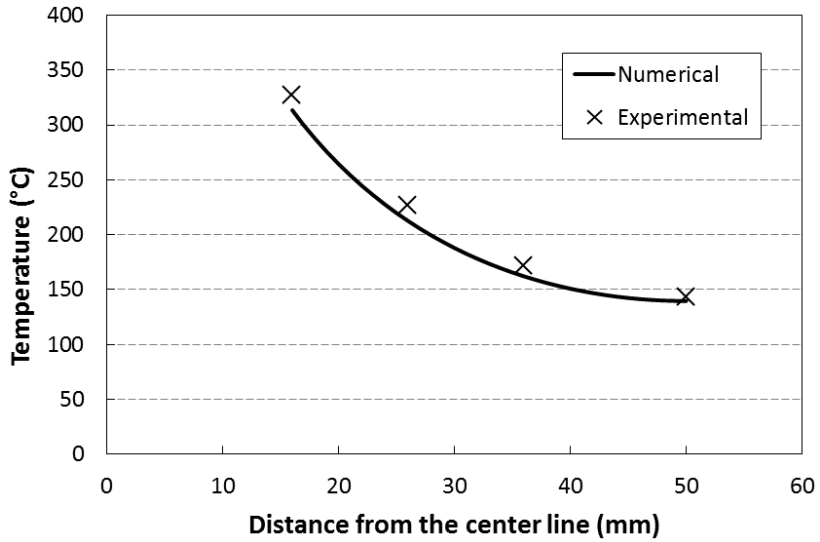

Figure 4.12 Temperature trend in the end phase

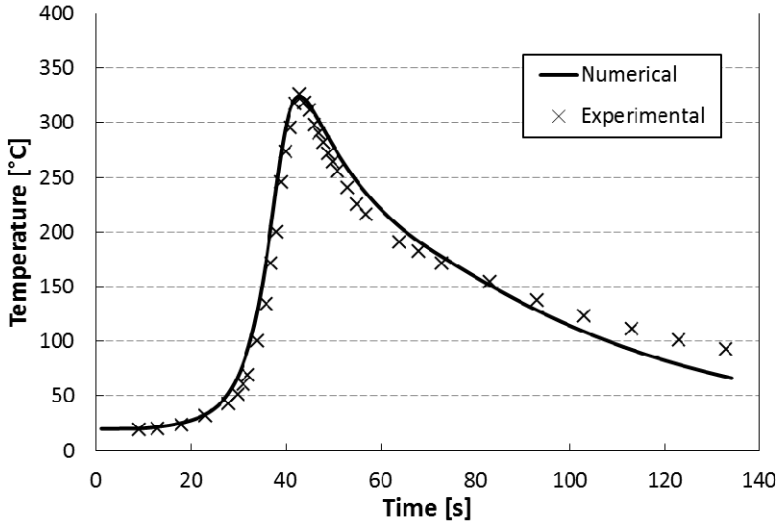

Figure 4.13 Temperature vs. time of a middle point distant 16 mm from the centre line

The Figure 4.14 shows the comparison between the numerical isothermals at the top surface of the specimen and the image of the surface temperature distribution taken by the infrared camera. The white area in this figure describes the zone of the plate where the temperature exceeds 250 °C. To describe and represent the data in a better way and because a semi-plate model has been made, the numerical results have been mirrored to the joint line in the next figure. Overall, there is a good agreement between the numerical and experimental data on the whole plate as highlighted in Figure 4.14. Only in the area near the clamping system, not implemented in the FEM model, the surface temperature is slight different.

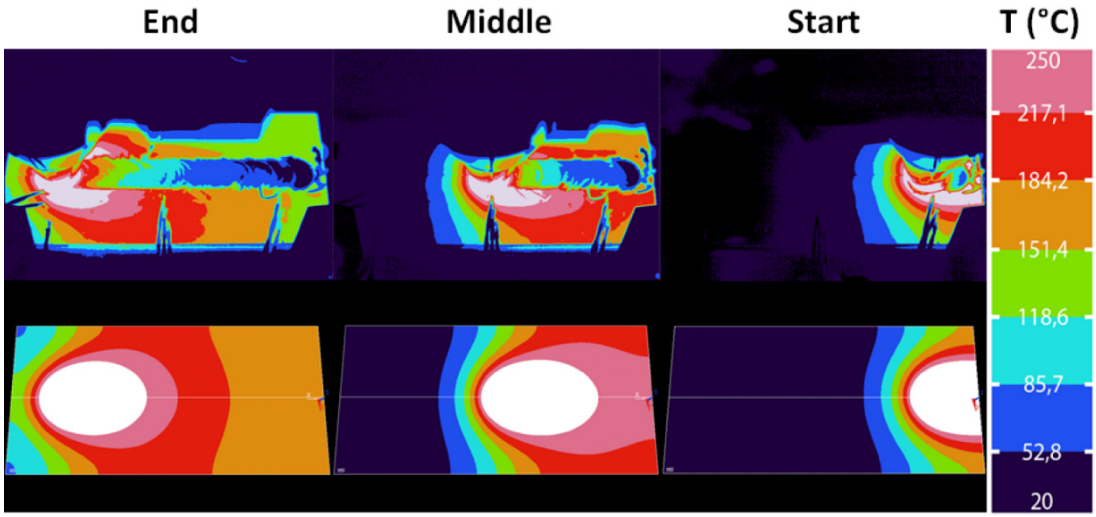

Figure 4.14 Graphical comparison between numerical data and the experimental ones

Figure 4.15 shows the calculated temperature contours (cross section) at the three steps analysed in this simulation. The figure illustrates the temperature distribution in the specimen during the tool pin crossing. The grey zone indicates the area which over 550°C. The highest temperature has been observed in the centre of the weld region where the rotation of the shoulder and probe

contributes the highest heat flux. In addition, the heat dissipation between the welded plate and the backing plate is higher than the dissipation between the top surface and air. This phenomenon causes the temperature contour in the weld nugget area to follow a "V" shape. At 20 mm from the weld centreline, the temperatures become uniform through thickness and the isothermal lines become almost vertical moving away from the centre line, according with that observed by Song et al. [57]. Figure 4.14 and Figure 4.15 show that detailed information can be provided by FEM model results also in areas (e.g. under tool shoulder, temperature fields in the plate) where the experimental data cannot provide information. This is one of the most important advantage of numerical modelling together with the possibility of predict thermo-mechanical behaviour of the joints that can be used for predict the best parameters for the weld process.

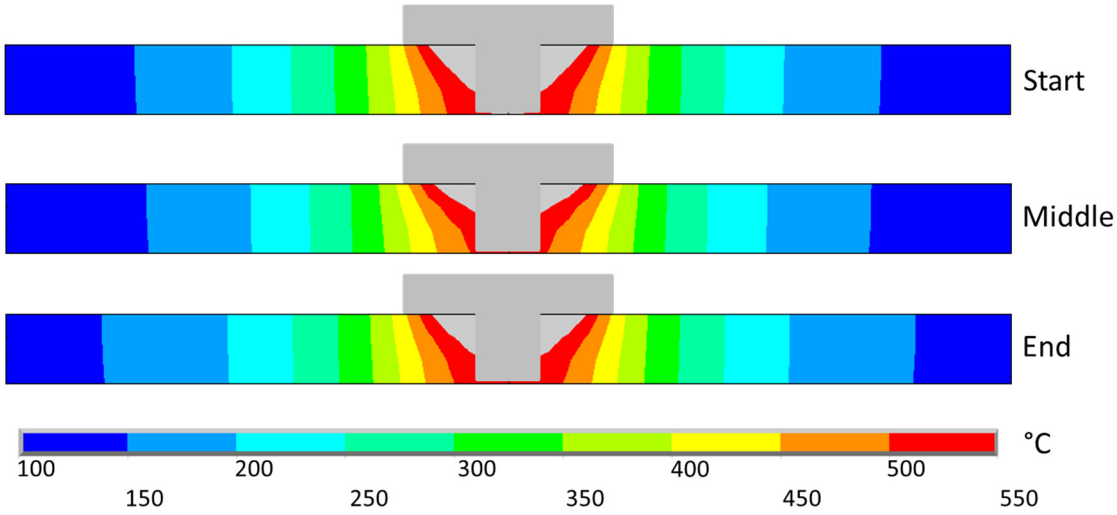

Figure 4.15 Comparison between model cross section of start, middle and end phase

- LASFW

In Figure 4.16 has been reported a scheme of the points that have been analysed to validate the thermal model. As in the previous showed results for FSW, also in this case three different steps have been studied and reported in the later graphs. The start position and the end position correspond to the initial and final welding phases and they are about 65 mm from the right and left edges of the plate respectively. Instead, the middle step is in the half of the specimen. For each position, the temperature has been measured at 16, 26, 36 and 50 mm from the welding line. The trends of the temperature versus distance from the weld line have been plotted for numerical and experimental data in the start (Figure 4.17), middle (Figure 4.18) and end (Figure 4.19) phase. Generrally, these graphs show that the temperature decreases moving away from the welding line and that the numerical model fits the experimental data with low errors. This is confirmed by R^2 value analysis defined as:

$$R^2 = 1 - \frac{SS_{res}}{SS_{tot}} \tag{4.2}$$

where SS_{res} is the sum of the squares of the distances between experimental data and the numerical curve, instead, SS_{tot} is the sum of the square of the distances of experimental values from a horizontal line through the mean of all Y values. The R^2 is 0.992 in the start step, 0.999 in the middle phase and, finally, 0.999 in the end step.

In order to accurately validate the FE model, in Figure 4.20 has been reported the temperature versus time of the experimental data and the numerical model. This graph represents the temperatures of a central point distant 16 mm from the welding line (point A in Figure 4.16). In general, there is a good agreement between the numerical model and the experimental data and, compared to the previous model, the adding of the baking plate improves the cooling phase prediction (Figure 4.13 vs. Figure 4.20)

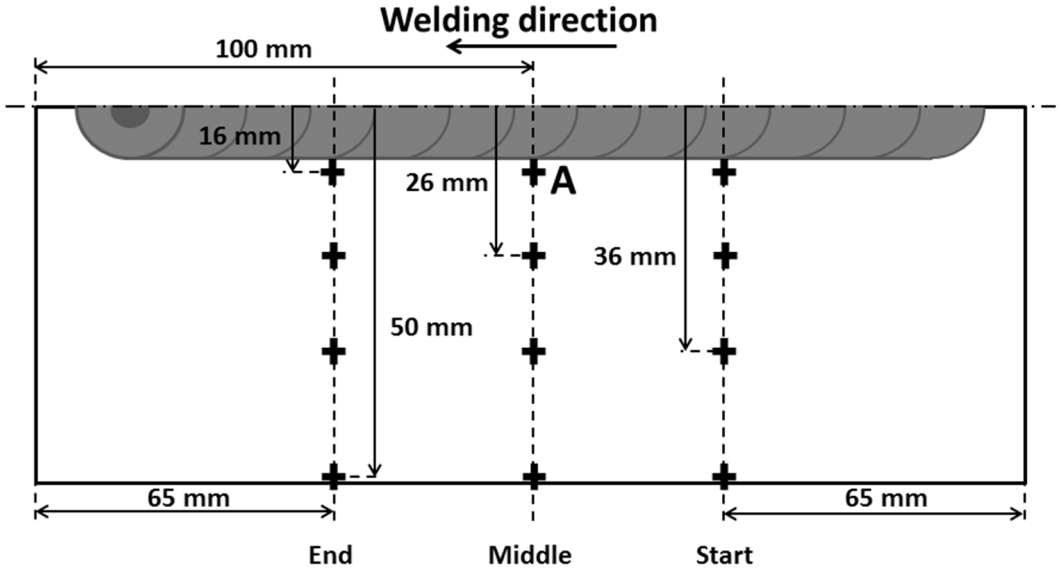

Figure 4.16 Scheme of temperature measured points

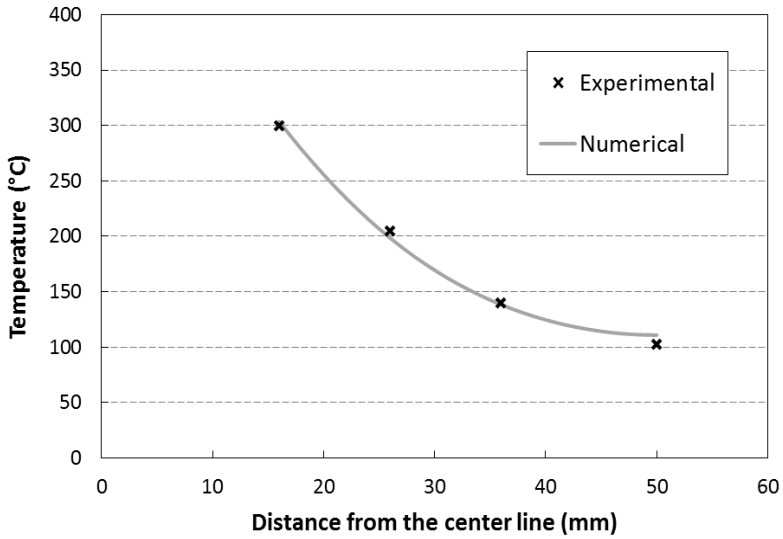

Figure 4.17 Numerical vs experimental data in the start phase

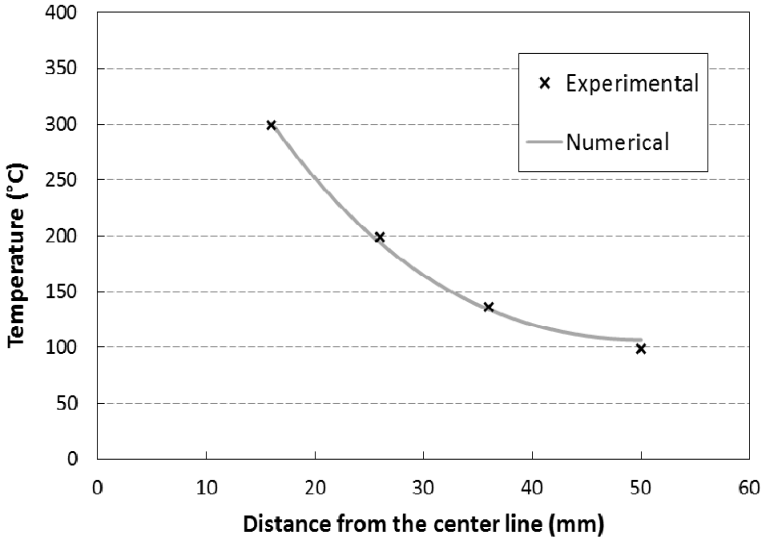

Figure 4.18 Numerical vs experimental data in the middle phase

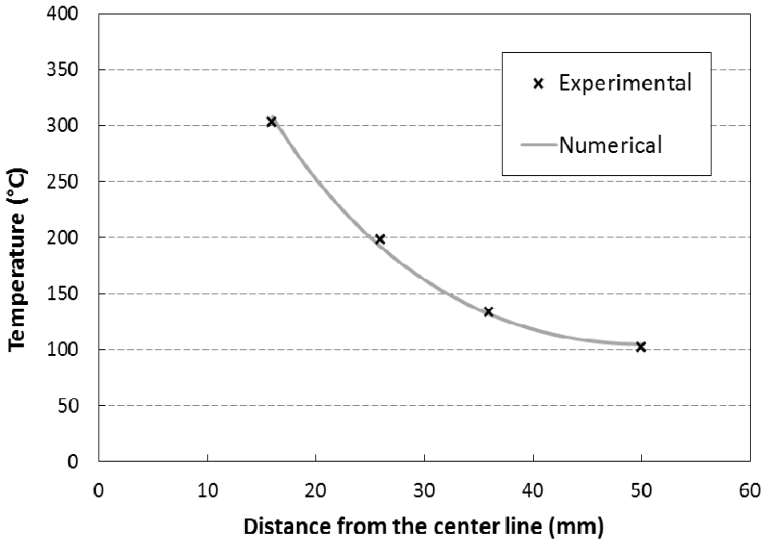

Figure 4.19 Numerical vs experimental data in the end phase

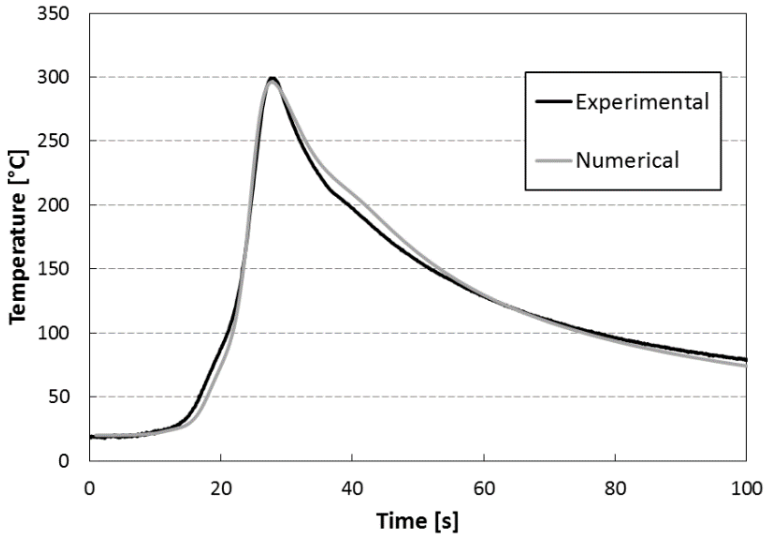

Figure 4.20 Temperature vs. time trend of the middle point A

The value of the thermal contact conductance coefficient, between the backing plate and the aluminium sheets, has been chosen in the way to fit the numerical maximum temperature in the point A with the experimental data.

In the Figure 4.21 has been reported a qualitative comparison of thermal field measured experimentally and that obtained numerically. The white area in the figure describes the zone of the specimen where the temperature exceeds 250 °C. Moreover, the temperature of welded area behind the FSW tool is not correct because there is a variation of the emissivity due to the paint removal and change of roughness after the transit of FSW tool. Finally, in order to present the results in better way and because only a semi-plate has been modelled, the numerical results have been mirrored along the joint line.

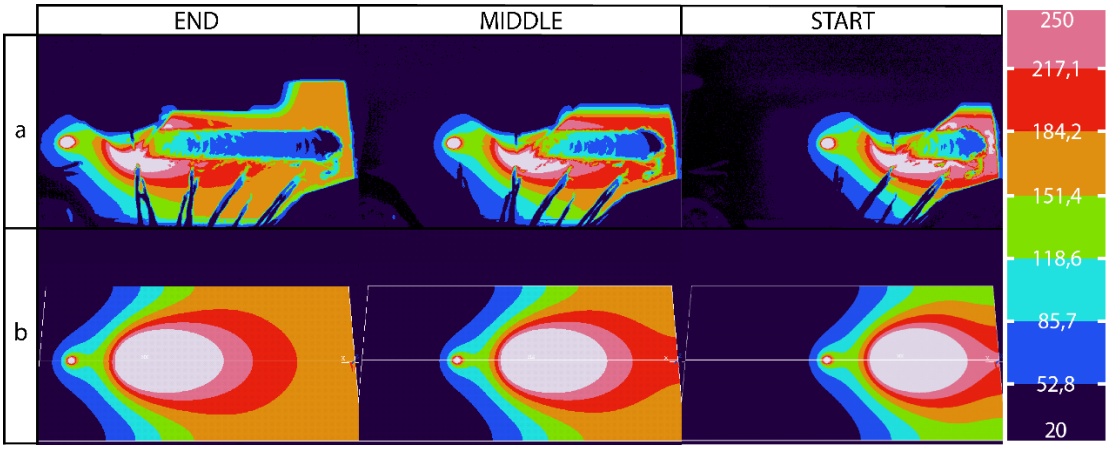

Figure 4.21 Graphical comparison between the experimental data (a) and numerical results (b)

4.3. Summary and conclusions

In this chapter, the influence on the temperature of the distance laser spot - FSW tool and of the laser source power has been investigated. In addition to the experimental results about LAFSW, the main characteristics and thermal results of the FSW and LAFSW numerical models have been presented.

In order to investigate the influence of the distance laser spot-FSW tool and of the laser source power on the temperature reached in the front zone tool, traditional FSW and three configurations of LAFSW bead on plate tests have been carried out. The welds have been done on 5754 H111 aluminium sheets with the dimensions of 200 mm length, 100 mm width and 6 mm thick. From the experimental results, it has been shown that, due to the high conductivity of aluminum, the distance of 40 mm is excessive (regardless of laser power) to produce a strong preheating effect on the specimens. Instead, the experimental measures show that a 20 mm distance is good choice for the aluminum alloy. The higher preheating effect with the 20 mm distance should reduce the residual stress in the welds in a stronger manner than that shown in the next chapter.

One of the most important advantage of numerical models is the possibility of predict temperature fields of the joints and to provide information on the whole plate where experimental data cannot give results. With this objective, two numerical models have been developed in order to predict the temperature fields in FSW and LAFSW. Both the numerical models have been validated and they can accurately describe the heat-transfer process. The difficulty in the prediction of the final cooling phase in the FSW model is due to the assumption of using heat convection instead of heat conduction and also of a constant temperature for the “simulated” backing plate. This issue has been overcome in the LAFSW model simulating also the backing plate and thus, its contribution to the heating and cooling phases.

Finally, as the heat dissipation between the welded plate and the backing plate is higher than the dissipation between the top surface and air, the temperature contour in the weld nugget area are not uniform but it follows a “V” shape with lower temperature on the bottom and higher on the top.

5. Residual stresses measurements in FSW processes

Residual stresses have a fundamental role in welded structures because they affect the way to design the structures, fatigue life, corrosion resistance and many other material properties. Consequently, it is important to investigate the residual stress distribution in FSW where, though the heat input is lower compared to traditional welding techniques, the constraints applied to the parts to weld are more severe.

Several papers have dealt with the residual stress distribution in FSW welds through experimental tests. Donne et al. [61] have measured residual stress distribution on FSW 2024Al-T3 and 6013Al-T6 welds by different techniques. They have shown that longitudinal and transverse residual stresses have a ‘‘M’’-like distribution across the weld. Furthermore, the longitudinal residual stresses are higher than the transverse ones regardless on tool rotation speed, pin diameter and traverse speed. Peel et al. [51] have reported a measurement of residual stress in FSW welded AA5083 specimens by synchrotron X-ray method, which shows that the weld bead is in tension in both the longitudinal and transverse directions. Moreover, they have shown that the longitudinal stresses increase with the traverse speed increase. Sutton et al. [62] have shown, according to Donne et al., that on 2024-T3 aluminium friction stir butt welds the longitudinal stress is the largest tensile component and that the transverse stress is about 70 percent of the longitudinal stress.

Though, many works on measuring residual stresses in FSW have been done, few works have been carried out on measuring or simulating residual stresses in innovative materials, configuration and techniques for FSW. In this chapter, the measurement of residual stresses in the LAFSW, in the in-process cooled FSW and in lap-joint aluminium-titanium welds will be done. These results will be useful in order to carry out a validation of the numerical model that will be presented in the chapter 6.

5.1. Residual stresses comparison between FSW and LAFSW

In this section a comparison of the residual stresses between the traditional FSW and the LAFSW will be done experimentally on aluminum 5754 H111 welds (see section 4.1.2 for material properties). The weld process has been carried out by the TISMA laboratory in Polytechnic of Bari. The weld process parameters have been selected according to the previous experiences of the TISMA laboratory.

5.1.1. Materials and methods

FSW and LAFSW tests were conducted on 6 mm thick 5754 H111 aluminium alloy plates, in butt joint configuration, with constant tool rotation and welding speed in order to compare the two processes and to evaluate changes in residual stress induced by laser pre-heating.

The FSW machine, equipped with an Ytterbium fibre laser source, is the same already presented in section 4.1.2. The laser has been positioned aligned with FSW pin in order to generate heating along the welding direction and has been located 40 mm forward of the tool. Two rectangular plates, 200 mm x 100 mm, has been welded perpendicular to the rolling direction. The welding process parameters have been reported in Table 5.1.

Table 5.1 Process parameters

Designation	**Traverse speed** [mm/min]	**Tool rotation speed** [rpm]	**Dwell time** [s]	**Laser power** [W]
1	20	500	3	–
1L	20	500	3	500
2L	20	500	3	1000
3L	20	500	3	2000

The residual stresses measures have been done employing a Xstress 3000 G3R Stresstech X-ray diffractometer. A Cr tube (λ = 0.2291 nm) powered with a 30 kV, 8 mA current and a 3 mm collimator has been used. A 2θ diffraction angle of 156.7° has been selected for the measures. In order to increase the quality of the measure, the stress in each point has been measured at five different angles (0°, ±22.5°, ±45°) with a φ oscillation of ±3°. The detection distance has been set at 75 mm. The residual stresses, both longitudinal (x axis direction) and transverse (y axis direction), have been carried out along the centre line of the specimens, i.e. the line normal to the welding line in the middle of the plate.

5.1.2. Results and discussion

In Figure 5.1, the longitudinal residual stresses have been reported. In general, for each test case, the longitudinal stress field shows a tensile region near the cord and a compressive area beyond 40 mm from the weld line. In particular, the traditional FSW (type 1 specimen) shows the typical "M-like" asymmetric stress field distribution near the bead [23]. The maximal stress value in tension is in the advancing side and it is over150 MPa.

Generally, the LAFSW plates show a reduction of the longitudinal residual stress close and into the bead in comparison with the traditional FSW. Away from the weld line, no significant differences have been found. The value of LAFSW longitudinal tensile stress into the bead is near to 90 MPa and it appears to be almost constant. Furthermore, this value seems to be independent from the increase of the laser power, as can be observed in specimen 1L, 2L and 3L. This effect could be explained considering that, although the laser power increases, the working temperatures near the tool remain the same as seen in section 4.1.3.

Figure 5.2 shows the transverse residual stresses within the weld as a function of distance from the weld line. In contrast with the longitudinal stresses, they do not display a direct dependence with the presence of the laser beam, indeed, the values are superimposable for all tested cases.

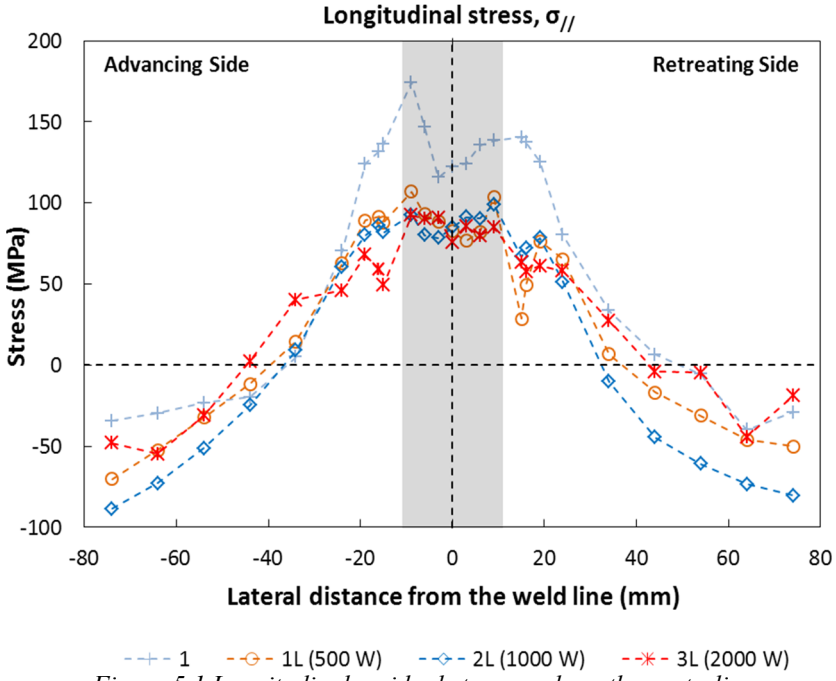

Figure 5.1 Longitudinal residual stresses along the centreline

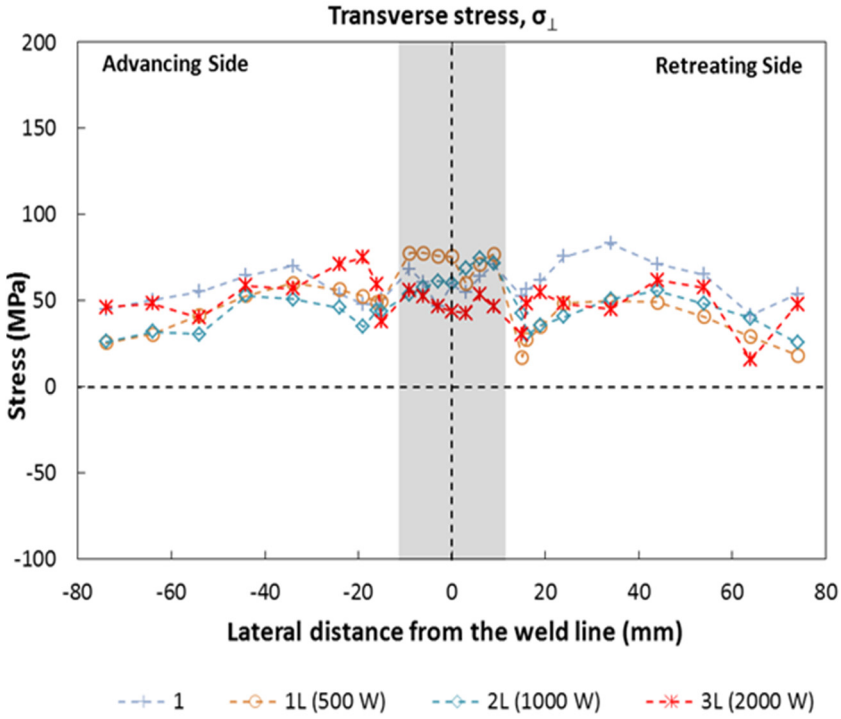

Figure 5.2 Transverse residual stresses along the centreline

5.2. Residual stresses comparison between in process cooled and traditional FSW

In this section, a comparison between the residual stresses in traditional FSW technique and in the in process cooled FSW has been reported. The weld process has been carried out by the colleagues of the Department of Chemical, Management, Computer Science and Mechanical Engineering of University of Palermo. The process parameters have been selected according to the previous experiences of the laboratory in Palermo.

The tests have been conducted on two aluminium 5754 H111 sheets (see section 4.1.2 for material properties), 200 mm length, 100 mm width and 6 mm thick joined in butt-weld configuration to make a 200 mm length and 200 mm width plate (Figure 5.3).

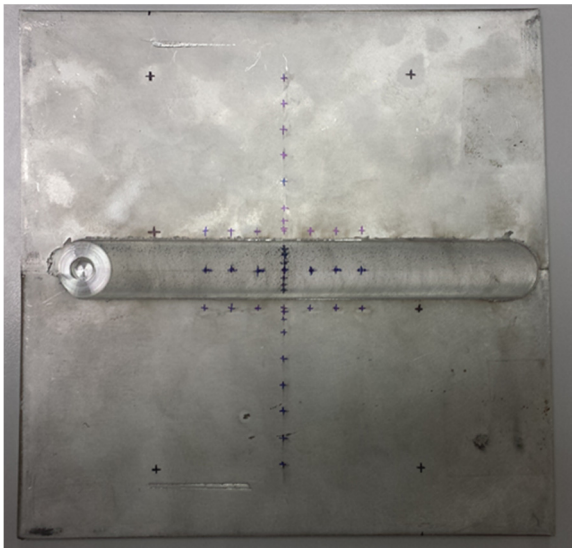

Figure 5.3 Butt-weld FSW plate

5.2.1. Materials and methods

The whole experimental campaign has been carried out with the same process parameters reported in Table 5.2. The only difference is the use of the water in the in process cooled FSW to cool down the weld immediately after the tool passage. The tool has a flat shoulder with a diameter of 21.5 mm and a cylindrical threated pin of 6 mm diameter and 5.8 mm height.

Table 5.2 Process parameters

Tool geometrical parameters	**Value**
Welding speed [cm/min]	20
Rotational speed [RPM]	500
Dwell time [sec]	3
Tilt angle [°]	2

The residual stresses measures have been done employing a Xstress 3000 G3R Stresstech X-ray diffractometer with the same setup explained in the previous section 5.1.1. The residual stresses, both longitudinal (x axis direction) and transverse (y axis direction), have been measured on each

point showed in Figure 5.4. In particular, the residual stresses measurements have been carried out along the centre line of the specimens, i.e. the line normal to the welding line, and along three lines parallel to the bead: the welding line, a line in the advancing and one in the retreating side at a distance of 15 mm from the welding line.

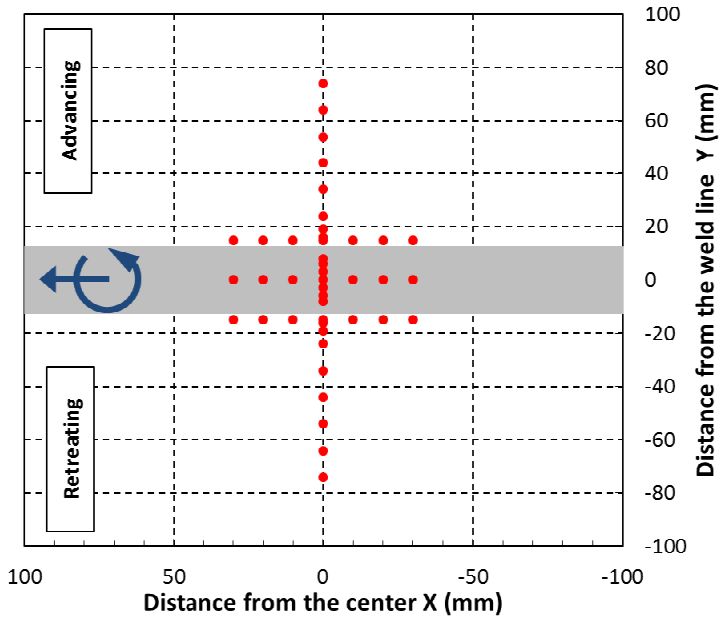

Figure 5.4 Points coordinates for the residual stress measurements

5.2.2. Results and discussion

In Figure 5.5 and Figure 5.6 have been reported the residual stresses comparisons, for both longitudinal and transverse directions, between FSW and in process cooled FSW. The grey area in the figures indicates the width of the bead.

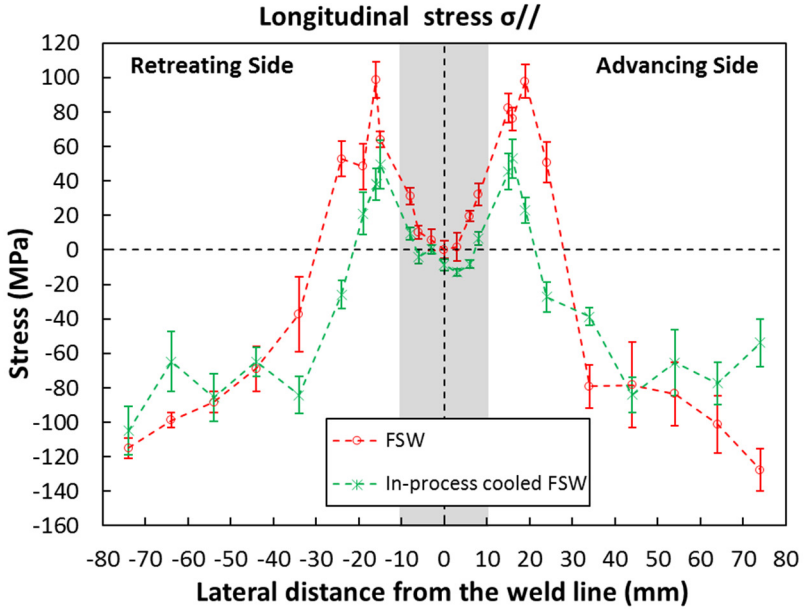

Figure 5.5 Comparison between longitudinal residual stresses in FSW and in-process cooled FSW

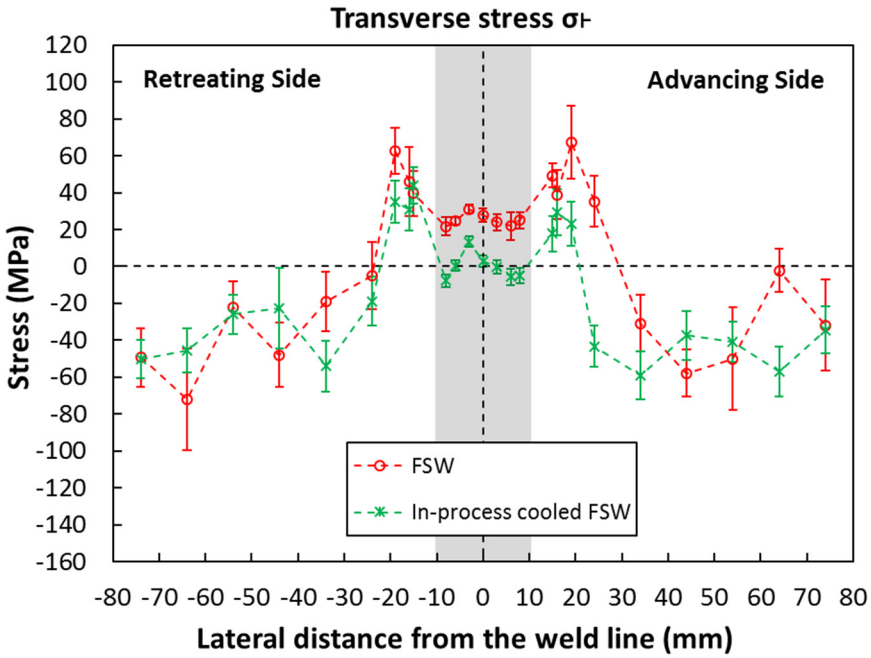

Figure 5.6 Comparison between transverse residual stresses in FSW and in-process cooled FSW

The previous figures highlight that the residual stresses are in general lower for the in process cooled FSW technique compared to traditional FSW for both the longitudinal and transverse residual stress. This is true in the welded bead, but is clearer outside the bead. For the longitudinal residual stress, beyond the distance of 40 mm from the welding line, the difference in the techniques is not significant but, between 10 to 30 mm, there is a 50% reduction in the residual stress values. On the other side, the transverse residual stress shows a greater reduction in the bead and comparable residual stress values beyond a distance of 20 mm from the welding line. Finally, the in process cooled FSW shows compression residual stress values in the bead and this should allow a longer fatigue life for this typology of joint.

In the Figure 5.7 has been reported the residual stresses trends, both longitudinal and transverse directions, for FSW and in process cooled FSW.

The advancing and retreating side measurements have been carried out on two lines parallel to the welding line and at a distance of 15 mm from this one. Finally, also these trends confirm that traditional FSW shows higher residual stresses than in process cooled FSW.

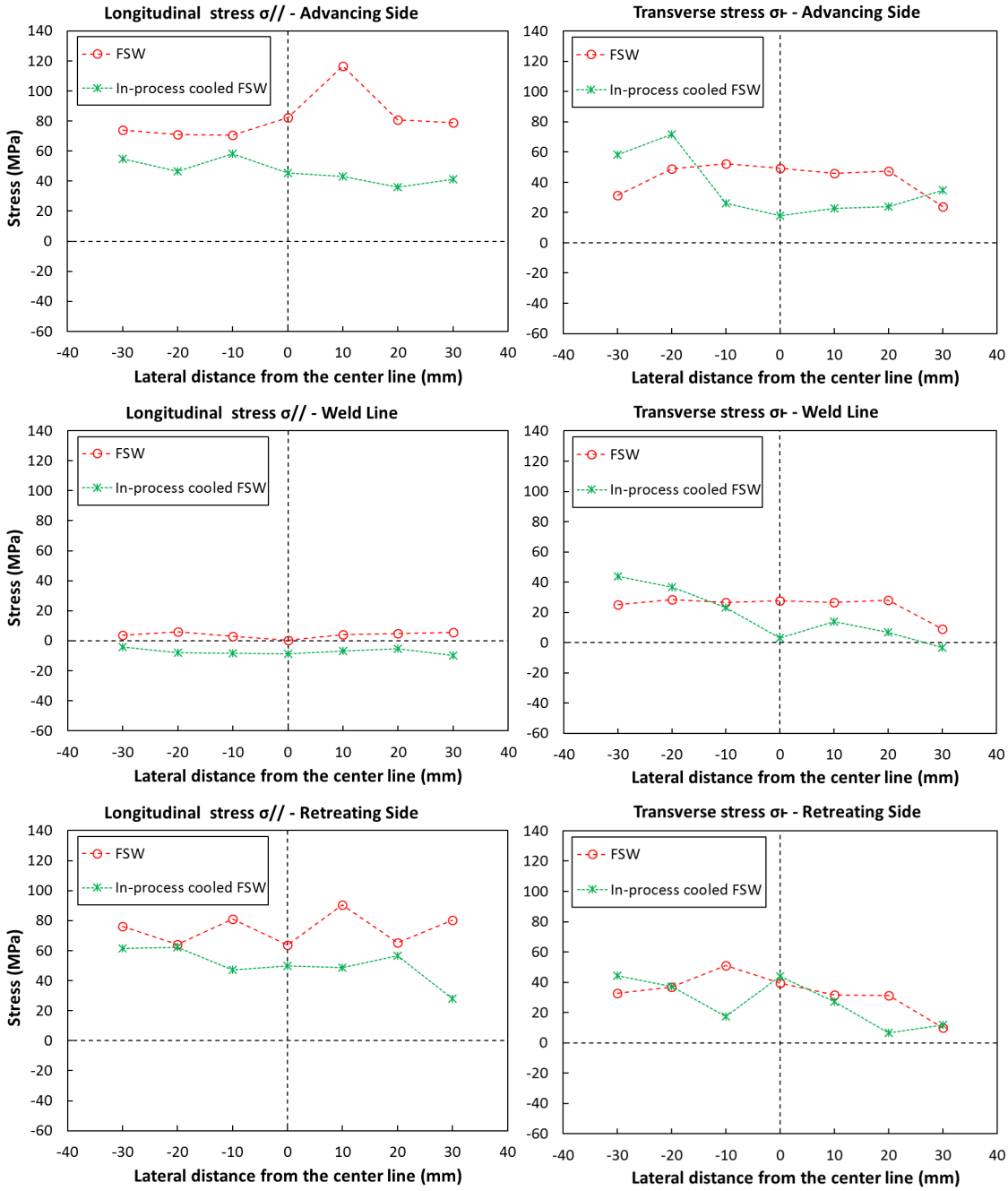

Figure 5.7 Residual stress in longitudinal and transverse directions for FSW and in process cooled FSW

In order to have a better and clear view of the residual stresses on the whole welded plate, in Figure 5.8 the 3D maps of the residual stresses for traditional FSW and in-process cooled FSW have been plotted.

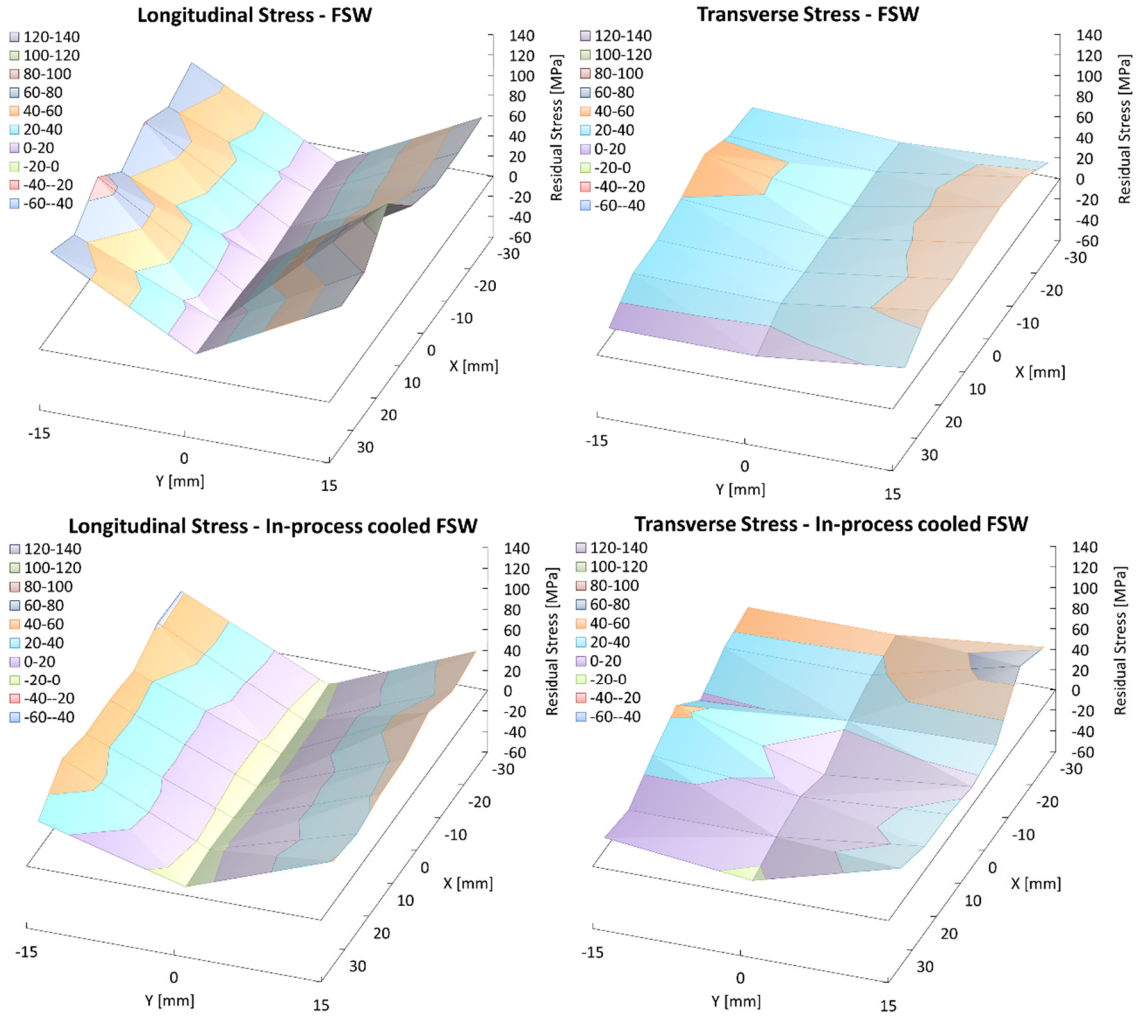

Figure 5.8 3D maps of the residual stresses for traditional FSW and in-process cooled FSW

5.3. Residual stresses measurements in FSW Al-Ti lap joints

In this section, the influence of the welding speed on the residual stresses in aluminium-titanium lap joints has been reported. The weld process has been carried out by the colleagues of the Department of Chemical, Management, Computer Science and Mechanical Engineering of University of Palermo. The process parameters have been selected according to the previous experiences of the laboratory in Palermo.

The tests have been conducted welding a 2 mm thick aluminium 6016 sheet on 1 mm thick titanium Ti-6Al-4V sheet. In Figure 5.9 the image of the actual welded plate has been reported together with a detail of the welded bead.

a)  b)

Figure 5.9 Lap joint aluminium-titanium (a) and a detail of the welded bead (b)

5.3.1. Materials and methods

The measurements have been done both on the top of the plate (aluminium) and on the bottom (titanium). The rotational speed and the dwell time have been set to, respectively 700 RPM and 2 sec for the whole experimental campaign. On the other hand, the welding speed and weld force have been changed during the tests:

1. 50 mm/min and 8.0 kN;
2. 100mm/min and 9.5 kN;
3. 200 mm/min and 10 kN.

In Table 5.3 the main tool geometrical parameters have been summed up.

Table 5.3 Tool geometrical parameters

Tool geometrical parameters	**Value**
Pin shape	conical
Greater pin diameter [mm]	4
Smaller pin diameter [mm]	2,92
Pin height [mm]	2
Taper angle [°]	15
Shoulder diameter [mm]	16
Shoulder surface [mm^2]	200

In the Figure 5.10, an image of the tool employed to join the aluminium titanium lap-weld has been reported.

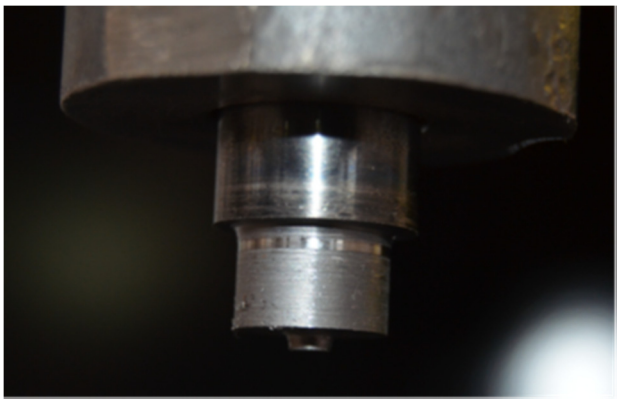

Figure 5.10 FSW aluminium-titanium tool

- *Aluminium measurements*

The residual stresses measures have been done employing a Xstress 3000 G3R Stresstech X-ray diffractometer with the same setup reported in the previous section 5.2.1. The Figure 5.11 sums up the points that have been measured on the top of the plate. As the previous section 5.2.1, both longitudinal (x axis direction) and transverse (y axis direction) residual stresses have been measured. Moreover, the residual stresses measurements have been carried out along the centre line of the specimens, normal to the welding line, and along three lines parallel to the bead: the welding line, a line in the advancing and one in the retreating side (both at 12 mm distance from the welding line).

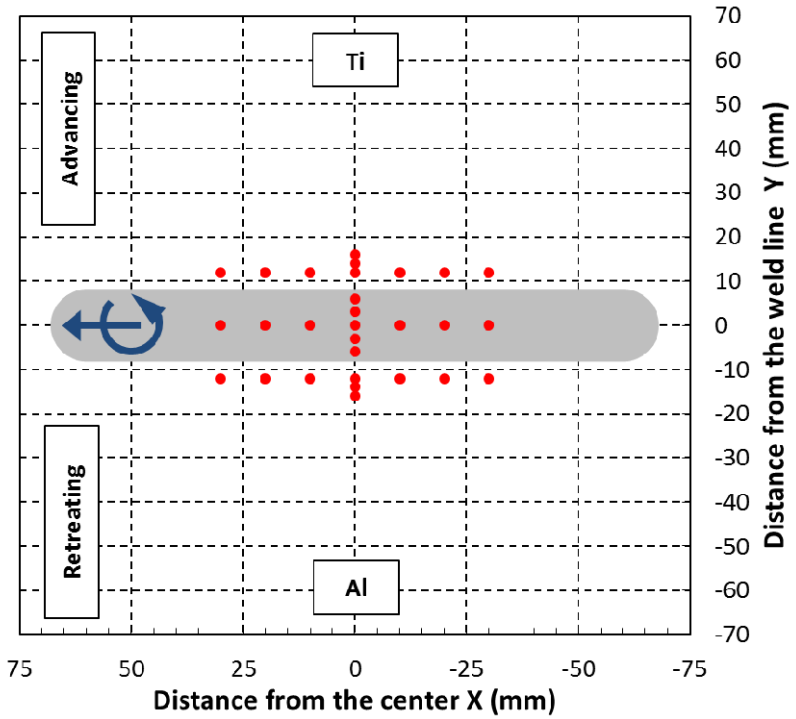

Figure 5.11 Points Coordinates for the residual stress measurements - aluminium

- *Titanium measurements*

Also the residual stresses measures on the back of the plate have been done by the Xstress 3000 G3R Stresstech X-ray diffractometer. However, as the analysed material is different, the setup of the machine shows some changes. In this case, a Ti tube powered with a 30 kV, 7 mA current and a 3 mm collimator have been employed and a 2θ diffraction angle of 137.4° has been selected for the measures. As the residual stress measurements on titanium alloy is quite difficult with x-Ray diffraction due to oxide presence on the material, the stress in each point has been measured at seven different angles (0°, ±24.09°, ±35.26°, ±45°) with a φ oscillation of ±3°. The detection distance has been set at 50 mm. As in the previous section, the longitudinal and transverse residual stresses have been measured on each point showed in Figure 5.12.

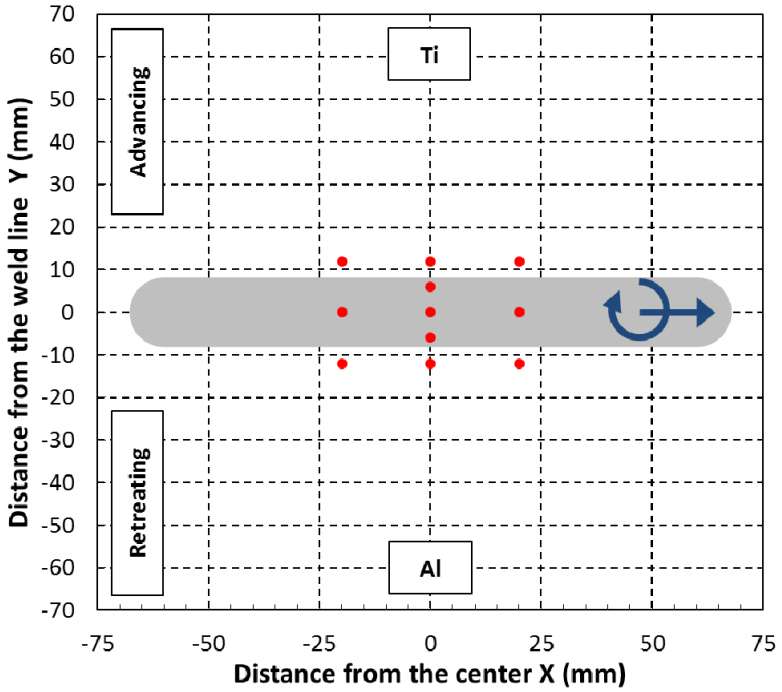

Figure 5.12 Points Coordinates for the residual stress measurements - titanium

5.3.2. Results and discussion

In this section the results from the x-Ray residual stress measurements has been reported. As the previous section, the results have been divided in measurements carried out on the top of the welded plate (aluminium measurements) and on the back (titanium measurements).

- *Aluminium measurements*

In Figure 5.13 and Figure 5.14 have been reported the residual stresses comparisons along a line normal to the welding line, for both longitudinal and transverse directions, among the three studied welding speeds. Also in this case, the grey area in the figures indicates the width of the bead. Each trend has been obtained as an average on three plates of the same type, i.e. same welding speed.

The longitudinal residual stress trends (Figure 5.13) do not highlight significant difference changing the welding speed because the three curves are virtually overlapped. On the other hand, the transverse residual stress (Figure 5.14) shows, on the welding line, some difference changing the process parameters. Higher compression residual stresses can be observed increasing the welding speed.

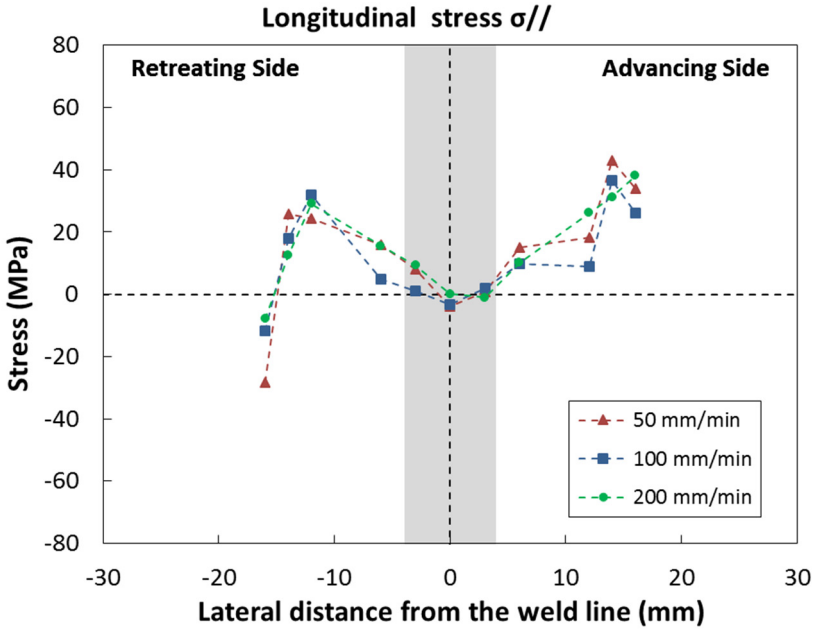

Figure 5.13 Longitudinal residual stress along a line normal to the welding line - aluminium

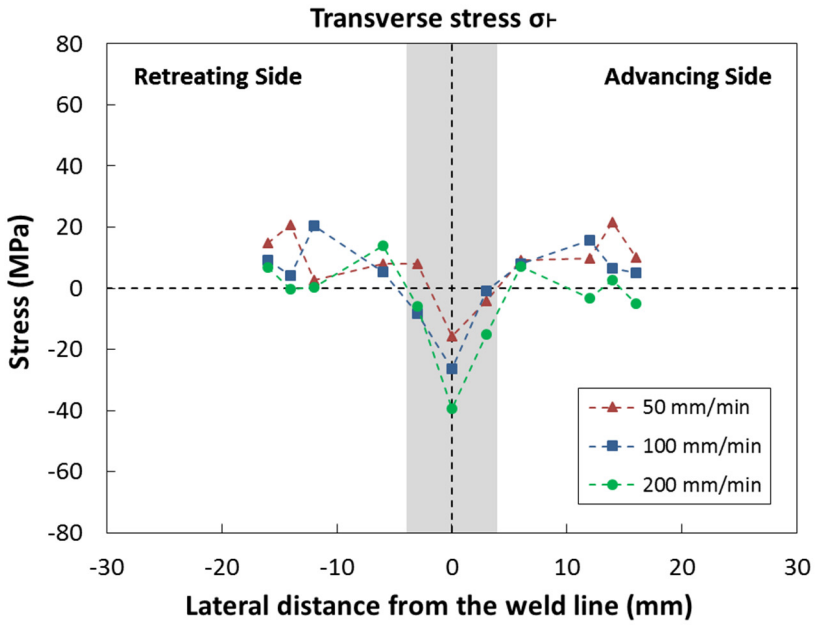

Figure 5.14 Transverse residual stress along a line normal to the welding line - aluminium

In the Figure 5.15 has been reported the residual stresses trends, both longitudinal and transverse directions, along the welding line and two other parallel lines, at a distance of 12 mm, in the advancing and retreating side. Also this trends confirm that there is no significant influence of the welding speed on the residual stress.

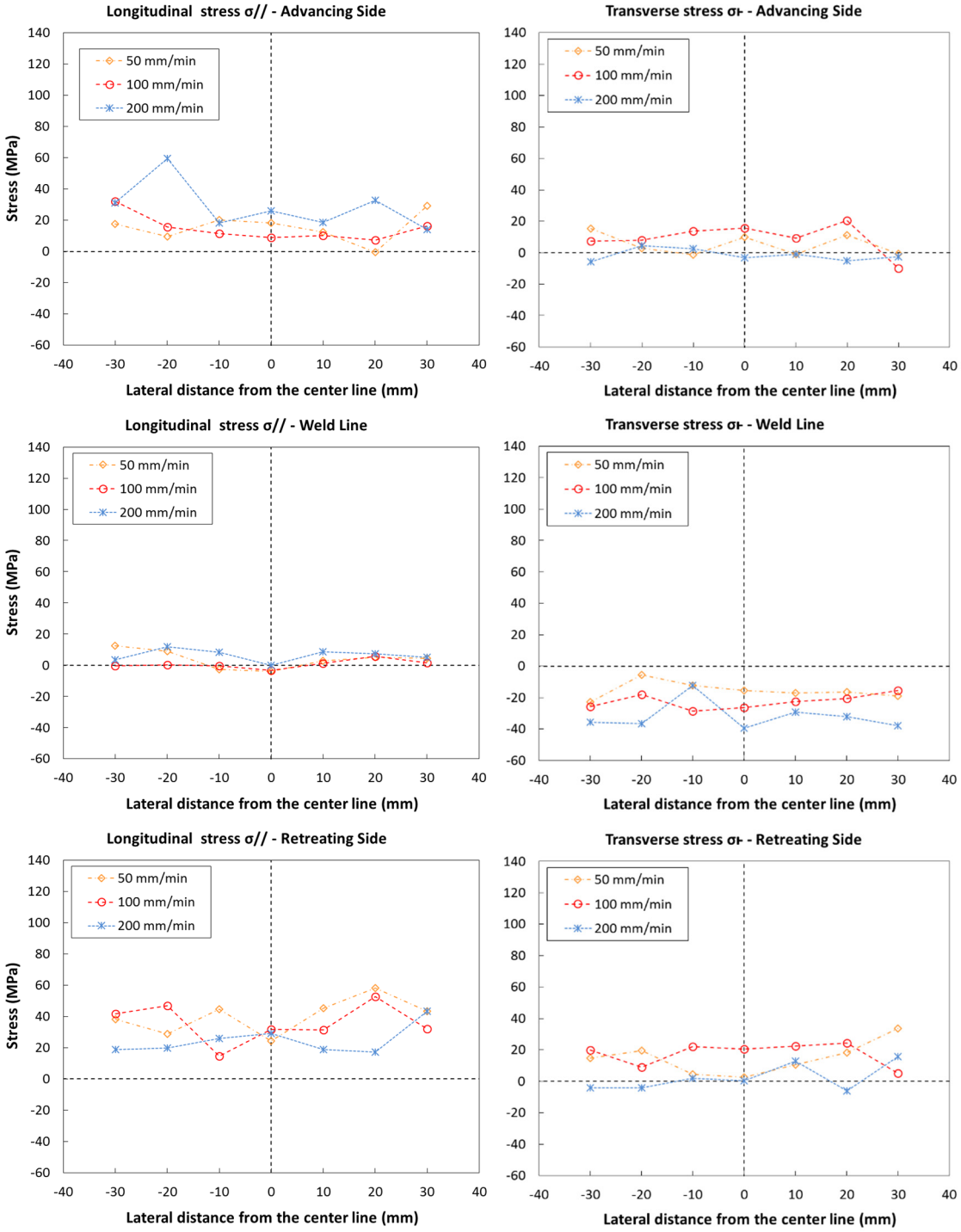

Figure 5.15 Residual stress in longitudinal and transverse directions changing the welding speed – aluminium

In order to have a better and clear view of the residual stresses on the whole welded plate, in Figure 5.16 the 3D maps of the residual stresses for the three tested speeds have been plotted.

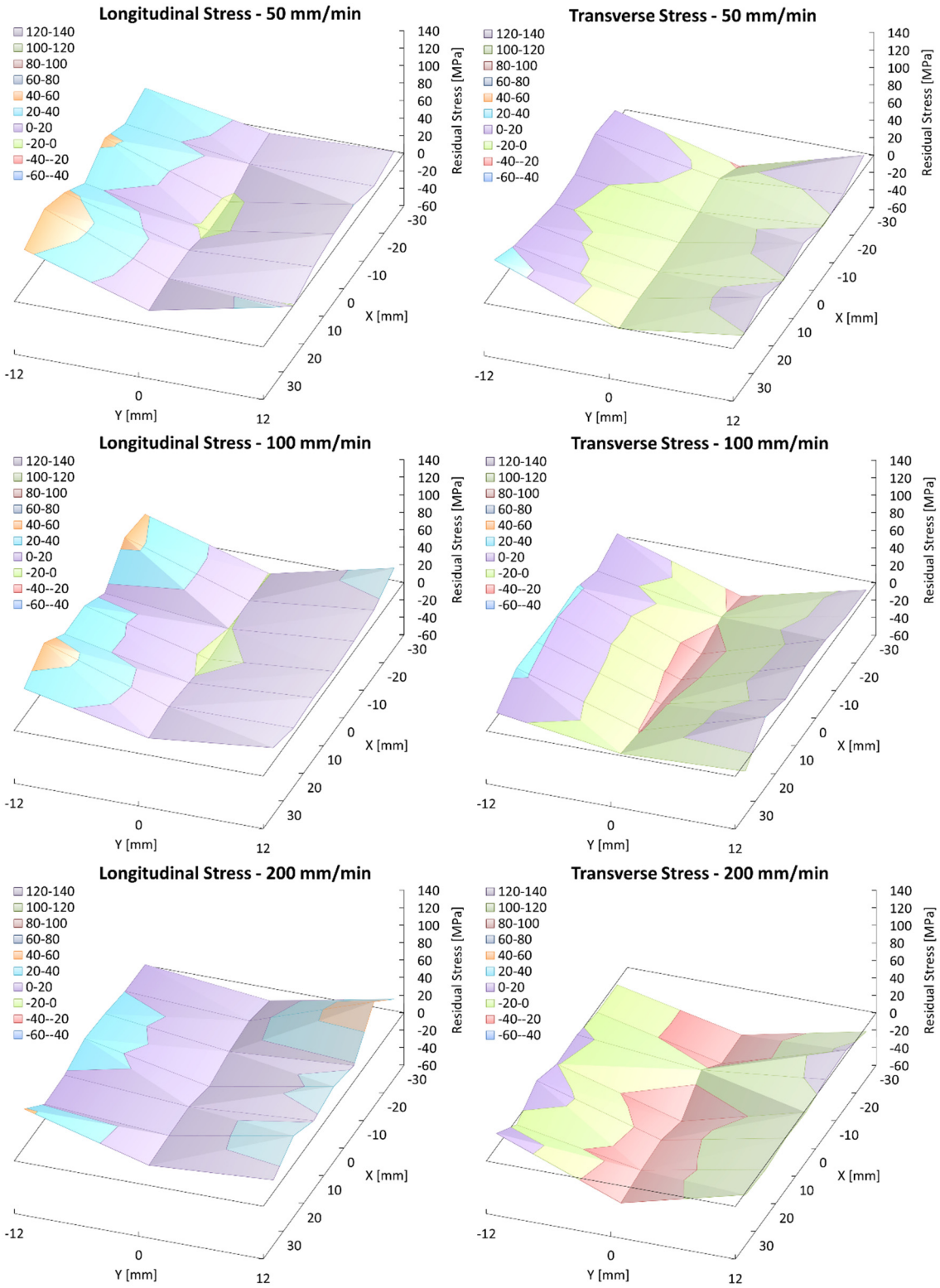

Figure 5.16 3D maps of the residual stresses changing the welding speed - aluminium

- *Titanium measurements*

In Figure 5.17 and Figure 5.18 have been reported the residual stresses comparisons along the normal to the welding line, for both longitudinal and transverse directions, among the three studied welding speeds.

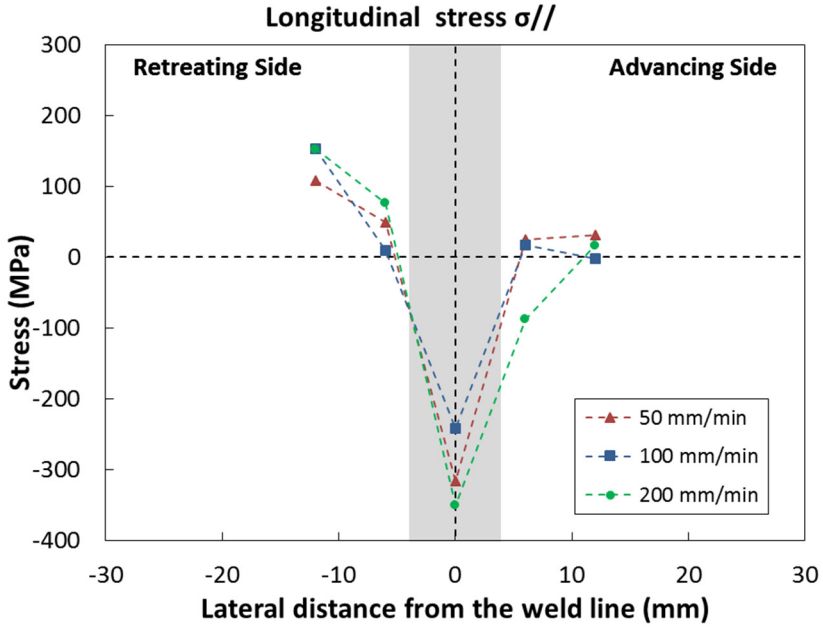

Figure 5.17 Longitudinal residual stress along the normal to the welding line - titanium

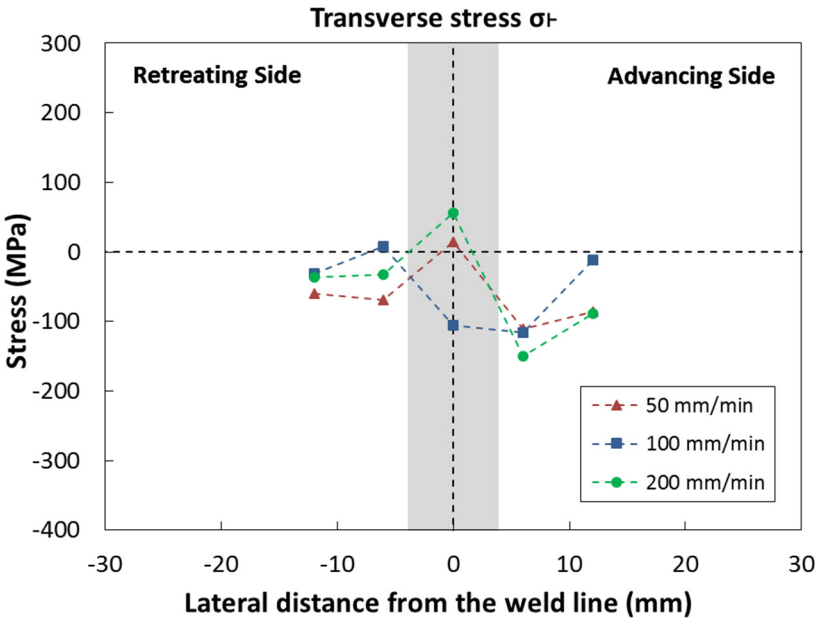

Figure 5.18 Transverse residual stress along the normal to the welding line - titanium

Also in the back of the plate, for both longitudinal and transverse residual stresses trends, there is no significant difference changing the welding speed. In the longitudinal direction, can be observed high compressive residual stresses in the central zone and this is probably due to the effect of the pin. Finally, the transverse direction shows compressive stress in general.

In the Figure 5.19 has been reported the residual stresses trends, both longitudinal and transverse directions, along the welding line and two other parallel lines, at a distance of 12 mm, in the advancing and retreating side. Also this trends confirm that there is no significant influence of the welding speed on the residual stress.

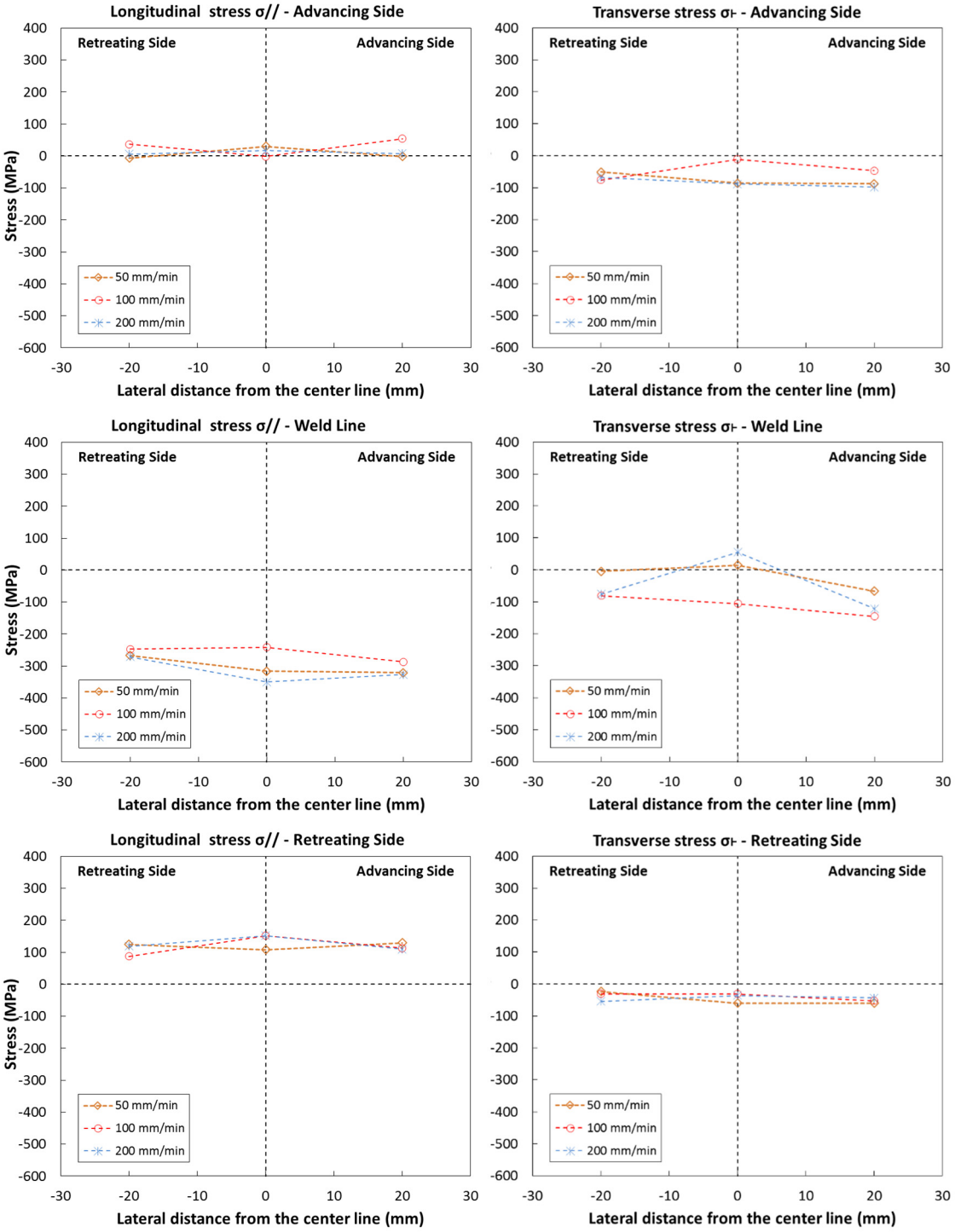

Figure 5.19 Residual stress in longitudinal and transverse directions changing the welding speed – titanium

Also for the titanium, in Figure 5.20, the 3D maps of the residual stresses for the three tested speeds have been plotted.

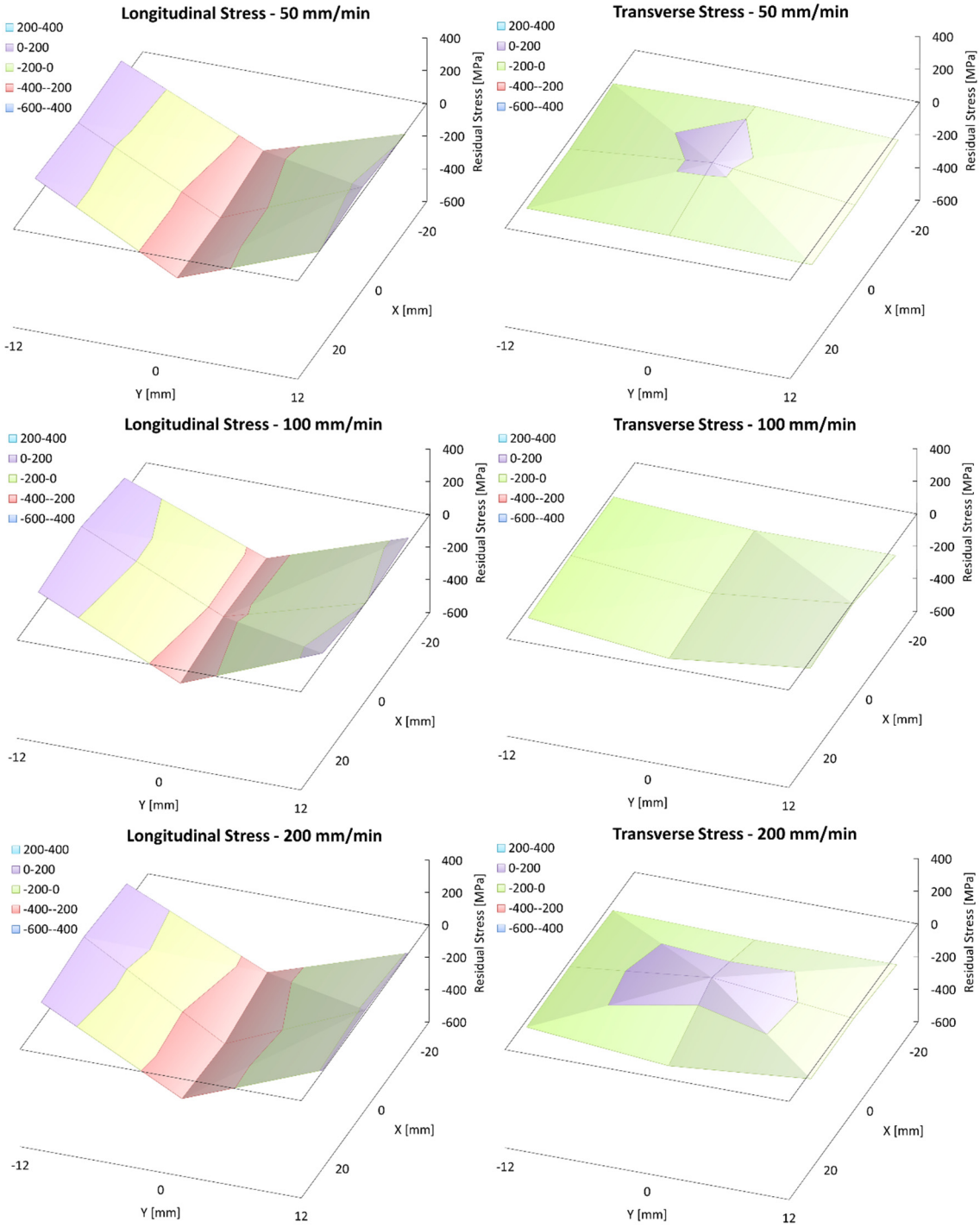

Figure 5.20 3D maps of the residual stresses changing the welding speed – titanium

5.4. Summary and conclusions

In this chapter, the residual stresses measurements in FSW innovative processes and material has been addressed. In particular, the measurement of residual stresses in the LAFSW, in the in-process cooled FSW and in lap-joint aluminium-titanium welds have been done.

From the comparison of traditional FSW and LAFSW, it has been found that the laser pre-heating induces lower longitudinal residual stress in the bead surface. However, the help of the laser does not produce any appreciable reduction in the magnitude of the transverse residual stresses. Moreover, the changes in laser power do not affect both the longitudinal and transverse residual stresses.

The results for comparison between traditional FSW and the in-process cooled FSW show that the residual stresses are in general lower for the in-process cooled FSW technique compared to traditional one for both the longitudinal and transverse residual stress. This is true in the welded bead, but is clearer outside the bead. For the longitudinal residual stress, away from the welding line (beyond the distance of 40 mm), the difference in the techniques is not significant but, between 10 to 30 mm, there is a 50% reduction in the residual stress values. On the other side, the transverse residual stress shows a greater reduction in the bead and comparable residual stress values beyond a distance of 20 mm from the welding line. Finally, the in-process cooled FSW shows compression residual stress values in the bead and this should allow a longer fatigue life for this typology of joint.

The influence on the residual stresses of the welding speed has been studied in the FSW lap-joint aluminium-titanium. The comparison among the three different speeds show that, for the longitudinal residual stress, there is not significant difference changing the welding speed because the three curves are virtually overlapped. On the other hand, the transverse residual stress shows, on the welding line, some difference changing the process parameters. Higher compression residual stresses can be observed increasing the welding speed. Also the residual stresses trends, both longitudinal and transverse directions, along the welding line and two other parallel lines, at a distance of 12 mm, in the advancing and retreating side confirm that there is no significant influence of the welding speed on the residual stress. In the back of the plate, for both longitudinal and transverse residual stresses trends, there is no significant difference changing the welding speed. In the longitudinal direction, can be observed high compressive residual stresses in the central zone and this is probably due to the effect of the pin. Finally, the transverse direction shows compressive stress in general.

6. Residual stresses prediction in FSW processes

With the purpose of a clearer understanding of the FSW process, in recent years, some researchers have studied the development of FSW numerical models. Furthermore, besides a deeper knowledge of FSW, these numerical simulations have also the aim to guide the development of the process through the research of optimal parameters minimizing the amount of trial and error. Khandkar et al. [63] have made an uncoupled thermo-mechanical model for some aluminium alloys and 304L stainless steel based on torque input for calculating temperature and then residual stress. Chen et al. [64] have developed a three-dimensional numerical model based on a finite element method to study the thermal impact and evolution of the stresses in the weld. Many of these numerical are only thermal model or thermo-mechanical models in which it is not considered the mechanical force that the tool exerts on the workpiece. These should be included into the thermo-mechanical model because FSW is mainly a mechanical process and the forces involved in this type of work are relevant.

In this chapter, the numerical model to predict residual stresses in FSW and LAFSW will be presented and a study on the influence of the clamps configuration on residual stresses will be carried out.

6.1. Prediction of residual stresses in FSW and influence of the clamp configuration

In this section, a numerical model that can predict the residual stresses in FSW will be presented. Moreover, the correlation between the residual stress field and configurations of clamps will be established numerically. Indeed, due to thermal expansion during the FSW process, as the welding structure is fully constrained, high stresses and also yielding can be produced in the material. Therefore, it will be shown that a particular attention to the choice of the boundary conditions should be done to avoid over constraining the thermal expansion.

6.1.1. Materials and methods

The FSW process has been carried out joining, in butt-weld configuration, two 200 mm x 100 mm x 6 mm AA5754-H111. The material chemical composition, thermo-physical properties, and mechanical characteristics at room temperature are the same of the properties reported in the chapters 4. The tool scheme, experimental setup, etc. are the same of that reported in section 4.2.2. The process parameters are the same reported in section 5.1.

The residual stresses measurements have been carried out employing the Xstress 3000 G3R Stresstech X-ray diffractometer with the same setup explained in section 5.1.1. As mentioned in section 4.2.2, the temperature measurement but also the residual stresses analysis and then

numerical simulation have been carried out for the retreating side of the FSW welded plate, because the configuration of the FSW machine prevents access to both sides.

6.1.2. Numerical model description

An uncoupled FE model has been carried out to calculate residual stress field. At first, a thermal analysis has been conduct to calculate the temperatures history due to the welding process. Then the calculated temperature field has been used as thermal input to the mechanical model to predict the residual stresses and strains. For this simulation, the finite elements commercial code ANSYS 14.5 has been used and the thermal simulation is based on the previously presented model in section 4.2.1 modified to describe the welding process of two 200 mm x 100 mm plates in butt-weld configuration. With the aim of an accurate simulation of residual thermal stresses, beyond the temperature dependent thermo-physical properties reported in Table 4.4 also temperature dependent thermo-mechanical properties have been used (Table 6.1). Because the FSW is a solid-state welding process, it has been assumed that there is no material melting. Consequently, enthalpy values are not considered in this model. Moreover, a multi-linear isotropic hardening has been adopted to describe the behaviour of the material.

Table 6.1 Temperature dependent thermo-mechanical properties for AA5754-H111 [60]

Temperature [°C]	**Thermal expansion** [m/m°C]	**Young's Modulus** [GPa]	**Poisson's ratio**
20	23.90 E-6	103.4	0.34
100	24.40 E-6	-	0.34
200	25.13 E-6	97.88	0.35
300	26.15 E-6	42.11	0.365
400	27.15 E-6	23.07	0.365
500	28.15 E-6	-	0.34

In the second step of the thermo-mechanical analysis, the thermal histories simulated by the FE thermal model have been inputted in the mechanical simulation to calculate the stresses. To this aim, the SOLID186 elements have been used instead of the SOLID90 elements but keeping the same mesh and load step size. Moreover, in this model, also the mechanical effect due to the compression force applied by the tool has been taken into account. To simulate this force, a uniform axial pressure distributed on tool area has been included in the FE Mechanical model.

Initially, the mechanical constrains have been set according with experimental set up (blue area in Figure 6.1) constraining a 4×43 mm^2 area for the left and right clamp.

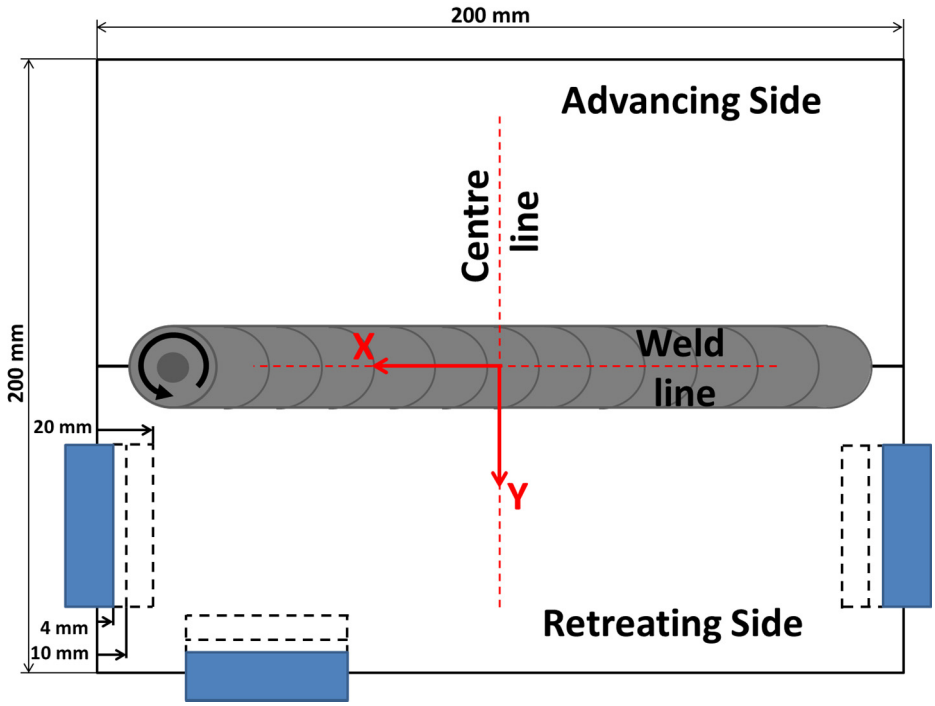

Figure 6.1 Specimen and clamping system scheme

For the below clamp a 4×45 mm^2 area has been constrained. Subsequently, the constrained area in the numerical models has been increased in the same manner for all three clamps (10 and 20 mm dotted lines in Figure 6.1) to evaluate the effect of boundary condition on residual stress field. The constraints on the top surface of the specimen block the movements in all direction. Moreover, the bottom of the plate has been constrained in z-direction. Once that the welding simulation is concluded, the constraints are gradually released and the residual stresses due to FSW process have been evaluated.

The FSW has been carried out along the welding line reported in Figure 6.1 that was perpendicular to the rolling direction of the AA5754 sheets. Temperature measurement, residual stresses analysis, and then numerical simulation have been carried out for the retreating side of the FSW welded plate. Due to the layout of the FSW machine, it was not possible to acquire the temperatures of both the advancing and retreating side.

6.1.3. Results and discussion

In order to obtain plausible stress values in the simulated cases with different constraints, the previously described model has been validated on both temperatures and stresses for the actual case. To reach this aim, the temperature field of the specimen have been measured during the FSW test by an infrared thermo-camera. In the same way, as in the section 4.2.3, the recorded values have been compared with the data calculated by the numerical model. The temperature gradient obtained by the numerical simulation has been compared with that measured experimentally in three different position when maximum (Figure 6.2), i.e. start, middle and end

step. The start position and the end position correspond to the initial and final welding phases and they are about 50 mm from the right and left edges of the plate respectively. Instead, the middle step is in the half of the specimen. For each position, the temperature has been measured at 16, 36, 80 and 100 mm from the welding line.

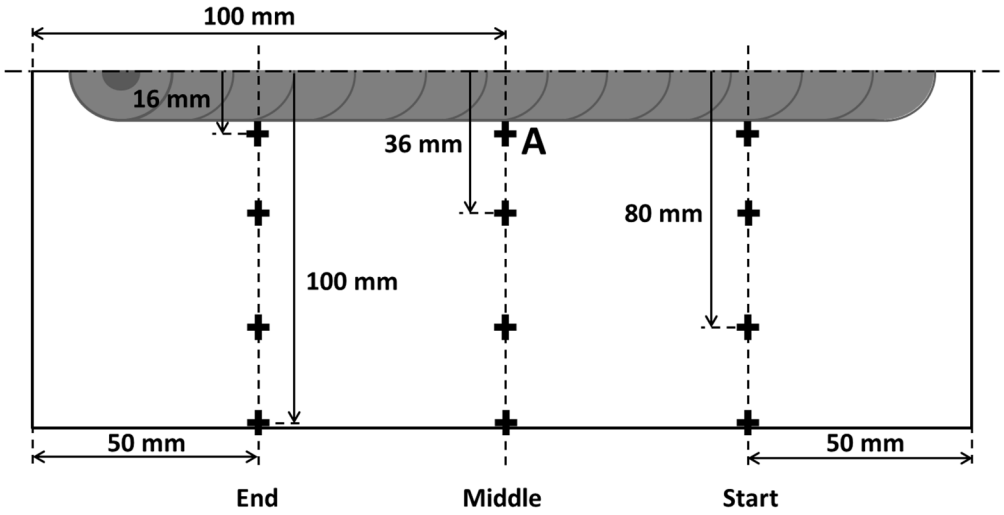

Figure 6.2 Scheme of temperature measured points

In Figure 6.3, Figure 6.4 and Figure 6.5 the graphs of the temperature versus distance from the weld line have been plotted both for numerical and experimental data. Generally, the numerical data show a good agreement with the experimental measurements. This is confirmed by R^2 that is 0.997 in the start step (Figure 6.3), 0.999 in the middle phase (Figure 6.4) and, finally, 0.991 in the end step (Figure 6.5).

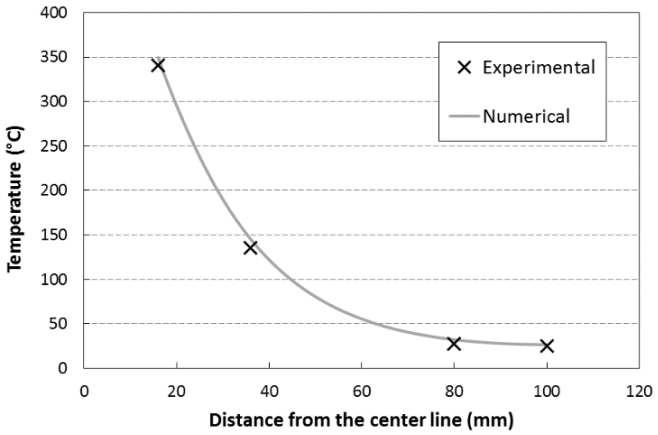

Figure 6.3 Numerical vs experimental data in the start phase

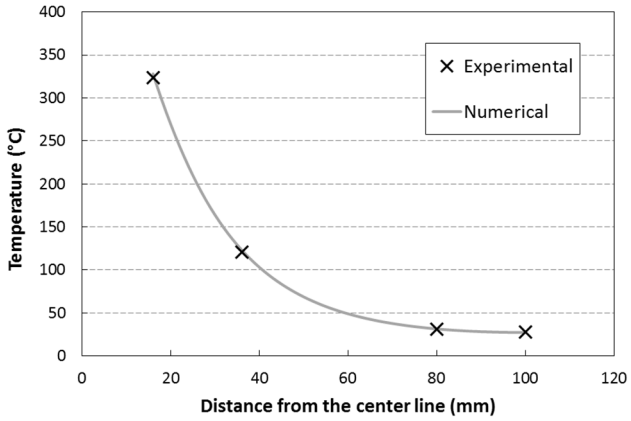

Figure 6.4 Numerical vs experimental data in the middle phase

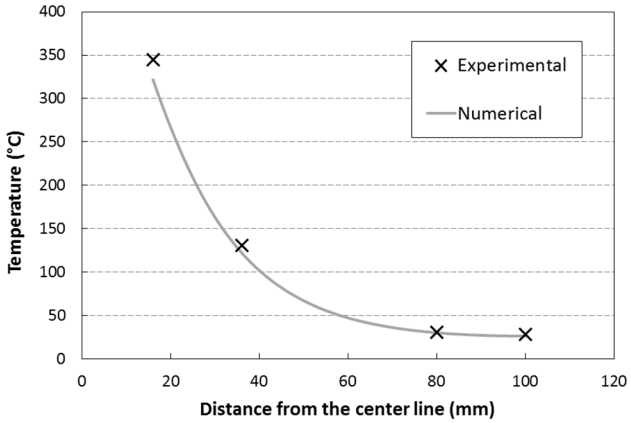

Figure 6.5 Numerical vs experimental data in the end phase

The trend of temperature versus time for both numerical model and experimental data has been plotted in Figure 6.6. This graph shows the temperatures of the central point indicated by A in Figure 6.2. In general, there is a good agreement between the numerical model and the experimental data with some difference in the heating and cooling phase as already explained in section 4.2.3.

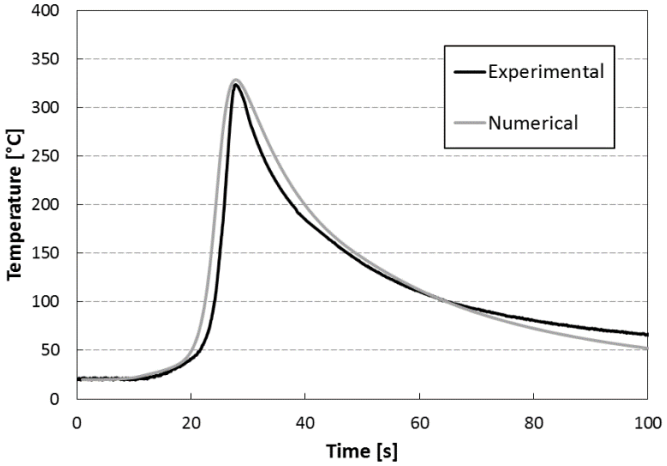

Figure 6.6 Temperature vs. time trend of the middle point A

The mechanical part of the model has been validated based on the X-Ray diffraction stress data presented in section 5.1.2. These superficial measures have been compared with the numerical model prediction. In Figure 6.7 the stress in the welding direction, i.e. the longitudinal stress, has been reported and compared with the numerical values. The longitudinal stress shows a ‘‘M’’-like distribution across the weld and, moreover, the maximum stress value in a FSW weld is located on the edge of the bead described in the Figure 6.7 by the vertical grey line at a distance of 10.75 mm from the welding line.

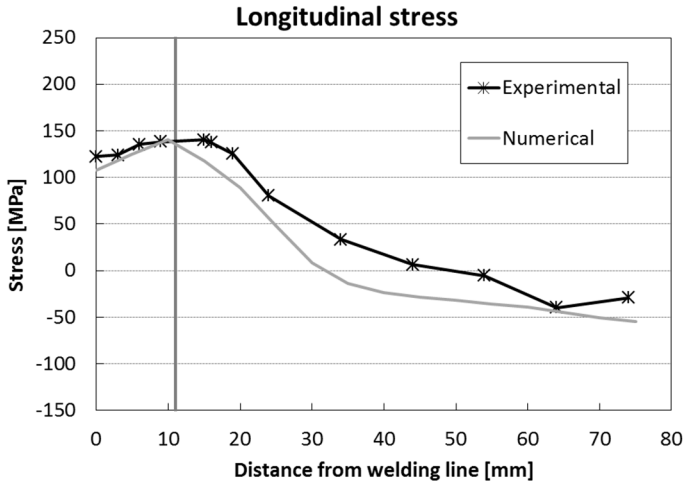

Figure 6.7 Numerical vs experimental comparison of longitudinal stress

In Figure 6.8 the stress in the transverse direction has been reported and compared with numerical results. The trend of stress is roughly constant with a value of 60 MPa along all the transverse direction of the plate. Moreover, according to the observations reported by Sutton et al. [62], the transverse stress has lower values than longitudinal stress and it is about 70% of the this one.

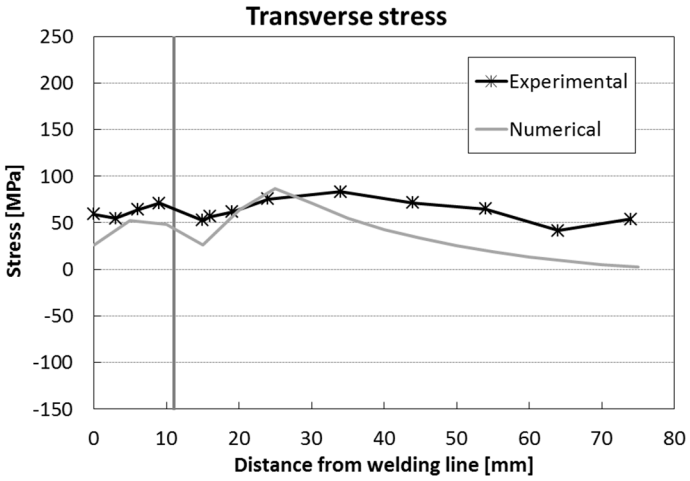

Figure 6.8 Numerical vs experimental comparison of transverse stress

Although some little discrepancies exist between the simulated numerical values and the measured ones, the distribution of the residual stress both longitudinal and transverse show a good

agreement with the experimental results. However, away from the welding line there is the maximum difference between numerical and experimental data for both longitudinal and transverse stresses. This could be explained considering that the initial residual stress in the numerical model is difficult to take into account. Moreover, away from the welding line, the influence of the welding process is minimal and the residual stresses trend should tend to the pre-weld value.

The numerical model has been solved changing the clamp positions as indicated in Figure 6.1. In Figure 6.9 and Figure 6.10 the comparison of the residual stress profile between the actual clamp model and the two different simulated clamp setups have been reported. The longitudinal stress (Figure 6.9) shows a reduction of the residual stress value in the welded zone and in the zone close to the bead. Indeed, on the welding line the longitudinal stress goes from 108 MPa of the actual setup to 83 MPa of 10 mm and 72 MPa of 20 mm setups. This reduction is more consistent from 4 mm to 10 mm than from 10 mm to 20 mm setups. Instead, away from the bead, there is the opposite behaviour and 20 mm configuration shows an increase of residual stress of 30 MPa than the experimental setup.

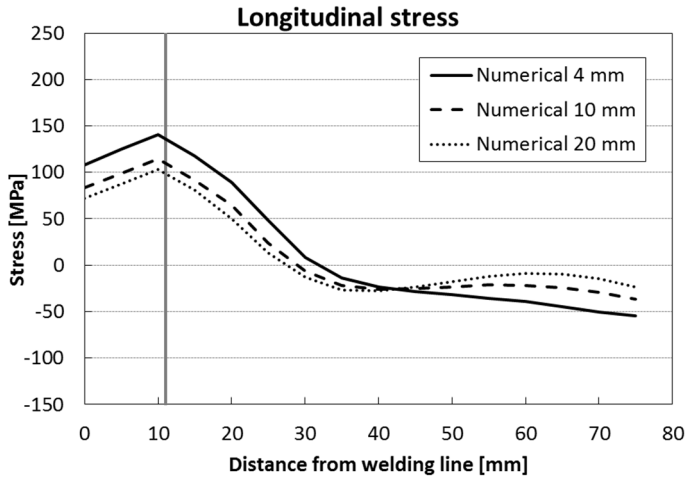

Figure 6.9 Numerical simulation of the clamp position on the longitudinal stress

Figure 6.10 shows the trend of the transverse stress. There is a small reduction in the residual stress between the actual clamps setup and the simulated 10 mm and 20 mm. Moreover, the 10 mm and 20 mm setups do not show any substantial difference in the residual stress values between them. The maximum residual stress difference between experimental configuration and 20 mm simulated setup is 10.8 MPa.

Finally, based on numerical results, the 20 mm clamp setup should reduce the residual stress in the welded zone and produce a beneficial effect on the welded specimen.

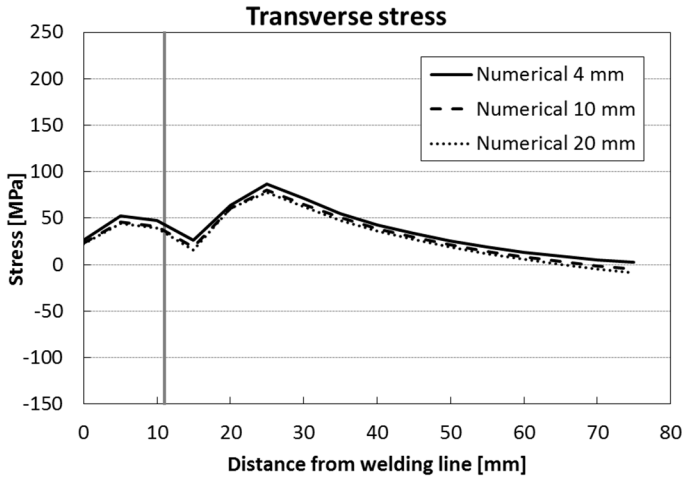

Figure 6.10 Numerical simulation of the clamp position on the transverse stress

6.2. Numerical prediction of residual stresses in LAFSW

In this section, the implementation of a numerical model that can predict the residual stresses distributions in LAFSW will be explained.

6.2.1. Materials and methods

The LFSW process has been carried out joining, in butt-weld configuration, two 200 mm x 100 mm x 6 mm AA5754-H111. The material chemical composition, thermo-physical properties, and mechanical characteristics at room temperature are the same of the properties reported in the previous chapters. The process parameters, tool scheme, experimental setup, etc. are the same of those reported in section 4.2.2.

The residual stresses measurements have been carried out employing the Xstress 3000 G3R Stresstech X-ray diffractometer with the same setup explained in section 5.2.1.

As mentioned in section 4.2.2, the temperature measurement but also the residual stresses analysis and then numerical simulation have been carried out for the retreating side of the FSW welded plate, because the configuration of the FSW machine prevents access to both sides.

6.2.2. Numerical model description

The mechanical part of the LAFSW model is based on the thermal model described in section 4.2.2. To the previously described thermal model, it has been added the mechanical part which employ the thermal data as an input to the mechanical model. However, as explained in the previous chapter, the LAFSW has been validated on a bead on plate configuration in order to capture also the temperature in front of the tool. To validate the residual stress model, it is necessary to carry out the measurements on real butt-weld configuration. In order to solve this problem, once the numerical model has been validated (see section 4.2.3), it has been extended on the actual welding configuration to simulate the temperature during the joining of two 200 mm x 100 mm plates. The obtained temperature field has been used as thermal input to the mechanical

model to predict the residual stresses and strains. Finally, the numerical computed stress values have been compared to the X-Ray residual stress experimental measured.

In order to pass the temperature data from the thermal model to the mechanical part as an input, the SOLID90 elements have been substituted with SOLID186 elements, keeping the same load step size. A multi-linear isotropic hardening has been adopted to describe the stress-strain behaviour of the material and temperature dependent mechanical properties of the material have been used (Table 6.1).

The mechanical effect due to the compression force applied by the tool has been taken into account introducing a uniform axial pressure distributed on tool area. The mechanical constrains have been set according to experimental set up (Figure 6.11). For the left and right clamp an area of 20×40 mm has been constrained, instead, for the below clamp a centred 3×100 mm area has been constrained. These constraints block the movements in all direction. Moreover, the left side of the plate has been blocked in the x-axis direction. Finally, the bottom of the plate has been constrained in z-direction. Once that the welding simulation is concluded, the constraints are gradually released and the residual stresses due to LFSW process have been evaluated.

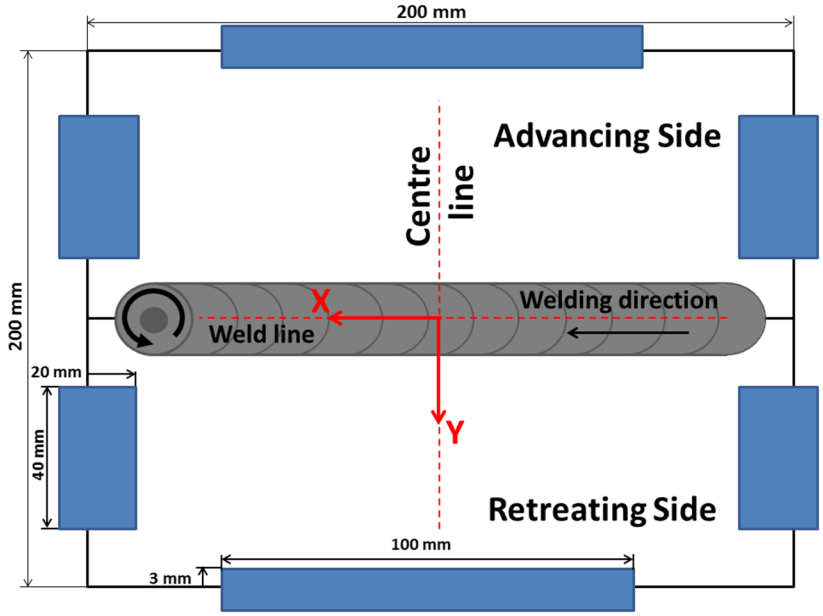

Figure 6.11 Specimen and clamping system scheme in LAFSW

6.2.3. Results and discussion

In order to validate the mechanical part of the model, X-Ray diffraction stress measures have been carried out. Both the superficial longitudinal stress (welding direction) and transverse stress (transverse to welding direction) on the centre line has been measured and compared with the numerical model prediction. In Figure 6.12, the numerical versus experimental longitudinal stress trend has been reported for the retreating side. The maximum stress value in the LFSW welds is

located on the edge of the bead as has been showed in the Figure 6.12 by a vertical grey line at a distance of 10.75 mm from the joining line.

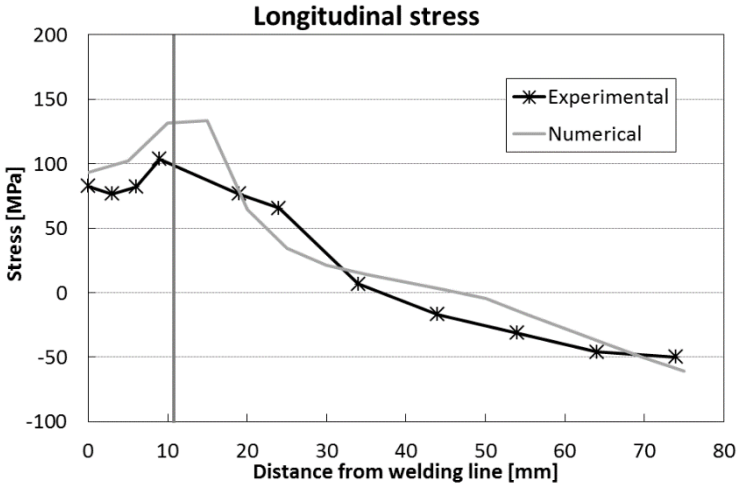

Figure 6.12 Numerical vs experimental comparison of longitudinal stress

In Figure 6.13 the stress in the transverse direction, in the retreating side, has been reported. The trend of the stress is roughly constant along all the transverse direction of the plate. Only in the welded zone there is a small increment probably due to the laser presence. In general, the distribution of the residual stress, in both longitudinal and transverse direction, shows a good agreement with the experimental results.

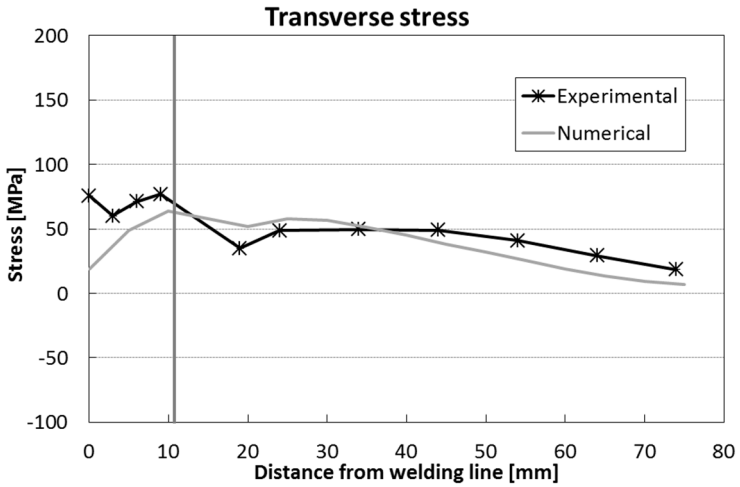

Figure 6.13 Numerical vs experimental comparison of transverse stress

6.3. Summary and conclusions

In this chapter, the numerical model to predict residual stresses in FSW and LAFSW and a study on the influence of the clamps configuration on residual stresses have been presented.

A three-dimensional thermo-mechanical model has been developed in order to predict residual stresses in FSW and to have a better knowledge of the influence of the clamp position on residual stresses trends. This model includes the mechanical action of the shoulder and the thermo-mechanical characteristic of AA5754 at different temperatures. Thermographic analysis of FSW

weld process and residual stress measurement by X-Ray diffraction have been carried out to validate the model thermally and mechanically. The model shows good capacity to predict the actual temperature and the residual stresses. As next step, the numerical model has been solved increasing the constrained area of the FSW plate in order to understand the influence of the constraints. Following this change the longitudinal stress shows a reduction of its value in the bead and in the zone close to the bead. Instead, away from the welding line there is an opposite behaviour that increases the longitudinal residual stress bringing it closer to zero value. Moreover, the transverse residual stress, changing the clamped area on the plate, does not show a significant reduction of the residual stress.

Finally, a three-dimensional thermo-mechanical model of LAFSW has been modelled. The aim of the FE simulation is to predict the temperature and residual stress developed during the weld. As the FSW model, also this one includes the mechanical action of the shoulder and the thermo-mechanical characteristic of AA5754 at different temperatures. The validation of the thermal part of the model has been done on a bead on plate configuration as showed in section 4.2.3. Once the thermal part has been validated, the model has been extended to weld two 200 mm x 100 mm plates in view to simulate the actual welding setup. The obtained temperature field has been used as thermal input to the mechanical part in order to predict the residual stresses. These values have been compared to the X-Ray residual stress experimental measurements. The longitudinal residual stress measurements confirm, as pointed out in the chapter 5, that the maximum value in the LAFSW welds is located on the edge of the bead. Moreover, the transverse stress has lower values than longitudinal stress confirming that this type of residual stress is a less critical issue also in this combined joining process.

7. Fused Deposition Modelling: background and state of the art

The name rapid prototyping processes (RP) groups several technologies that have as main objective to speed up the process of product development by creating prototypes in a very small period of time [65]. The first commercial implementation of RP began through the Stereolithography apparatus (SLA) technique in 1986. In the following years, many new technologies emerge for RP, such as, Fused Deposition Modelling (FDM), Three-Dimensional Printing (3DP), Selective Laser Sintering (SLS), Selective Laser Melting (SLM), PolyJET, Multi Jet Modelling, etc.

Initially the RP were mainly used to produce prototype parts for design verification, kinematic functionality testing, and fabrication of models for visualization. But nowadays, the RP technologies have also a significant role in the rapid production of finished parts such as, polymer or wax prototypes used as sacrificial patterns to produce moulds for casting or direct building of the final part using SLS, SLM or FDM [66]. Consequently, these techniques change their functions from RP to Rapid Manufacturing (RM) and can be involved in production of custom or replacement parts in single piece or small series production. The common benefit in all these cases is being able to produce parts direct from digital data, eliminate the need for complex tooling, and enhance the speed and cost, compared to traditional approaches like injection moulding.

7.1. Process

The Fused deposition modelling (FDM) is an additive rapid prototyping process invented and patented by S. Scott Crump co-founder of Stratasys Inc. in 1989. In this process, as in other additive techniques [67], the model is built as a layer-by-layer deposition of a feedstock material. The conceptual design, which is created on a CAD software, cannot be inputted directly into the FDM system. After the modelling, the CAD file has to be exported as .STL file and then inputted in a slicer. This software can be a proprietary or open source software (e.g. Slic3r, Skeinforge, Cura, etc.) and it has the function to slice the part into horizontal layers and define the tool path. After this software procedure, the output of the slicer is a .gcode file that can be inputted in the 3D printer and start the printing phase. Initially, the raw material is in the form of filament that is partially melted, extruded and deposited by a heated nozzle onto the previously built model [68]. After the deposition, the material cools, solidifies and sticks with the surrounding material (Figure 7.1). Once the entire layer has been deposited, the nozzle moves upward along the z-axis for the deposition of the next layer. If the model requires structural support for any overhanging

geometry, a second nozzle simultaneously extrudes layers of a water soluble support material in the same manner [69].

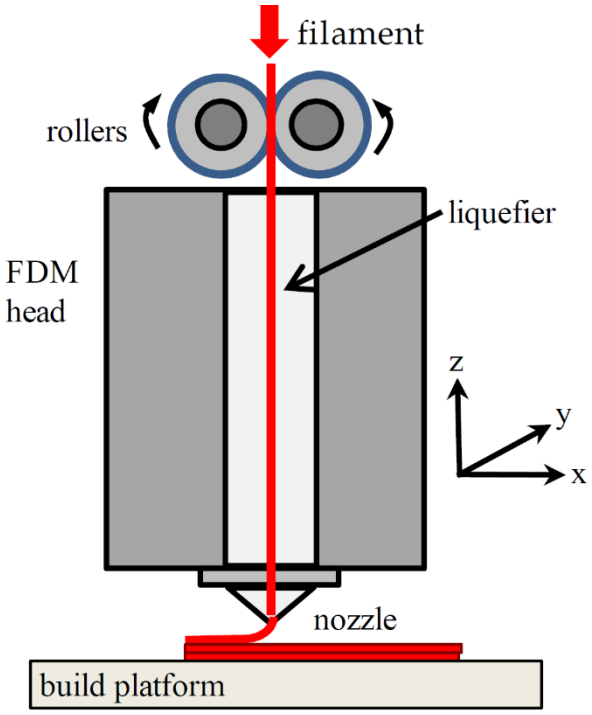

Figure 7.1 Scheme of the FDM process [69]

In FDM, the plastic filament is extruded as closely spaced beads within each layer and then, the layers are stacked one over the other to build the 3D part. The beads bonding is driven by the thermal energy of the semi-molten material that is deposited [70]. After the deposition, the polymer establishes an interfacial molecular contact by wetting and starts the molecular motions. As can be observed in Figure 7.2, the resulting parts are an orthotropic structure of partially bonded beads and voids [71].

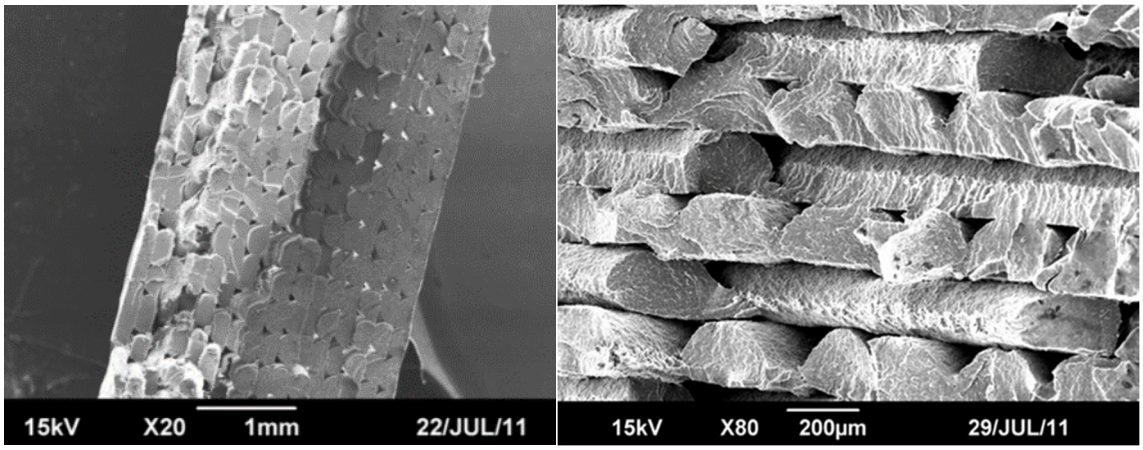

Figure 7.2 FDM fracture section through a SEM image [69]

Thus, the mechanical properties of FDM parts depends from the mesostructures that is influenced by the manufacturing parameters, such as, width of the beads, layer thickness, deposition

orientation, speed and time of deposition. The presence of air gaps and the quantity of air voids between the rasters additionally influences the strength of FDM parts. Consequently, as in composite materials, also in FDM parts should be established the most appropriate raster orientation based on the expected in-service loading before the printing phase.

7.2. Materials

Traditionally, the FDM 3D printers have been able to build parts only in thermoplastic materials such as polylactic acid (PLA) and acrylonitrile-butadiene-styrene (ABS). The PLA offers better thermo-mechanical characteristics than ABS having a stronger mechanical resistance and a lower coefficient of thermal expansion. The last characteristic improves the printability of PLA because reduces the effects of warping during the printing phase. Moreover, it shows less health risks than ABS when printing in small and improperly ventilated spaces [72]. Nowadays, many others materials have been used or developed, e.g., bio-resorbable polymer (PCL) [73], short fibre composites [74], ceramics [75, 76], metal [77, 78] and metal/polymers mixture materials [79].

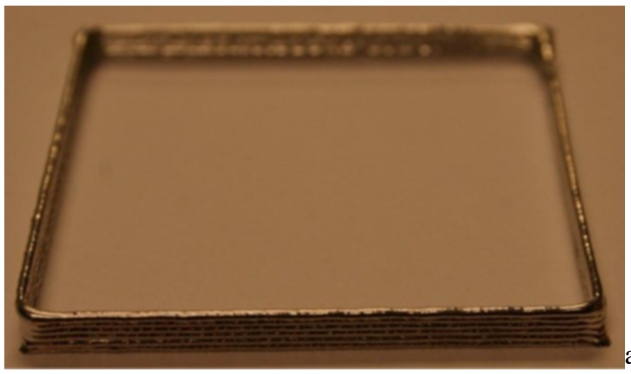
a)

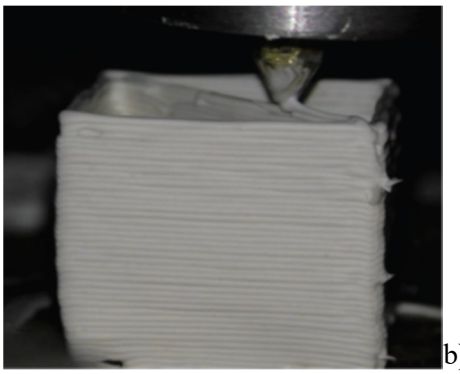
b)

Figure 7.3 Example of FDM metal (a) [78] and ceramic (b) [76] prints

The procedure to print by fused deposition of ceramics requires a further step after the printing phase. Indeed, the creation of FDM feedstock filaments in ceramic material requires using ceramic powders mixed with organic binder system. The properties of the mixed feedstock filament meet the mechanical characteristics required for successful FDM processing. However, the fabricated green parts need to undergo further processing to remove the organic binder and are subjected to sintering to achieve densification [80].

7.3. Process parameters

As in every manufacturing processes, also in FDM the process parameters control the part quality and the production time. Consequently, the key success of the FDM process depends upon the proper selection of process parameters which ensure quality of the products, reduce production time and cost, improve dimensional precision and avoid wastes and large amount of scraps. However, FDM is a complex process in which there are great difficulties in determining the optimal parameters due to the presence of a large number of conflicting parameters that

sometimes depend on the specific 3D printer. For example, in Figure 7.4 has been reported the main process variables and factors that need to be studied and optimized in FDM process in order to obtain good quality objects [81].

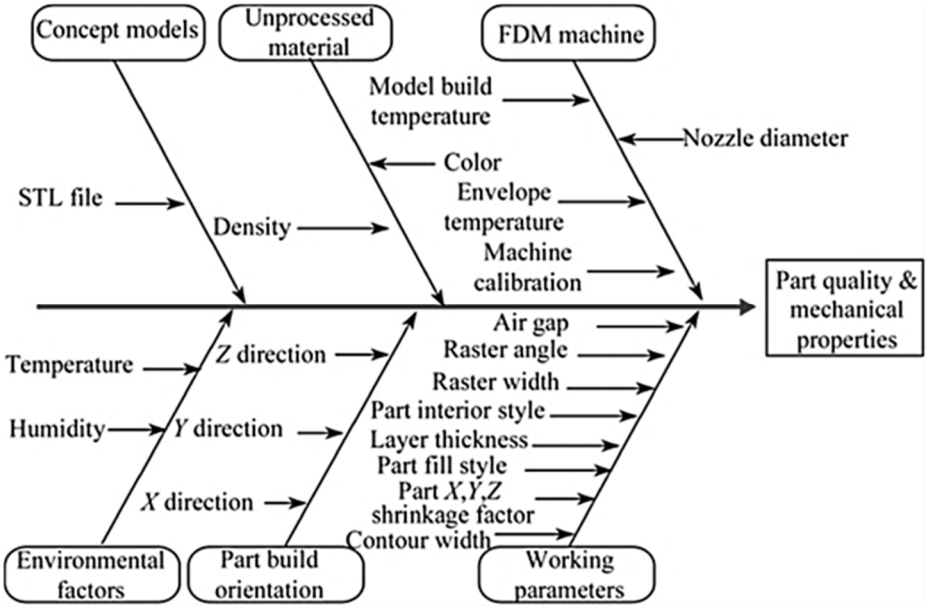

Figure 7.4 Main FDM process parameters and factors that influence the quality of the objects [81]

In Figure 7.5, Figure 7.6 and Figure 7.8 the meanings of some FDM process parameters have been reported. In order to explain in a better way these figures, the process parameters are also described as follows [81]:

1) The build orientation refers to the way in which the part is oriented inside the build platform with respect to X, Y, Z axes, as shown in Figure 7.5.

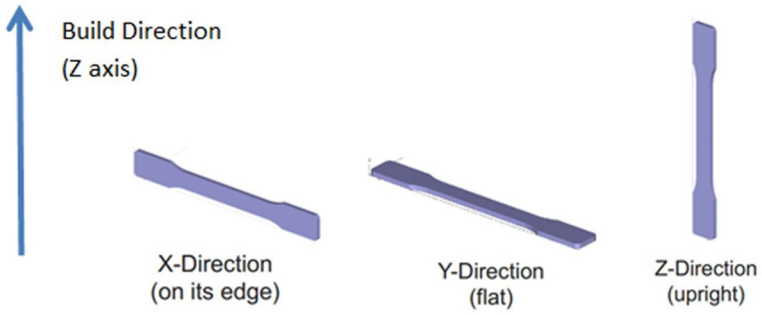

Figure 7.5 Build orientation on a FDM build platform

2) The layer thickness is the thickness of a layer deposited by the nozzle, as shown in Figure 7.6. The value of layer thickness depends on the material and nozzle diameter. Decreasing this value the surface quality improves (Figure 7.7) but the printing time increases as a consequence.

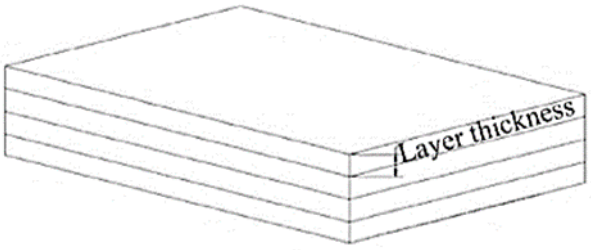

Figure 7.6 Layer thickness [81]

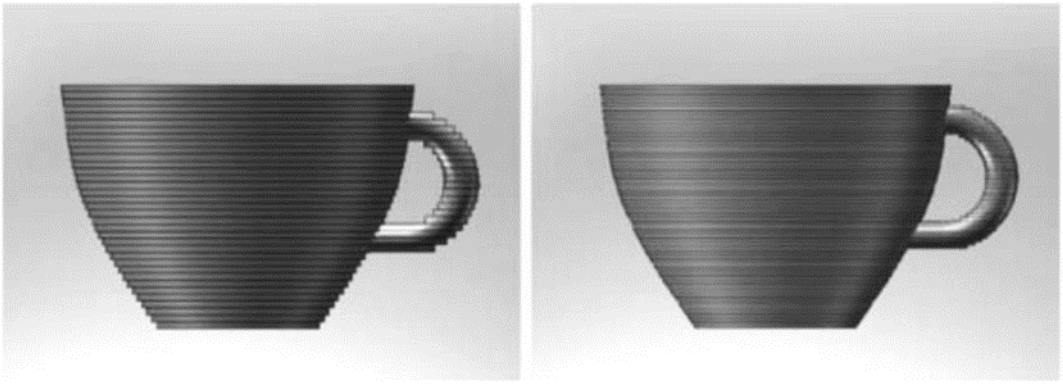

Figure 7.7 Effect of building using different layer thicknesses [82]

3) Air gap refers to the gap between adjacent raster tool paths on the same layer, as shown in Figure 7.8. Sometime, in order to eliminate the internal void, this parameter can be a negative value. Consequently, this setup produces an overlap between two adjacent rasters.
4) The angle of the raster pattern respect to the X axis is the raster angle. This parameter is very important in FDM because influence the mechanical behavior of the parts. The typical allowed raster angles are from 0° to 90°.
5) The width of the material bead employed for the rasters is called the raster width. The value of raster width varies based on nozzle diameter and can be larger than the nozzle diameter itself. Usually, a larger value can be employed in th e first layer to increase the adhesion of this layer on the platform. This in order to reduce the warping problem.
6) Contour width refers to the width of the contour tool path that surrounds the part curves.
7) The number of contours to build around all outer part curves is shown in Figure 7.8. Additional contours, usually, improve mechanical resistance of the part.
8) Contour to contour air gap refers to the gap between contours when the printer carries out multiple contours.
9) Perimeter to raster air gap refers to gap between the inner most contour and the edge of the raster fill inside of the contour.

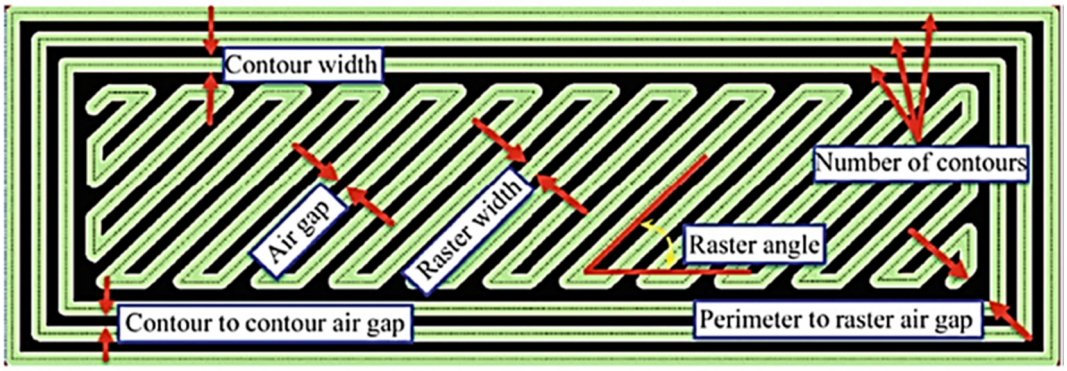

Figure 7.8 FDM tool path parameters [81]

7.4. Advantages, applications and issues

The principle of the FDM technology offers great potential because, without any need for machining, allows the fabrication of complex 3D parts directly from a computerized solid model. With FDM, but this is in common with Additive Manufacturing, it is possible to build a part with almost any shape, both internal and external, due to the layer by layer approach. This is a huge advantage compared to the two conventional manufacturing techniques, i.e. machining and injection moulding. In machining, a limiting factor that determines shape complexity is tool accessibility. On the other hand, in injection moulding, shape complexity is limited by the need to separate the parts from the moulds [82]. Moreover, with the layer by layer approach, internal voids or particular shape can be made in an easy way. Thus, different kinds of components can be inserted into fabricated parts during building. This makes post-fabrication assembly unnecessary. For instance, small metal parts, electric motors, printed circuit boards, and sensors can be embedded in parts.

Compared to other 3D printing techniques, this method allows to employ various materials, including waxes, ceramics, thermoplastic resins, and metals in specific forms to be used to print three-dimensional shapes. For industrial company, FDM allows to evaluate and optimize the prototype design in early stages of product development reducing the costs and shorten the development time. Moreover, FDM prototypes can be tested in real world environment and can be employed also as final product in single parts or low volume productions.

Many companies have already employed FDM in their productions. For example, BMW employs the FDM technique to test and enhance the ergonomics of some parts of its products using the freedom of design and manufacturing possibilities to create configurations that improve handling. National Aeronautics and Space Administration (NASA) tests some parts of the next generation rover for space exploration. 3D-printed parts on NASA's rover include flame-retardant vents and housings, camera mounts, large pod doors, a large part that functions as a front bumper, and many custom fixtures (Figure 7.9).

Figure 7.9 More than 70 parts of the NASA rover has been made using FDM

Lamborghini uses the FDM to make functional prototypes for the transmission of its new cars. Moreover, it produced a 1/6 scale model of the body and chassis of the Lamborghini Aventador (Figure 7.10).

Figure 7.10 The 1/6 scale FDM prototype of Lamborghini Aventador

Further examples of FDM applications can be found especially in biomedical applications, where the development of biopolymers has been strongly expanded.

On the other hand, there are also some shortcomings associated with FDM technique. The speed of an FDM system depends from the feed rate and the plotting speed, thus, cannot be too much high. The feed rate is linked to the ability of the liquefier to melt the material and feed it through the nozzle. However, in order to increase the material flow rate, the liquefier has to been able to melt more material and most likely it would result in an increase in mass. Consequently, this increase of mass would make it more difficult to move faster [82].

Another important issue is the anisotropic properties of a FDM part. Different layering strategies result in different strengths. Typically, using the appropriate stacking sequence, the mechanical properties are quasi-isotropic in the x–y plane of the parts, but if the raster fill pattern is set to preferentially deposit along a particular direction, then the properties in the x–y plane will also be anisotropic. However, in every case, the strength in the z-direction is less than the strength in the x–y plane. Thus, the appropriate stacking sequence and print orientation should be selected in order to align the major stress axes with the x–y plane rather than in the z-direction [82].

The part defects can be a great issue in FDM. These can be classified into two categories: surface and internal defects. Usually, the surface defects are related to the nature of layer by layer manufacturing procedure. Indeed, the external surfaces are affected by stair-step effects due to the deposition of flat layers one on the other. Clearly, this become particularly evident on curved surface and when using thicker layers. In order to partially overcome this problem, thinner layers can be employed but, consequently, the printing time increases (Figure 7.11).

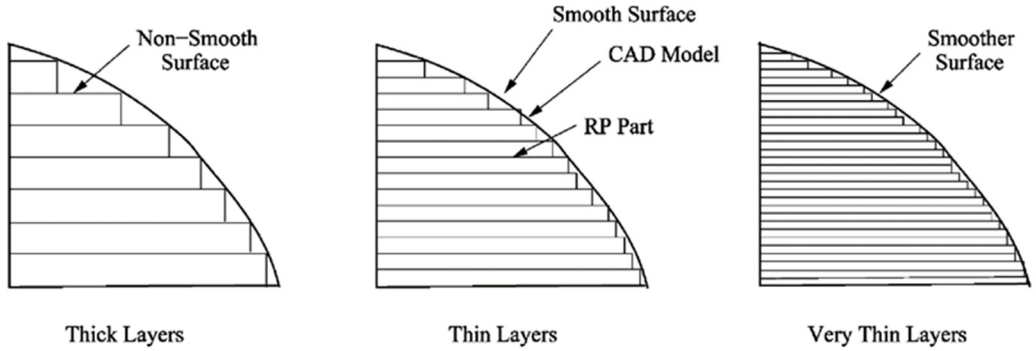

Figure 7.11 Effect of layer thickness on surface finish [83]

Internal defects are usually due to the limitations of FDM systems and slicer processing strategies. For example, inter-bead or core voids can be successfully eliminated by several techniques that are now commonly implemented in slicer software. A solution for the inter-bead void is the use of a negative gap between adjacent roads. The core voids can be avoided selecting the appropriate build and infill strategies.

Though external and internal voids are an issue in FDM technique, however, the main problem is the distortion of the part during the printing phase. Indeed, the FDM part cools down layer by layer during the deposition and, consequently, there is thermal variation and different cooling rates from one layer to the other. This produces internal stresses between layers [84], uneven shrinkage, de-layering problems, warping and the relatively associated problems especially with larger parts (Figure 7.12). Often the warpage of the part can prevent the finalization of the objects due to unsticking problems from the bed.

Figure 7.12 Warpage of the FDM part

In order to reduce the distortion problems, a heated bed on low cost machines or a heated chamber on high-end 3D printer can be employed. In addition to the heated bed to solve the warping problem, usually, the part is glued on a bed. However, this can solve the distortion problem but it does not resolve or it can also worsen the residual stress issue in FDM part.

8. Mechanical properties of FDM parts

In recent years, the FDM evolved from rapid prototyping technique towards a rapid manufacturing method, changing the main purpose in producing finished components ready for use [66]. Indeed, this technique is particularly promising for the fabrication of a single piece or, in general, low volume products such as replacement parts for not widespread system. This trend highlights the need for a deep understanding of the mechanical properties and the behaviour of parts produced by FDM. A thorough understanding of the mechanical properties is complex, because this is influenced by many production parameters whose combination is often difficult to understand. A FDM part can be considered as laminated orthotropic structure with vertically stacked layers of bonded beads [71]. As consequence, not only the feedstock material controls the mechanical properties of FDM parts, but also, the stack sequences whereby the layers are overlapped.

Several papers deal with the anisotropic characteristics of FDM parts in recent years. Ahn et al. [71] carried out several experiments to determine the effects of air gap, bead width, raster orientation and ABS colour on tensile and compressive strengths. They determine that air gap and raster orientation have an important effect on the tensile strength, on the other hand, the other parameters have negligible effects. Moreover, the factors that they have studied do not affect the compressive strength in a noticeable way. Lee et al. [85] concluded that raster angle, air gap and layer thickness influence the elastic performance of flexible ABS objects. Also Anitha et al. [86] studied the effect of the layer thickness showing that the performance increases when the thickness decreases. Sood et al. [87], using the response surface methodology, analyse the functional relationship between specimens strength and several factors, e.g., build orientation, layer thickness, raster angle and air gap. Their results show that these factors influence the bonding and distortion within the parts. Lee et al. [88] carried out several experiments on cylindrical layered parts made from three different rapid prototyping processes, i.e., FDM, 3D printer and nano-composite deposition (NCDS). The aim of their work was to study the effect of the build direction on the compressive strength. The results show that compressive strength is greater for axial FDM specimens than for the transverse ones. This empirical approach allows to understand easily the relation between the FDM process parameters and the mechanical properties of the material, but it needs expensive experimental campaigns and, generally, it is difficult to extrapolate the behaviour of the material in other conditions. On the contrary, few papers in literature deal with the development of predictive models to determine the mechanical properties of FDM parts. Croccolo et al. [89] develop an analytical model taking into account some of the 3D printer parameters to determine the final mechanical characteristics of the specimens. However, this model needs to introduce adhesive force between the beads that could be difficult

to estimate. Contrariwise, the use of models widely known and implemented, such as the classical laminate theory, already employed for composite materials, could be a real advantage in terms of usability.

In this chapter, some preliminary studies on the mechanical behaviour of FDM parts will be done. It is divided into two main section. In the first, the Classical Laminate Theory (CLT) will be employed to describe the FDM parts behaviour, in the second, a study on tensile-impact of FDM specimens will be done. The final aim is to prove that FDM parts show an orthotropic behaviour on both static and dynamic loads. These studies will be useful in order to have a better knowledge of the FDM parts and establish the appropriate behaviour of the material to employ in the residual stress calculation that will be done in the next chapter.

8.1. Orthotropic mechanical properties of FDM parts

The aim of this section is to describe the mechanical behaviour of FDM parts by the classical laminate theory (CLT). In order to reach this objective, the values of the elastic modulus in the longitudinal and transverse directions to the fibre (E_1, E_2), the Poisson's modulus (ν_{12}) and the shear modulus (G_{12}) will be experimentally measured. The determination of E_1 and E_2 will be carried out by single layer tests conducted on specimens with 0° and 90° raster angles. The Poisson's modulus will be determined measuring, on five layers 0° specimens, the longitudinal and transverse deformation by strain gauges. The shear modulus, G_{12}, will be determined according to the ASTM D3518. In this study, two different material ABS and PLA will be employed to prove the validity of CLT on several materials.

8.1.1. Classical laminate theory

The classical laminate theory allows to calculate the elastic behaviour of a multi-layer orthotropic material using the constants that describe the mechanical behaviour of the single layer E_1, E_2, ν_{12}, G_{12} and h_c. E_1 and E_2 are the elastic modulus in the longitudinal and transverse directions to the fibre, ν_{12} is the Poisson's ratio, G_{12} is the shear modulus, and h_c is the layer thickness. The reduced stiffness tensor $\mathbf{Q}_k$ can be calculated, for each layer k and in the layer system reference $\{x_1, x_2, x_3\}$ (Figure 8.1), as:

$$\boldsymbol{Q}_k = \begin{bmatrix} Q_{11} & Q_{12} & 0 \\ Q_{12} & Q_{22} & 0 \\ 0 & 0 & Q_{66} \end{bmatrix} \tag{8.1}$$

The terms in the matrix are:

$$Q_{11} = \frac{E_1}{1 - \upsilon_{12}\upsilon_{21}},\ Q_{12} = \frac{\upsilon_{21}E_1}{1 - \upsilon_{12}\upsilon_{21}},\ Q_{22} = \frac{E_2}{1 - \upsilon_{12}\upsilon_{21}},\quad Q_{66} = G_{12} \tag{8.2}$$

with

$$v_{21} = v_{12}\frac{E_2}{E_1} \tag{8.3}$$

The relations between the applied forces **N** and moments **M** and the resulting mid-plane strains $\boldsymbol{\varepsilon}^0$ and curvatures $\boldsymbol{\chi}$ can be summarized as a single matrix equation:

$$\begin{Bmatrix} \boldsymbol{N} \\ \boldsymbol{M} \end{Bmatrix} = \begin{bmatrix} \boldsymbol{A} & \boldsymbol{B} \\ \boldsymbol{B} & \boldsymbol{D} \end{bmatrix} \begin{Bmatrix} \boldsymbol{\varepsilon}^0 \\ \boldsymbol{\chi} \end{Bmatrix} \tag{8.4}$$

where the tensors **A**, **B** and **D**, when thickness h_c of the layers is constant, are:

$$\begin{aligned} \boldsymbol{A} &= \frac{h}{n}\sum_{k=1}^{n} \boldsymbol{Q}_k(\delta_k) \\ \boldsymbol{B} &= \sum_{k=1}^{n} \frac{1}{2}\frac{h^2}{n^2} b_k \boldsymbol{Q}_k(\delta_k) \\ \boldsymbol{D} &= \sum_{k=1}^{n} \frac{1}{12}\frac{h^3}{n^3} d_k \boldsymbol{Q}_k(\delta_k) \end{aligned} \tag{8.5}$$

In equation 8.5, k has been numbered from the bottom of the laminate, n is the total number of layers, h is the laminate thickness while b_k and d_k are:

$$b_k = 2k - n - 1 \tag{8.6}$$

$$d_k = 12k(k - n - 1) + 4 + 3n(n + 2) \tag{8.7}$$

In equation 8.5 $\boldsymbol{Q}_k(\delta_k)$ is the reduced stiffness tensor of the layer k in the laminate reference {x, y, z}. As indicated in Figure 8.1, δ_k is the angle between x-axis of the laminate reference and the x_1-axis of the layer k.

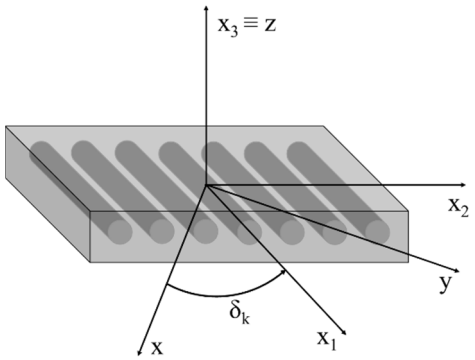

Figure 8.1 Laminate {x, y, z} and layer {x_1, x_2, x_3} systems reference

The calculation of the stress in each layer requires the calculation of the deformations and, thus, it is necessary to invert the laminate equation 7.4:

$$\begin{Bmatrix} \boldsymbol{\varepsilon}^0 \\ \boldsymbol{\chi} \end{Bmatrix} = \begin{bmatrix} \boldsymbol{A} & \boldsymbol{B} \\ \boldsymbol{B} & \boldsymbol{D} \end{bmatrix}^{-1} \begin{Bmatrix} \boldsymbol{N} \\ \boldsymbol{M} \end{Bmatrix} \tag{8.8}$$

Because this inversion could be quite complicate, another way to tackle the problem is to reverse one by one the three tensors that appear in equation 8.8, A, B and D. Thus, it is possible to rewrite equation 8.8 in the form:

$$\begin{Bmatrix} \boldsymbol{\varepsilon}^0 \\ \boldsymbol{\chi} \end{Bmatrix} = \begin{bmatrix} \boldsymbol{a} & \boldsymbol{b} \\ \boldsymbol{b}^T & \boldsymbol{d} \end{bmatrix}^{-1} \begin{Bmatrix} \boldsymbol{N} \\ \boldsymbol{M} \end{Bmatrix} \tag{8.9}$$

with

$$\begin{aligned} \boldsymbol{a} &= (\boldsymbol{A} - \boldsymbol{B}\boldsymbol{D}^{-1}\boldsymbol{B})^{-1} \\ \boldsymbol{d} &= (\boldsymbol{D} - \boldsymbol{B}\boldsymbol{A}^{-1}\boldsymbol{B})^{-1} \\ \boldsymbol{b} &= -\boldsymbol{a}\boldsymbol{B}\boldsymbol{D}^{-1} = -(\boldsymbol{A} - \boldsymbol{B}\boldsymbol{D}^{-1}\boldsymbol{B})^{-1}\boldsymbol{B}\boldsymbol{D}^{-1} \end{aligned} \tag{8.10}$$

Finally, in order to obtain the laminate properties, it can be defined:

$$\boldsymbol{a}^* = h\boldsymbol{a} \tag{8.11}$$

Thus, the laminate Young's Modulus in the x direction is:

$$E_x = \frac{1}{a_{11}^*} \tag{8.12}$$

This value of the laminate Young's modulus obtained from CLT will be compared with the Young's modulus measured from experimental data.

8.1.2. Materials and methods

As requested by CLT, the values of the elastic modulus in the longitudinal and transverse directions to the fibre (E_1, E_2), the shear modulus (G_{12}), and the Poisson's modulus (ν_{12}) have been experimentally determined. Finally, the comparison between the CLT and the experimental results, conducted on ABS and PLA, has been carried out on symmetric and balanced specimens. A RepRap Prusa i3 equipped with a marlin firmware and a nozzle of 0.4 diameter has been employed for the production of the specimens. Some parameters, such as the layer thickness or the number of contour lines, have been kept constant for every specimen. These values have been reported in Table 8.1. The bed temperature for ABS has been set to 90 °C and to 55 °C for PLA. Moreover, the nozzle temperature is 225 °C for ABS and 200 °C for PLA. Finally, the specimens have been fabricated with the minimum dimension of the part perpendicular to the build platform.

Table 8.1 Fixed printer parameters

Parameter	Value
Air gap [mm]	0
Layer thickness [mm]	0.35
Bead width [mm]	0.62
Number of contour lines	2

The angle, relative to the load direction, with which the beads are deposited, is called the raster angle. For example, a layer with a 0° raster angle has the deposited beads parallel to the load direction. The samples have been shaped as required by the standard ASTM D638-10 with reference to the geometry of the first typology (Figure 8.2). The solid model, created using a 3D CAD, has been sliced using the open source software Slic3r.

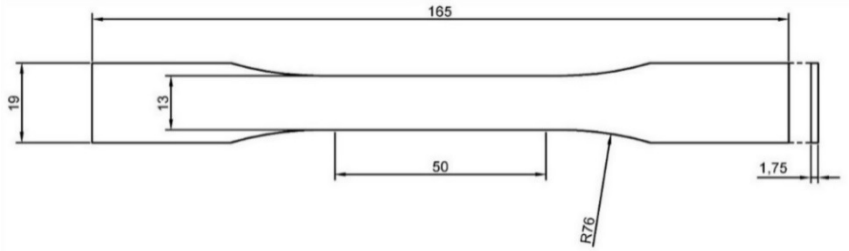

Figure 8.2 ASTM D638 Specimen shape with dimensions in mm

Five specimens for each direction and material have been made for the experimental measure of the elastic modulus of the single layer in the longitudinal and transverse directions to the fibre (E_1, E_2). The Figure 8.3 shows a detail of single layer ABS specimen (Figure 8.3a) with a raster angle of 90° and a detail of single layers PLA specimen (Figure 8.3b) with a raster angle of 0°. In addition, 45° specimens have been made in order to show in a better way the orthotropic mechanical behaviour of FDM specimens (Figure 8.3c). The tensile tests have been carried out on an Instron 3343 equipped with a 1000 N load cell and ISO 9513 class 0.5 extensometer. A crosshead speed of 5 mm/min has been selected according with ASTM D638-10.

The Poisson's modulus (ν_{12}) has been measured on five layers 0° specimens due to the difficulty to measure the transversal strain on single layer specimen. The longitudinal and transverse deformations have been measured using strain gauges and a HBM QuantumX 840 has been employed to acquire the data.

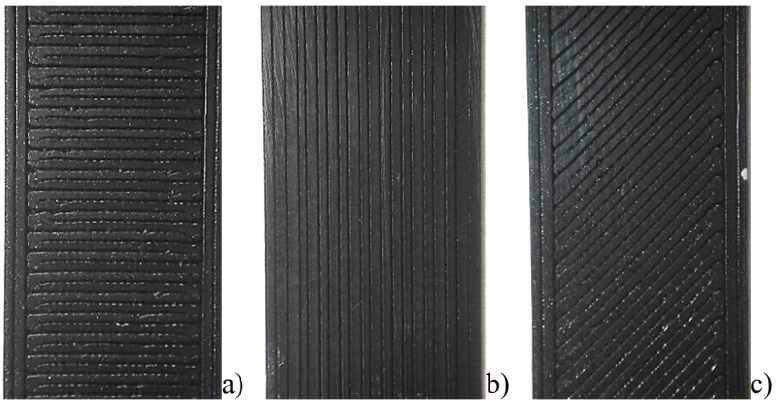

Figure 8.3 A detail of the single layer specimens: a) 90° orientation specimen; b) 0° orientation specimen; c) 45° orientation specimen.

The shear modulus (G_{12}) has been measured according with ASTM D3518-94. For each material, three flat rectangular specimens have been made with dimension 200 mm length, 25 mm width and 5.6 mm thick. These samples consist of 16 layers in a symmetric criss-cross configuration, i.e. the stack sequence is $[+45/-45]_{4s}$. The tests have been carried out on a MTS Alliance RT/30 instrumented with a 30 kN load cell. According with ASTM D3518-94 a crosshead speed of 2 mm/min has been used during the test.

In order to compare the CLT and the experimental results, five specimens for each material have been made with a symmetric and balanced stack sequence [+30/-30/0/-30/+30]. The ABS specimens have been tested on Instron 3343. However, because the PLA samples are stronger than the ABS ones and they would be broken at higher load than 1000 N, a MTS Alliance RT/30 with a 30 kN load cell has been used for the PLA tests. The stain measurements have been acquired using an MTS 634.25F-54 extensometer.

8.1.3. Results and discussion

The result data have been processed, following the recommendations of ASTM D638-10, for the determination of the Young's modulus E and the ultimate tensile strength UTS values. The Young's modulus E has been determined considering the linear part of the stress–strain curve and the slope has been estimated by a linear fit. The UTS has been calculated as a ratio between the maximum load reached during the test and the cross-sectional area. The mechanical properties for the two feedstock wire materials have been experimentally determined and reported in Table 8.2 and Table 8.3. The tests on the wire show that the PLA has a Young's modulus and UTS values that are about twice the values of ABS. However, even if PLA is stronger than ABS it is more brittle. Indeed, the deformation at fracture is 0.079 mm/mm for the PLA and 0.16 mm/mm for the ABS. Moreover, the most important disadvantages of PLA compared to ABS are the lower capacity to stand temperature higher that room temperature and the lower durability due to its biodegradability. A summary of the average results for the single layer tensile tests has been reported in Table 8.2 for ABS and Table 8.3 for PLA.

Table 8.2 ABS Single layer mechanical properties at different raster angle

Specimen	**Young's modulus** [GPa]	**Young's modulus Standard deviation** [GPa]	**UTS** [MPa]	**UTS Standard deviation** [MPa]
ABS Wire	1.81	0.180	32.11	0.303
ABS 0°	1.79	0.577	26.11	2.37
ABS 45°	1.38	0.106	11.97	3.12
ABS 90°	1.15	0.088	6.71	0.36

Table 8.3 PLA Single layer mechanical properties at different raster angle

Specimen	**Young's modulus** [GPa]	**Young's modulus Standard deviation** [GPa]	**UTS** [MPa]	**UTS Standard deviation** [MPa]
PLA Wire	3.38	0.054	55.26	0.76
PLA 0°	3.12	0.035	50.23	0.77
PLA 45°	2.86	0.018	40.68	0.75
PLA 90°	2.77	0.317	22.49	6.75

The Table 8.2 and Table 8.3 show that the wire, both for PLA and ABS, are stiffer and stronger than the 0° single layer samples. This is probably due to the extrusion process that influence, introducing some defects, the resulting specimens. Moreover, the single layer tests highlight the orthotropic behaviour of the FDM parts showing a reduction of the mechanical characteristics increasing the raster angle. The mean Young's modulus decreases between 0° and 90° of 35.72% for ABS and 11.12% for PLA. The mean UTS shows a reduction of 74.30% for ABS and of 55.22% for PLA. This trend suggests that ABS has a much more marked orthotropic behaviour than PLA. Probably, this is due to a better capacity of PLA to bond each bead to the other. The 45º specimens have an intermediate behaviour between the 0° and 90° mechanical properties. However, for both ABS and PLA, the 45° behaviour is nearer to 90° than 0°. Some representative stress-strain curves have been reported for the single layer specimens changing the raster angle in Figure 8.4 for ABS and Figure 8.5 for PLA.

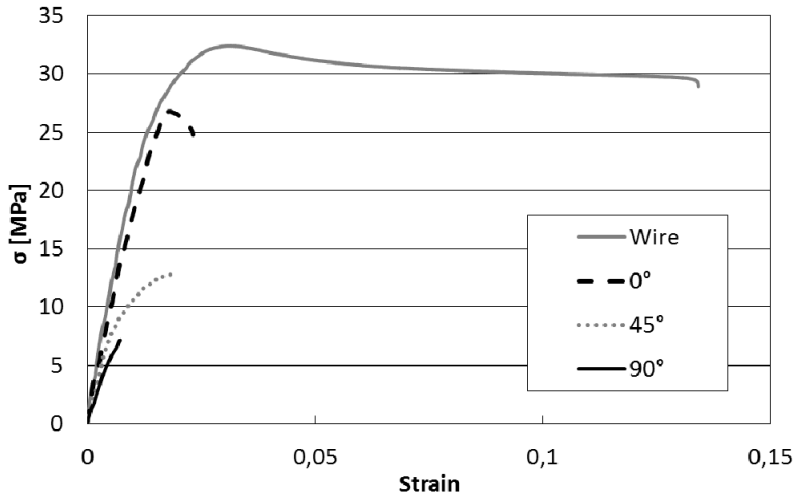

Figure 8.4 Representative tensile testing data for ABS at each raster orientation

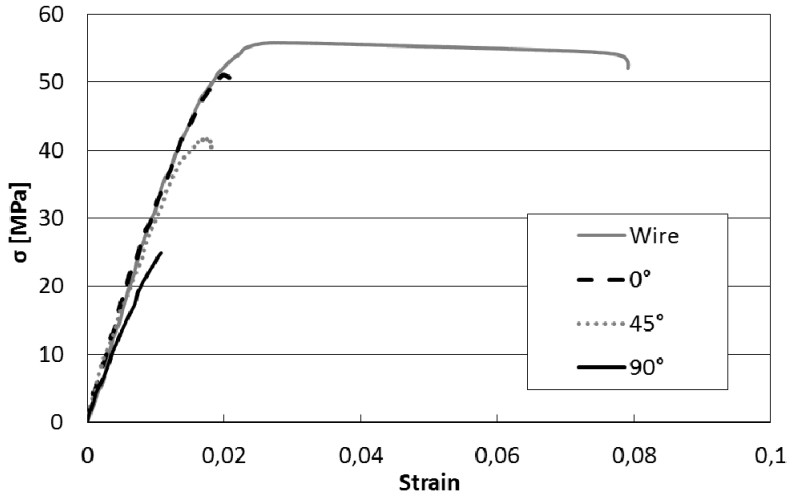

Figure 8.5 Representative tensile testing data for PLA at each raster orientation

In general, the results highlight a brittle behaviour for FDM specimens compared to the feedstock wire. However, 45° and 0° specimens show a little plastic behaviour compared to the 90° specimens that have a perfect brittle trend without plastic deformation. These results, showing the orthotropic properties of FDM specimens, confirm that the raster orientation has an important effect on the tensile strength, the Young's modulus and deformation at fracture.

In Figure 8.6, some representative shear stress vs. shear strain curves have been reported. As recommended by ASTM D3518-94, the slope of the curve between the point with a deformation of 2000 με and 6000 με is the shear modulus G_{12}. The mean vales of G_{12} obtained for PLA is 1246.57 ± 32.21MPa and 808.58 ± 17.80 MPa for ABS.

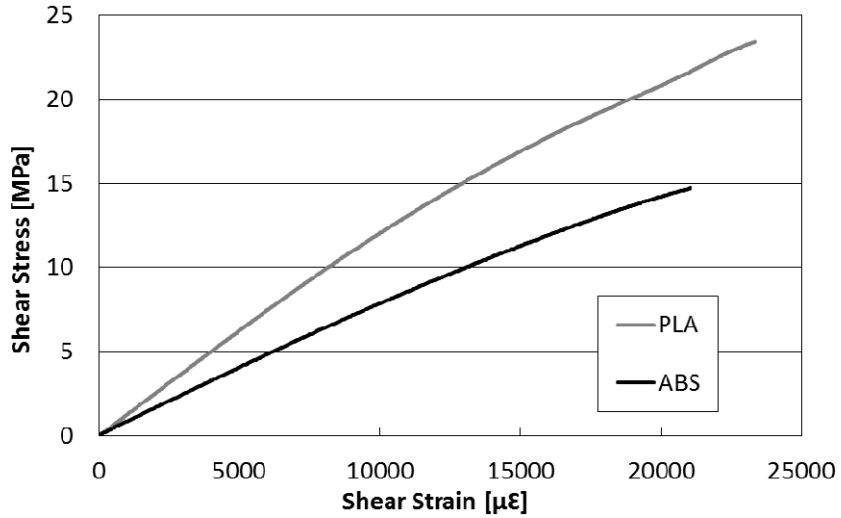

Figure 8.6 Representative shear stress - shear strain data for both PLA and ABS

Figure 8.7a for ABS and Figure 8.7b for PLA, show the comparison between experimental stress-strain curves of [+30/-30/0/-30/+30] specimens and CLT. In these figures, the dotted line represents the elastic modulus predicted by CLT. The values are 1.88 GPa for ABS and 3.17 GPa for PLA and these have been calculated using the measured Poisson's modulus of 0.344 for ABS and 0.330 for PLA. The mean experimental values are 1.86 ± 0.075 GPa for ABS and 3.35 ± 0.095 GPa for PLA. In Figure 8.7c, a comparison between experimental elastic modulus and CLT prediction has been reported. The difference between CLT and experimental vales are 1.07% for ABS and 5.37% for PLA. Finally, the mean UTS are 32.18 ± 0.47 MPa for ABS and 55.37 ± 1.44 MPa for PLA.

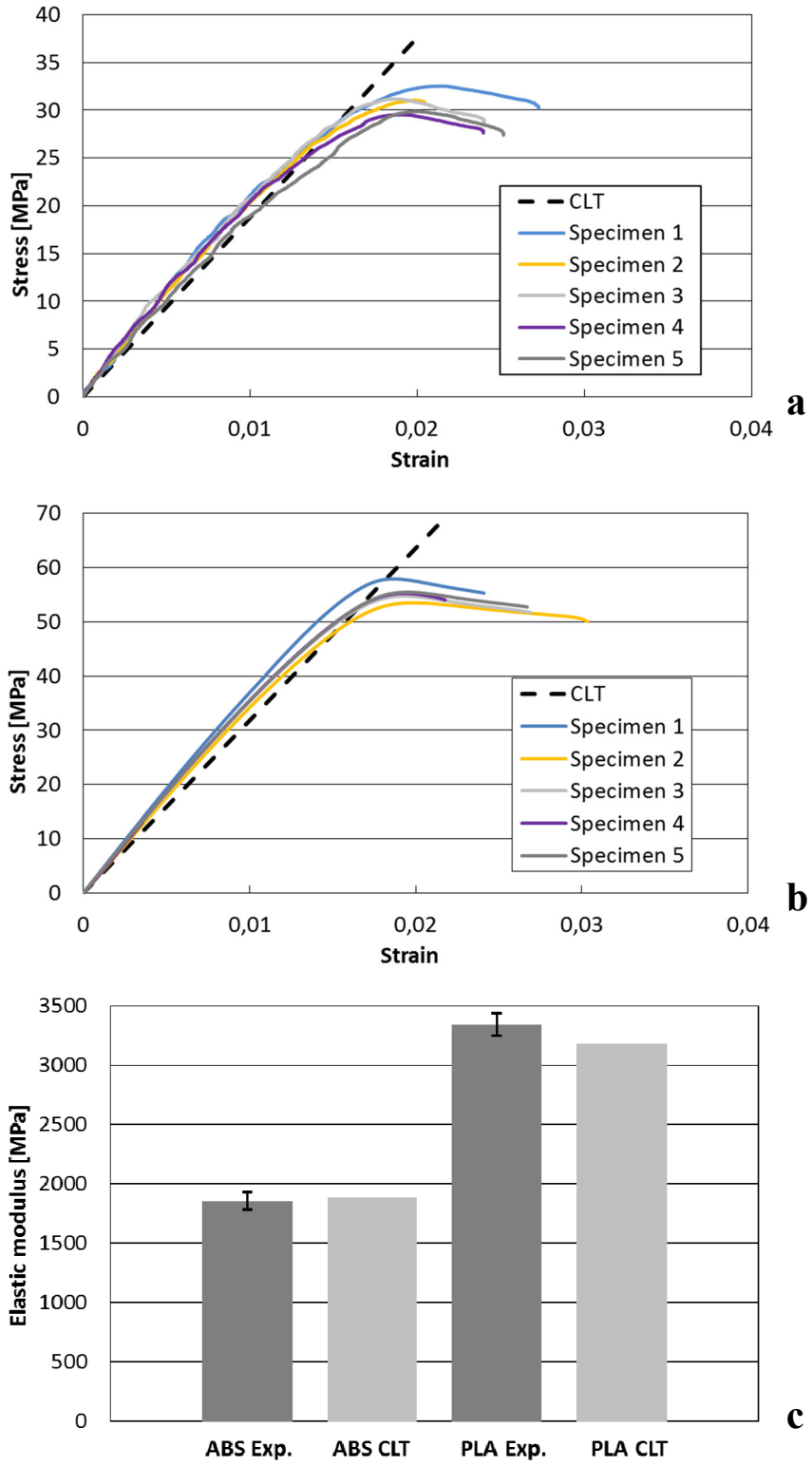

Figure 8.7 Experimental data vs. CLT for Abs (a) PLA (b) and comparison between elastic modulus (c)

8.2. Tensile-Impact of FDM parts

The results of the previous section highlight that the FDM printed parts show an orthotropic behaviour and that the CLT can predict in a good manner the elastic modulus of FDM models.

The aim of this section is to prove that these orthotropic properties are shown also in dynamic tests, such as the tensile-impact, and not only during quasi-static experiment. The tensile-impact test measures the amount of force needed to break a specimen under a high-speed tensile load introduced through a swinging pendulum or striker (Figure 8.8).

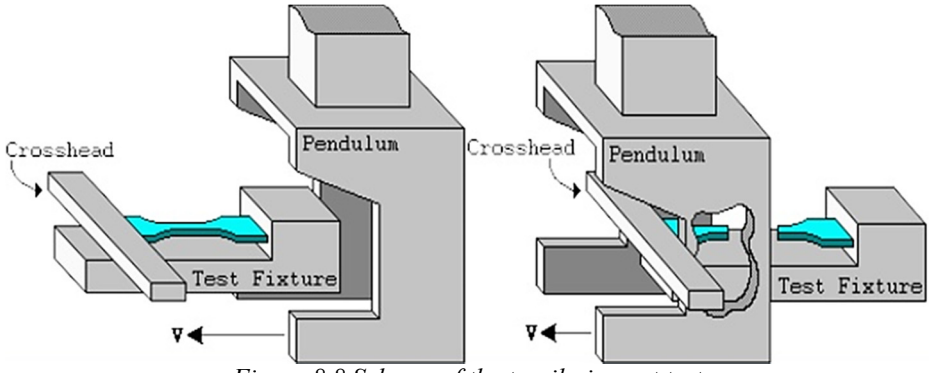

Figure 8.8 Scheme of the tensile-impact test

8.2.1. Materials and methods

In order to acquire a better knowledge of the orthotropic behavior of FDM parts during the tensile-impact tests, two types of ABS specimens have been tested:

- Single-layer (thickness t = 0,35 mm)
- Multi-layer (thickness t = 2 mm)

Moreover, this tests have been repeated for three layer orientations, i.e. 0°, 45°, 90°. In addition to the influence of the raster orientations, the influence of the impact speed has been studied. In order to carry out this part of the study, the energy of the striker has been fixed to 25 J and, employing additional masses, the speed of the striker has been changed. In particular, the Table 8.4 sums up the test parameters.

Table 8.4 Speed of the striker related to the total mass

Sample sets	**Speed** [m/s]	**Total mass striker** [kg]
A	3.78	3.492
B	3.02	5.492
C	2.67	6.992

In order to have the possibility to analyse statistically the results, ten samples for each typology of specimen have been printed. A total of 90 specimens have been printed.

The samples have been printed employing the same RepRap Prusa i3 described in the previous section 8.1.2. Also in this case, some parameters have been kept constant for every specimens and have been reported in Table 8.5. The bed temperature has been set to 90 °C and the nozzle temperature is 225 °C. Also in this case, the specimens have been fabricated with the minimum dimension of the part perpendicular to the build platform.

Table 8.5 Fixed printer parameters

Parameter	Value
Air gap [mm]	0
Layer thickness [mm]	0.35
Bead width [mm]	0.70
Number of contour lines	2

The shape of the specimens has been printed according to the standard UNI EN ISO 8256, type III (Figure 8.9) for the impact-tensile tests. Also in this case, the solid model has been sliced using the open source software Slic3r.

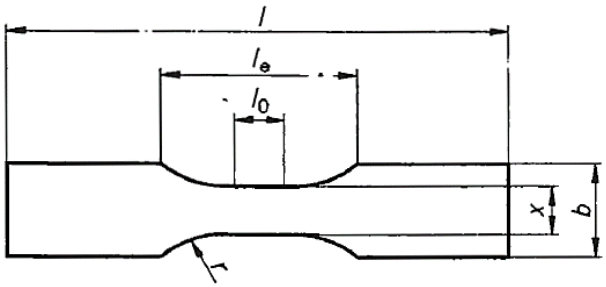

Figure 8.9 Type III specimen shape

In Table 8.6 the parameters for the specimen dimension of Figure 8.9 have been reported.

Table 8.6 Type III specimen dimension

Parameter	Value [mm]
l	80 ± 2
b	15 ± 0,5
x	10 ± 0,2
l_0	10 ± 0,2
l_e	30 ± 2
r	20 ± 1

In the next Figure 8.10, Figure 8.11 and Figure 8.12, an example, for each raster angle, of the specimens employed for the tests has been reported.

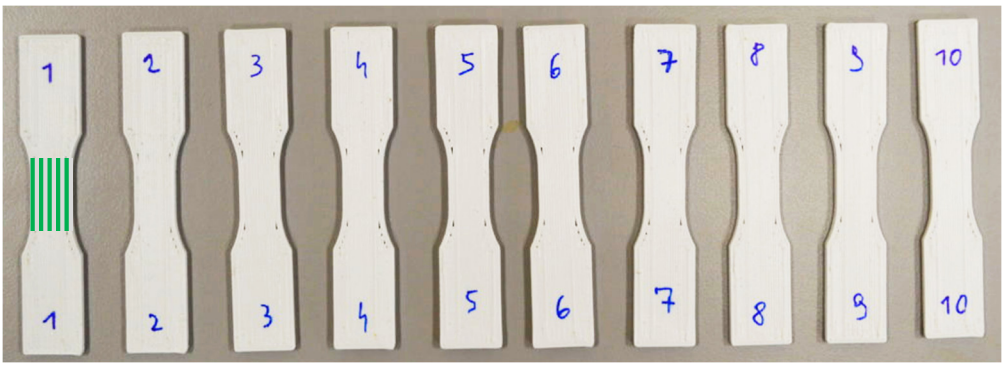

Figure 8.10 Multi-layer specimens with 0° raster orientation

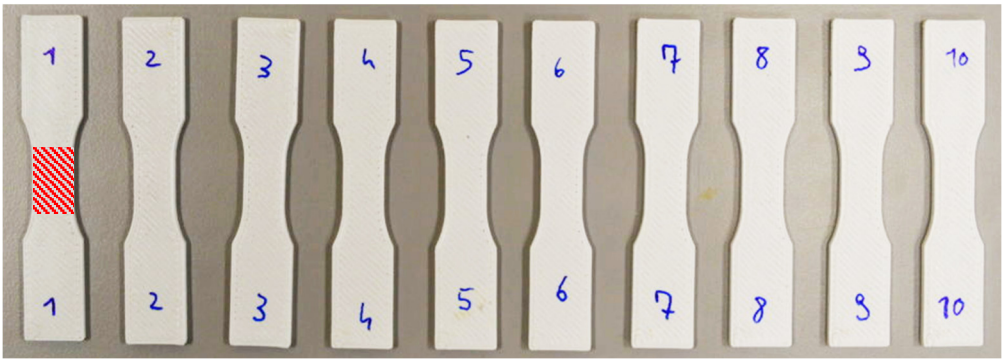

Figure 8.11 Multi-layer specimens with 45° raster orientation

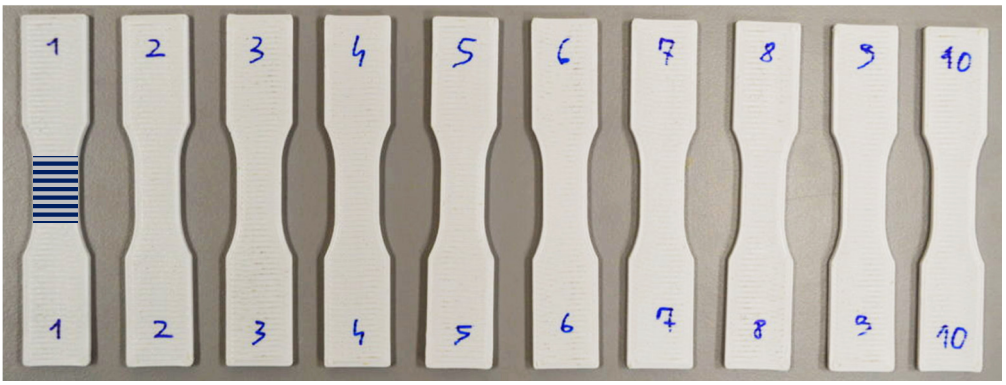

Figure 8.12 Multi-layer specimens with 90° raster orientation

For the tensile-impact tests of both single layer and multi-layers, an Instron CEAST 9350 with the software Visual Impact for the data acquisition and manipulation has been used. According to the machine setup, the A method of the UNI EN ISO 8256 and a 120 g clamp has been used. A 2.2 kN load cell has been mounted on this machine. This limitation avoids to repeat the same tests also for PLA as carried out in the previous section 8.1.

In order to not introduce local stress concentration due to excessive clamping force, the specimens have been mounted on the load train (Figure 8.13) employing a torque of 2.5 Nm on the clamps. However, this is not sufficient for the 90° specimen. Indeed, due to the clamp knurling that is parallel to the bead deposition, many failures of the specimens occurred near the clamp. To solve this problem a piece of sandpaper between the clamp and the specimens has been employed.

Figure 8.13 An example of specimen mounted in the grips in the temperature-controlled chamber

8.2.2. Results and discussion

In this section the results of the tensile-impact test will be presented. In the first part, the multi-layer tests will be analysed and then the single-layer results will be shown.

- *Multi-layer samples*

In the Figure 8.14, Figure 8.15 and Figure 8.16 the average stress-strain curve at different impact speeds and for each raster orientations have been reported. In Figure 8.14 can be observed as a higher impact speed produces higher stress in the stress-strain curves. While this difference is remarkable between the 3.78 m/s and 3.02 m/s speeds, the comparison between the two lower speeds, i.e. 3.02 m/s and 2.67 m/s, does not highlight this clear difference. Moreover, considering the absorbed energy, i.e. the area under the stress-stain curve, the three speeds show similar values. Indeed, the 3.78 m/s curve shows higher stress values, however the deformation is smaller than the other two curves.

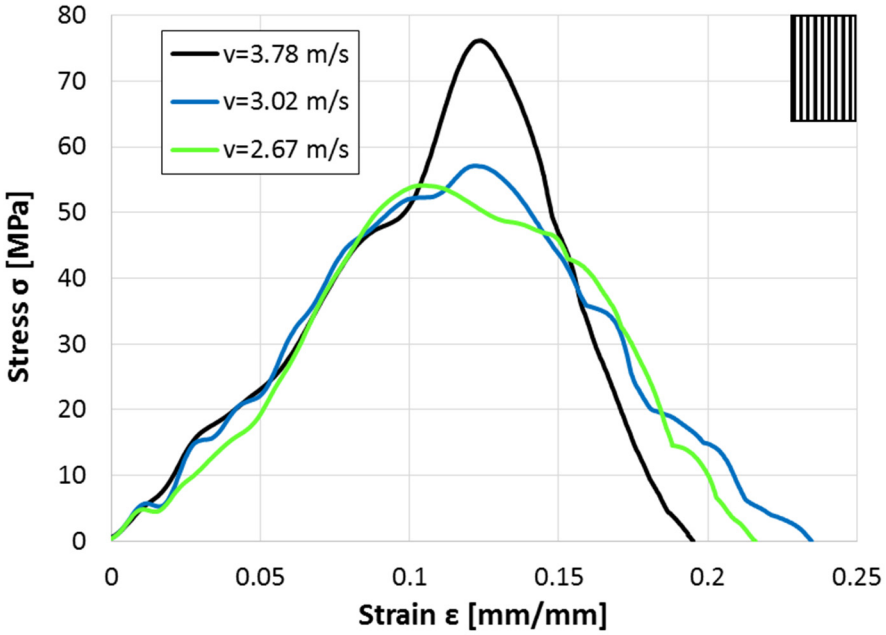

Figure 8.14 Multi-layer stress-strain curve for 0° specimen and for each impact speeds

Comparing the Figure 8.15 and the Figure 8.14, it is clear that there is a reduction of the maximum stress and the absorbed energy between 0° and 45° specimens. Moreover, for the 45° specimens, there is a small reduction of the maximum recorded stress between the 3.78 m/s and 2.76 m/s curves. Also in this case, it can be observed that the change in the absorbed energy is not remarkable between the different impact speed tests.

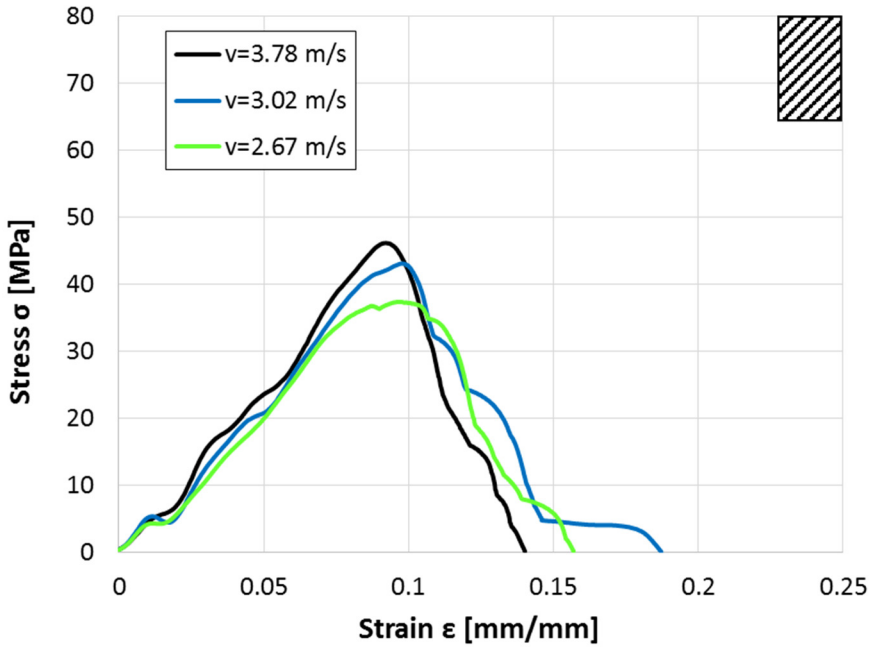

Figure 8.15 Multi-layer stress-strain curve for 45° specimen and for each impact speeds

Finally, in Figure 8.16 can be observed again a further reduction of the maximum stress and of the absorbed energy compared to the previous 0° and 45° cases. In the 90° specimens, the three curves at different speeds are almost overlapped, and consequently, the lower speed case that shows a higher stress value should not be considered as an actual result.

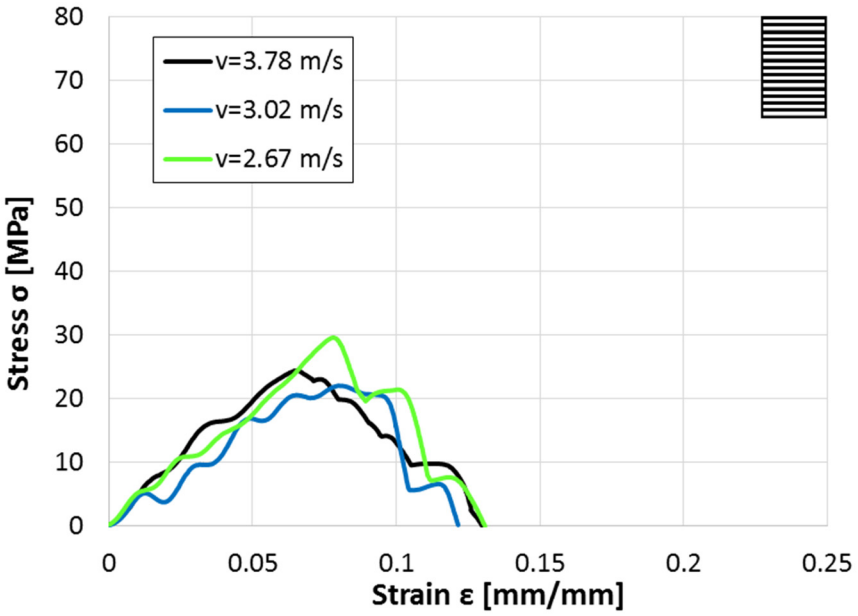

Figure 8.16 Multi-layer stress-strain curve for 90° specimen and for each impact speeds

In the next figures have been summed up the effects on the maximum stress (Figure 8.17) and on the absorbed energy (Figure 8.18) of the raster angles and impact speeds. Moreover, in Figure 8.17 has been reported in red the values of quasi-static tensile tests.

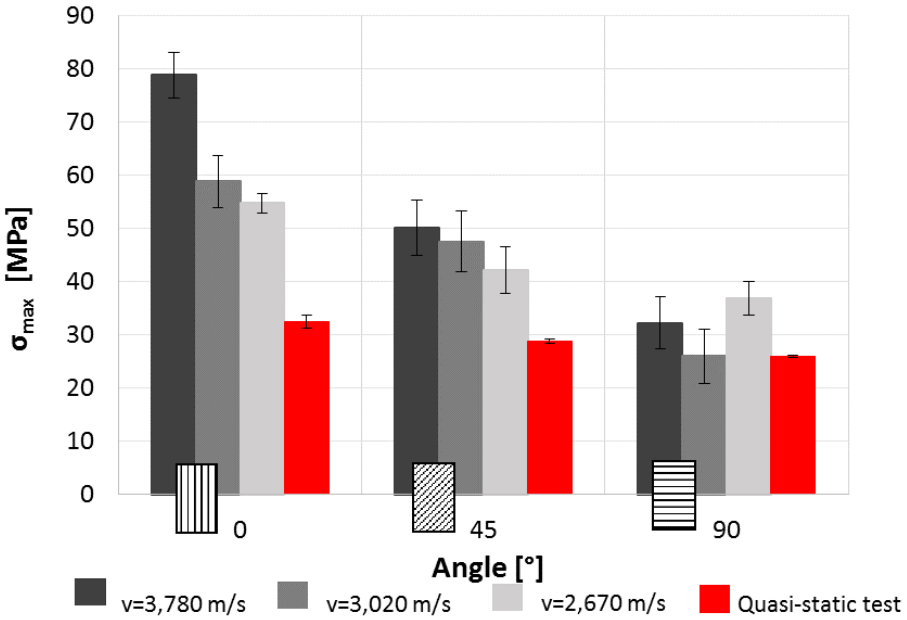

Figure 8.17 Effect on the maximum stress of the raster angles and impact speeds for multi-layer

In Figure 8.17 can be observed that increasing the raster angle there is a reduction of the maximum stress. This is true for each impact test speed. Moreover, for the 0° specimens there is a remarkable reduction of the maximum stress decreasing the impact speed (as already pointed out in Figure 8.14). This reduction become less clear for the 45° specimens and it is negligible in the 90° samples. However, considering the uncertainty, the variation that has been found in the three cases can be considered not relevant from a statistical point of view. The red band are the results obtained from quasi-static tensile tests. The results from this are quite lower than the dynamic values.

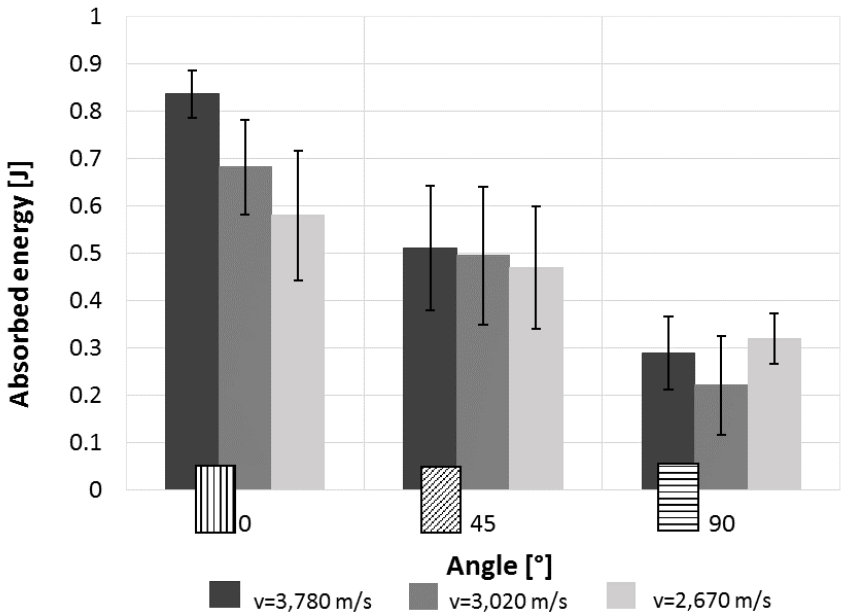

Figure 8.18 Effect on the absorbed energy of the raster angles and impact speeds for multi-layer

The Figure 8.18 highlights that the trend of the absorbed energy is comparable to the maximum stress trend. Indeed, increasing the raster angle there is a great reduction of the absorbed energy. Also in this case, the change due to the impact speeds are much more important in the 0°, become smaller in 45° case and are negligible in 90° samples.

In Figure 8.19 the fracture sections for the multi-layer specimens have been reported. From this figure, can be observed that the fracture path for the samples is related to the stacking sequence and that the fracture extends between the beads.

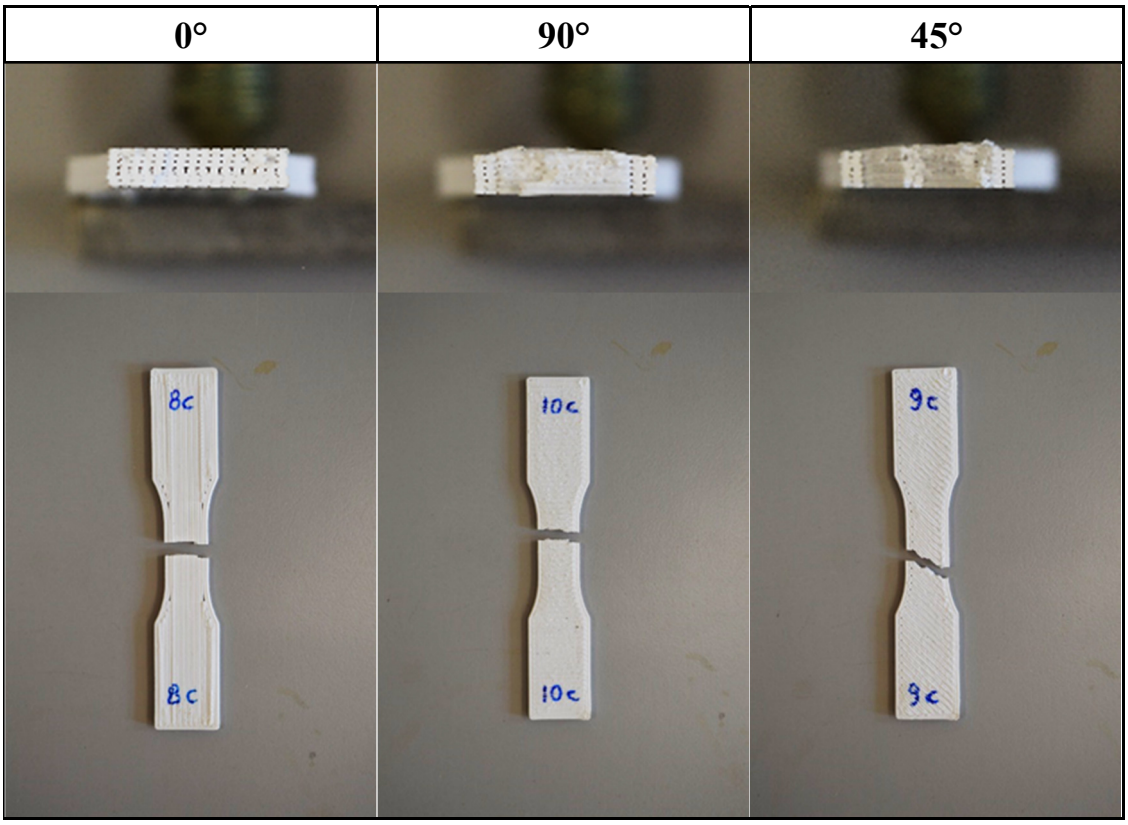

Figure 8.19 Fracture section for the multi-layer specimens

- *Single-layer samples*

The same analysis of the multi-layer specimens has been carried out on the single-layer samples. In Figure 8.20 the stress-strain curve for the 0° specimens has been reported. From the trends can be highlighted that the impact speed has no influence on both the maximum stress and absorbed energy. Indeed, the peaks of the three curves are near 50 MPa and the area under the curves is the same for each speed.

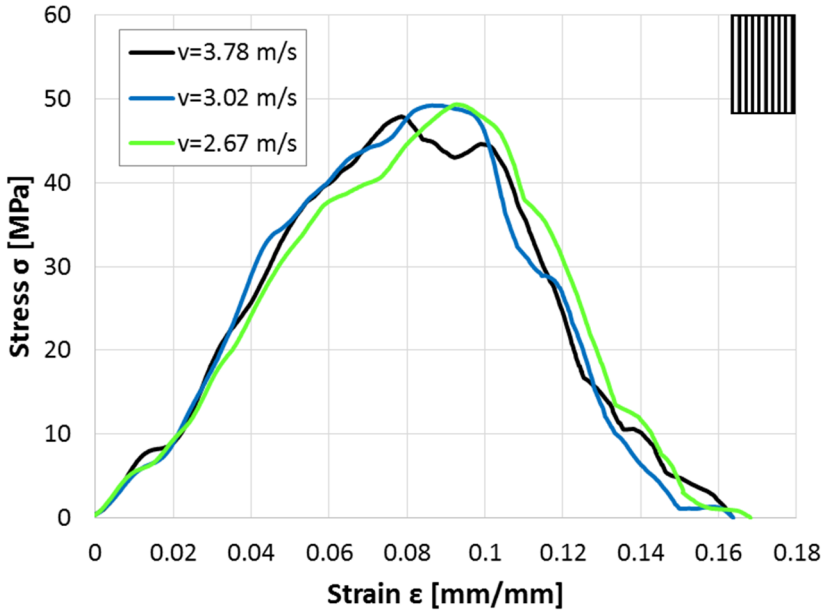

Figure 8.20 Single-layer stress-strain curve for 0° specimen and for each impact speeds

For the single-layer 45° specimens, there is a reduction of the maximum stress and absorbed energy compared to the 0° samples. Moreover, the changes due to the impact speed are not significant between 3.78 m/s and 3.02 m/s, while for 2.67 m/s, there is an important reduction of both maximum stress and absorbed energy.

In Figure 8.22, the trends for the 90° samples have been reported. As for the multi-layer specimens, there is a further reduction in both maximum stress and absorbed energy compared to the other stacking sequences. Also in this case as in the multi-layer, the behavior of the printed material is not influenced by the impact speed. Indeed, the maximum stress and absorbed energy is comparable for the three speeds.

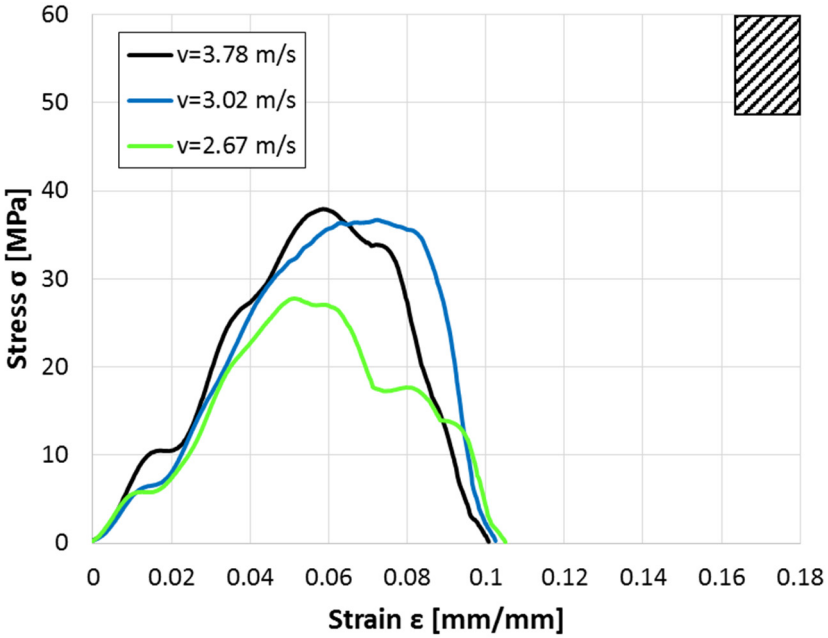

Figure 8.21 Single-layer stress-strain curve for 45° specimen and for each impact speeds

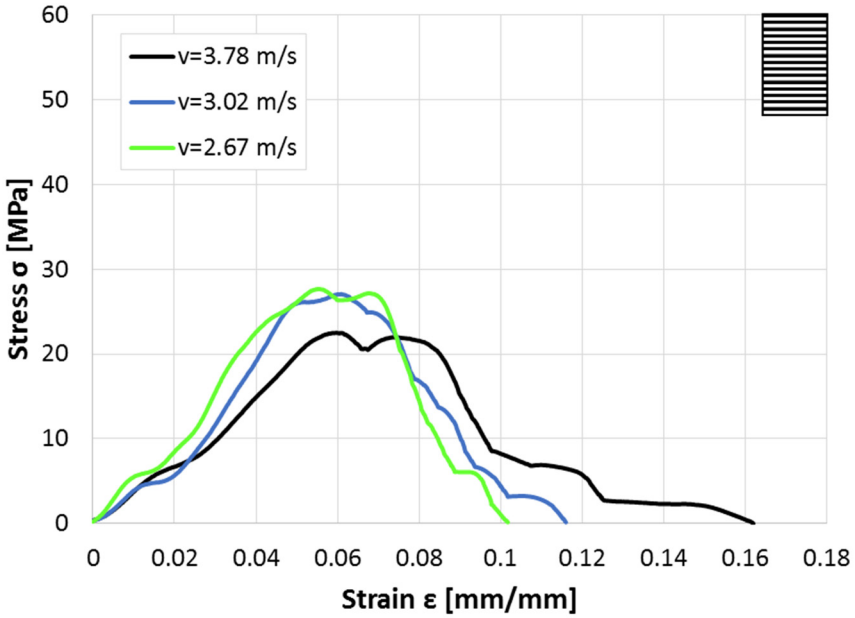

Figure 8.22 Single-layer stress-strain curve for 90° specimen and for each impact speeds

In the same way of multi-layer tests, the next figures summed up the effects on the maximum stress (Figure 8.23) and on the absorbed energy (Figure 8.24) of the raster angles and impact speeds.

Also for the single-layer tests is confirmed that increasing the raster angle there is a reduction of the maximum stress (Figure 8.23). However, in a clear way than for the multi-layer, the variation among the three speeds can be neglected because the stress values are the same for each speeds. Also in this case, the results from quasi-static tensile test are lower than the dynamic values.

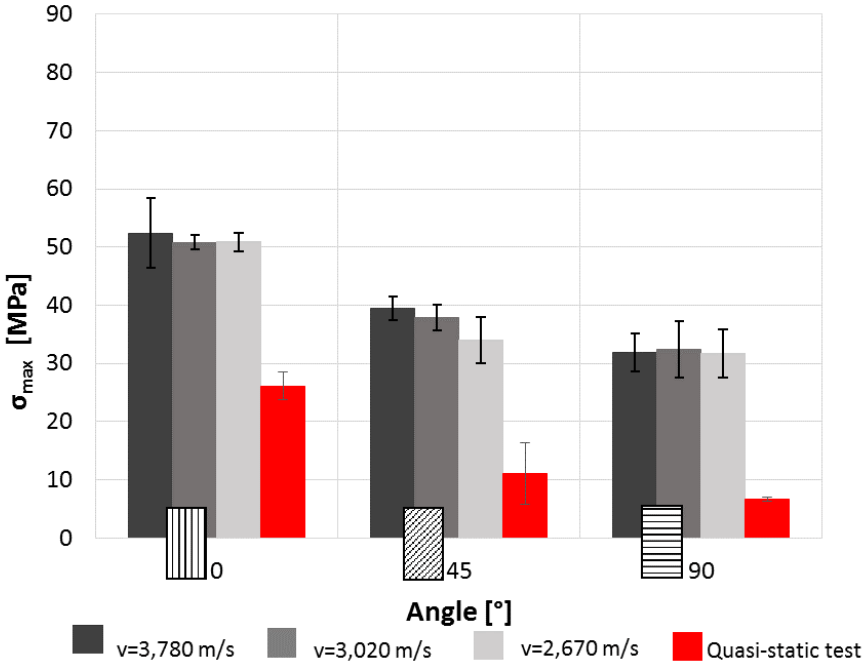

Figure 8.23 Effect on the maximum stress of the raster angles and impact speeds for single-layer

The Figure 8.24 highlights that the trend of the absorbed energy is comparable to the maximum stress trend. Indeed, increasing the raster angle there is a great reduction of the absorbed energy. Also in this case, the change due to the impact speeds are much more important in the 90°, become smaller in 45° case and are negligible in 90° samples. Finally, the same consideration for the absorbed energy that have been carried out for the multi-layer specimens can be repeated for the single-layer tests (Figure 8.24).

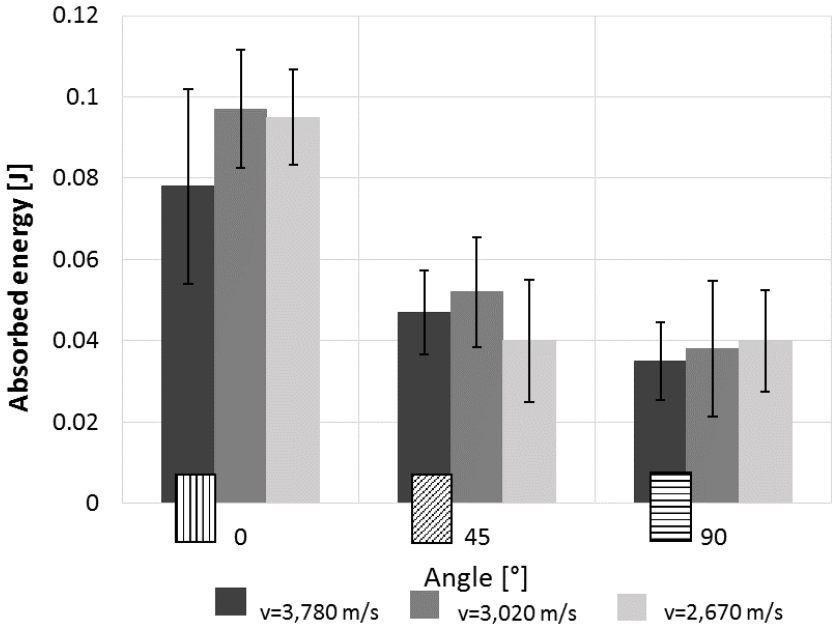

Figure 8.24 Effect on the absorbed energy of the raster angles and impact speeds for multi-layer

In Figure 8.25 an example of the fracture of the single-layer specimens has been reported. Also in this case, the fracture extends between the beads.

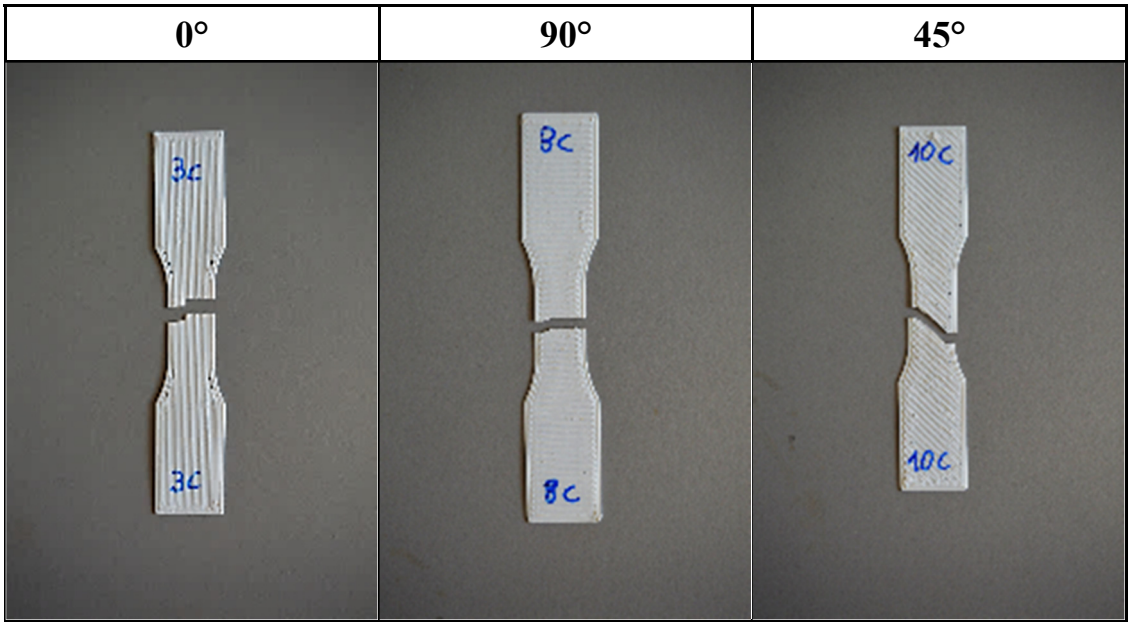

Figure 8.25 Fracture of single-layer specimens

8.3. Summary and conclusions

In this chapter, some preliminary studies on the mechanical behaviour of FDM parts have been done. The final aim was to prove that FDM parts show an orthotropic behaviour on both static and dynamic loads.

In the first section, the mechanical behaviour of FDM parts has been described using the classical laminate theory (CLT). In view of this aim, some mechanical parameters employed in CLT has been experimentally determined. The values of the Young's modulus in the longitudinal and transverse directions to the fibre (E_1, E_2) has been carried out by single layer tests conducted on specimens with 0° and 90° raster angles. The shear modulus (G_{12}) has been determined according to the ASTM D3518. The Poisson's modulus has been measured on five layers 0° specimens acquiring the longitudinal and transverse deformation by strain gauges. The comparison between the CLT and the experimental results has been carried out on specimens with a symmetric and balanced stack sequence [+30/-30/0/-30/+30]. Finally, two different material, ABS and PLA, have been employed to prove the validity of CLT prediction on several materials.

The tests on the wire show that the PLA has a Young's modulus and UTS values that are about twice the values of ABS even if it is more brittle. For both PLA and ABS, the wire are stiffer and stronger than the 0° single layer samples and this is probably due to the extrusion process that introduces some defects in the resulting specimens. The experimental results highlight the orthotropic behaviour of FDM specimens showing a reduction of the mechanical characteristics increasing the raster angle. The Young's modulus, increasing the raster angle from 0° to 90° decreases of 35.72% for ABS and 11.12% for PLA. Moreover, the mean UTS shows a reduction of 74.30% for ABS and of 55.22% for PLA changing the raster angle. Apparently, these results suggest that ABS has more marked orthotropic behaviour than PLA. One of the potential motivation of this PLA behaviour should be a better capacity of this material to bond each bead to the other. In addition, tests on 45° specimens have been carried out. For both materials analysed, the 45º specimens have an intermediate mechanical behaviour between the 0° and 90° even if the mechanical behaviour is nearer to 90° than 0°.

The CLT has showed a high capacity to predict the elastic modulus of ABS and PLA laminate obtained by FDM. Furthermore, the results are in according with other models present in literature [89], that showed higher errors between experimental results and model prediction (from -4.7% to 6.6%).

In the second section, a study on tensile-impact of FDM specimens has been carried out. The aim of this section was to prove that FDM parts show an orthotropic behaviour also during dynamic test such as tensile-impact. Two typology of ABS specimens, i.e. single-layer and multi-layer, have been tested. Moreover, these tests have been repeated for three layer orientations, i.e. 0°,

45°, 90°. In addition to the influence of the raster orientations, also the effect of the impact speed has been studied.

The results, for both the multi-layer and single-layer, show that increasing the raster angle there is a reduction of the maximum stress and of the absorbed energy. This is true for each impact test speeds. Moreover, for the 0° multi-layer specimens there is a reduction of the maximum stress decreasing the impact speed. This reduction become less clear for the 45° specimens and it is negligible in the 90° samples. For the single-layer specimens, the variation among the three speeds can be neglected because the stress values are the same for each speeds. However, considering the uncertainty the variation of the maximum stress related to the impact speed can be considered, in general, not relevant in both multi-layer and single-layer samples. The same observation on the influence of the impact speed can be done for the absorbed energy.

In conclusion, the FDM parts clearly show an orthotropic behaviour in both quasi-static and dynamic loads and it has been proved that the CLT can predict the quasi-static behaviour of FDM parts.

9. Residual stress in Fused Deposition Modelling parts

The distortion of the part during the print is one of the most important issues in the FDM process. The rapid heating and cooling cycles of the feedstock material could produce accumulation of residual stresses during part building up [84, 90]. This residual stress could lead to distortion and de-layering problems, which seriously affect the shape and the final dimensions of the parts or it could prevent the finalization of the objects due to unsticking of the part from the bed. In order to reduce these issues, a common technique is to use a heated bed with some type of adhesive on the surface of the bed. Although, such procedures help to reduce distortions, they can increase the residual stresses of the final part.

Several techniques can be employed to measure the residual stress in plastic parts. One of the most well-known is the incremental hole-drilling method [10]. In this semi-destructive technique, the introduction of a hole into a stressed body causes localized stress relaxation and deformation around the hole. The strain distribution can be measured by a strain gage rosette or by an optical technique [91]. Until now, some works have dealt with experimental measurements to determine residual stress distribution in plastic parts [92-94] but no one in FDM parts. Turnbull et al. [92] carried out a comparison among several techniques in order to measure residual stresses in polymers such as Polycarbonate, ABS and Nylon. They concluded that the hole drilling is in accordance with the other techniques and, even if it shows some problems due to the calculation procedures, it can be employed as a valid measurement method. Nau et al. [93] highlighted that the procedures and process parameters valid for stress analysis in metallic materials cannot be applied in plastic materials. They pointed out that the surface preparation of specimens, the strain gauge bonding, and the drilling speed are critical issues in order to obtain a correct measure. However, both Turnbull et al. [92] and Nau et al. [93] did not consider the local reinforcement effect that the installation of a rosette produces in materials that have a low Young's modulus. Finally, Magnier et al. [13] carried out a deep investigation on the influence of material viscoelasticity, room temperature, and local reinforcement of the strain gauge on the measure of deformation by HDM of plastic materials. They pointed out how these parameters can produce a difference up to 30% between the results recorded by strain gauge and DIC.

Only one paper has tried to deal with the residual stress issues in FDM by numerical simulation. Zhang and Chou [95], using simplified material properties and boundary conditions, have simulated different deposition patterns and have demonstrated the feasibility of using the element activation function to reproduce the filament deposition. They found that residual stress is higher in the first deposited layer compared to the last layer and that there was a modification of the residual stress distributions changing the tool-path pattern. However, they did not validate their

model using residual stress measurements but only by comparing the distortion of the printed part and the numerical prediction.

In this chapter, the aim is to measure the residual stress in FDM parts made of ABS employing the hole-drilling method. In order to avoid the local reinforcement of the strain gage, an optical technique, i.e. ESPI (electronic speckle pattern interferometry), is employed to measure the displacement of the surface due to the stress relaxation. Furthermore, the effect of the stacking sequences on the residual stress distribution has been investigated. Four stacking sequences have been printed, i.e. ±30°, ±45°, 0°/90° and 0° only. In addition, the residual stress distribution on each side of the specimen has been investigated; for this purpose, the measures have been carried out on the top, i.e. the last printed layer, and the bottom of the specimens, i.e. the first printed layer.

9.1. Materials and methods

Due to the orthotropic behaviour of FDM parts, the isotropic model usually implemented in commercial hole drilling software cannot be used. Thus, an orthotropic FEM model, based on the results of the previous chapter, has been developed to calculate the displacements due to some known stress cases. The combination between the experimental displacement data and the FE model allows calculating the residual stress in the parts.

The same RepRap Prusa i3 of the previous chapter has been employed to produce the specimens. These have a rectangular shape and the dimensions of 80 x 40 x 7 mm. Four stacking sequences have been studied, i.e., the raster angles are ±30°, ±45°, 0°/90° and 0° only. A layer with a 0° raster angle has the deposited beads parallel to the major side of the specimen. Also in this case, the samples have been fabricated with the minimum dimension of the part perpendicular to the build platform. The Figure 9.1 shows the coordinate system for the deposition and for the residual stresses.

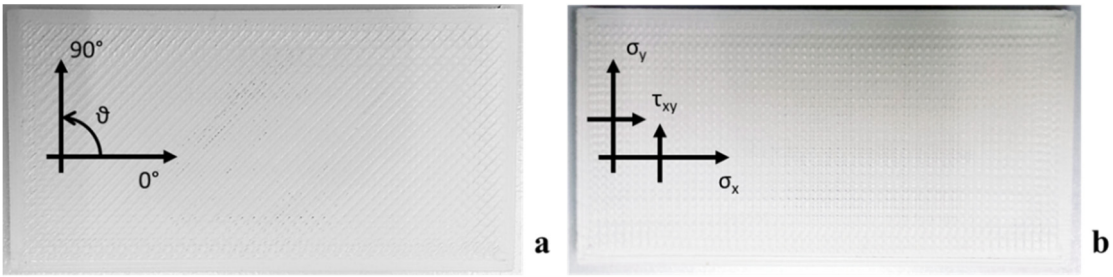

Figure 9.1 Specimen examples with ± 45° (a) and 0°/90° (b) stacking sequence

The parameters reported in Table 9.1, such as the layer thickness or the number of contour lines, have been kept constant for every specimen.

Table 9.1 Fixed printer parameters

Parameter	Value
Air gap [mm]	0
Layer thickness [mm]	0.2
Bead width [mm]	0.67
Number of contour lines	3
Bed temperature [°C]	90
Nozzle temperature [°C]	215

The bed temperature has been set to 90 °C and some glue on the bed has been employed to reduce the warping effect. The solid model, created using a 3D CAD, has been sliced using the open source software Slic3r.

The measure of the residual stresses has been carried out on three different samples for each stacking sequence. Moreover, to obtain a better knowledge of the residual stress in the top and the bottom of the samples, three holes have been drilled on the top of each specimen, i.e. starting from the last layer deposited, and three on the bottom, i.e. starting from the first layer deposited (Figure 9.2). An average value for each side of the specimen has been calculated based on the data of these three holes.

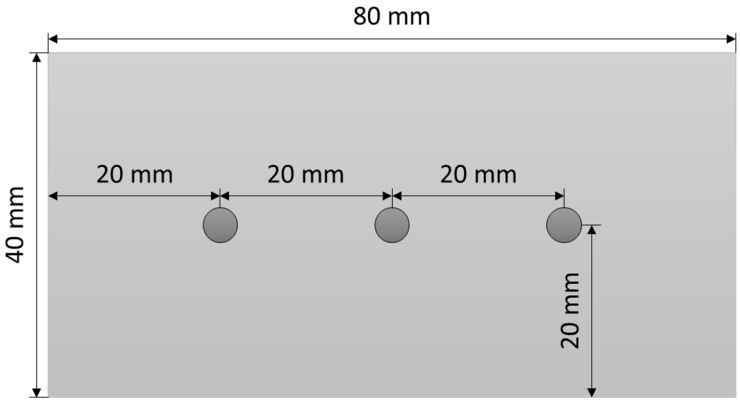

Figure 9.2 Holes position on the top and the bottom of the specimens

The holes were drilled by means of a high-speed turbine that is mounted on a precision travel stage. Turbine rotation speed was set to 5000 rpm after some preliminary tests that indicated that this speed allows obtaining good quality holes [90]. The cutter is made by tungsten coated by TiN and it has a nominal diameter d =1.59 mm. Compressed air was activated during the test to clean the surface of the sample by the formation of drilling chips. The holes were drilled to a depth of 0.6 mm through 30 drill increments to contain the temperature during the drilling phase on lower values. In order to reduce the computational time, the residual stress calculation has been done on 15 drill increments.

A diode pumped solid-state laser source (λ=532 nm) was used to shine the sample and to generate the speckle pattern. The laser beam is divided in two parts by a beamsplitter and delivered by two optical fibres. The beam emerging out from the first fibre is collimated and then directed towards the sample at a given angle (α=54°). The beam emerging from the second fibre, instead, is directed towards the CCD matrix of the camera and acts as a reference beam. The CCD camera (640x480 pixel) itself is placed at a given angle with respect to the normal to the sample (β=34°). Light diffused by the sample interferes on the CCD matrix with the reference beam. Four-step temporal phase shifting algorithm was adopted in order to obtain the phase [15, 16]. This means that four reference images are taken initially having a π/2 phase difference among each other. Another set of four images is, analogously taken for each drill increment. These intensity patterns were subtracted from the reference intensity pattern recorded on the sample before starting the drilling procedure. This operation allows obtaining fringe patterns encoding the information about the displacement experienced by the sample along the sensitivity vector.

9.2. Numerical model description

In this study, the integral method has been used to calculate the residual stresses. In the ESPI technique, a reference set of phase-stepped images of the specimen surface around the hole is acquired before the start of hole drilling and then after each incremental increase in hole depth. The images acquired after each increment in depth are correlated with the previous set to calculate the incremental displacements of the surface around the hole. The relationship between the measured incremental displacements **d** and the stresses **σ** within each step can be expressed as a matrix equation [7]:

$$\mathbf{D\sigma} = \mathbf{d} \tag{9.1}$$

where **D** is a matrix, **σ** and **d** are vectors. Matrix element D_{ij} represents the incremental surface displacements measured after hole depth increment i caused by a unit stress within increment j. For ESPI measurements, each camera pixel provides an information of the displacements and thus the vector **d** represents the n measured pixels around the drilled hole, where n is typically millions of pixels. Because of this excess of data, the equation (9.1) is overdetermined and can be solved by using a least square method:

$$\mathbf{D}^{\mathrm{T}}\mathbf{D\sigma} = \mathbf{D}^{\mathrm{T}}\mathbf{d} \tag{9.2}$$

The computation of the residual stress has been carried out calculating the matrix **D** using a finite element model, measuring the incremental displacements **d** and then solving the equation (9.2) to determine the stresses **σ**.

The orthotropic behaviour of FDM parts requires the development of an orthotropic FEM model for each raster orientation case under study. The required **D** matrix has been calculated

considering the actual values of the hole diameter, the depth of the hole and steps of the drilling procedure. A SOLID185 layered element has been employed to have the possibility to simulate the raster orientation of each layer. The mechanical properties of the single layers have been based on the data from the previous chapter 8. In Figure 9.3 the mesh structure of the model has been reported.

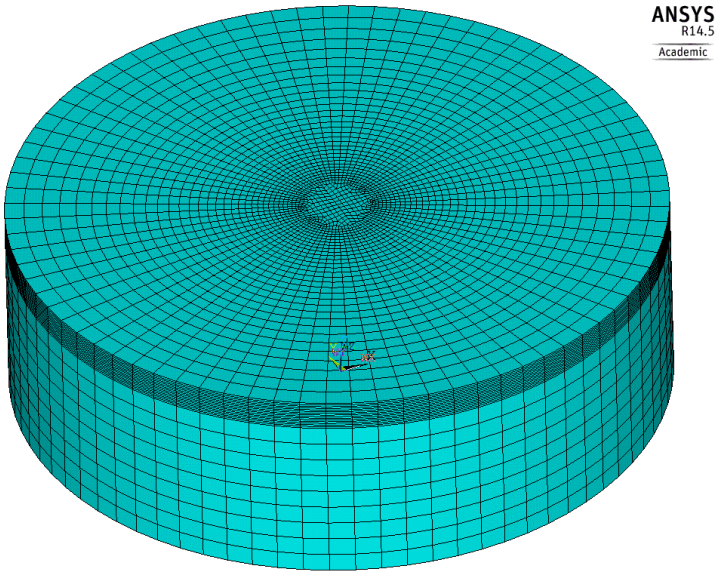

Figure 9.3 Finite element model mesh

For an easier meshing process and to reduce the computational time, only a cylindrical zone near the hole that has a radius of 8 times the radius of the hole has been modelled. In order to better follow the displacement field without increasing the computational time, the mesh is finer near the hole, where higher displacement was expected. For the same reason, the elements on the top of the model, for the entire drilling depth, have the same height of the calculation steps (i.e. 0.04 mm), while elements of the lower layers are thicker (i.e. 0.4 mm). Each step of hole-drilling process has been simulated, using a birth and dead technique, by removing elements at the hole area, applying loads on the elements forming wall of the drilled hole, and then calculating corresponding displacements around the hole. This procedure has been repeated until the whole hole has been simulated. For each depth increment, three load cases have been considered: $\sigma_x = 1\ MPa$, $\sigma_y = 1\ MPa$ and $\tau_{xy} = 1\ MPa$. To apply each of these loads, the equivalent radial and hoop stress distributions were applied simultaneously to the hole face according to Akbari et al. [96].

9.3. Results and discussion

Due to the low melting point of the ABS, the effects of the local increase of temperature due to drilling speed should be considered. The drilling speed has been set to 5000 rpm after some preliminary tests that have been summed up in Figure 9.4. In this Figure, the hole macrography

and thermograms comparison between 5000 rpm (Figure 9.4a, Figure 9.4b) and 50000 rpm (Figure 9.4c, Figure 9.4d) have been reported.

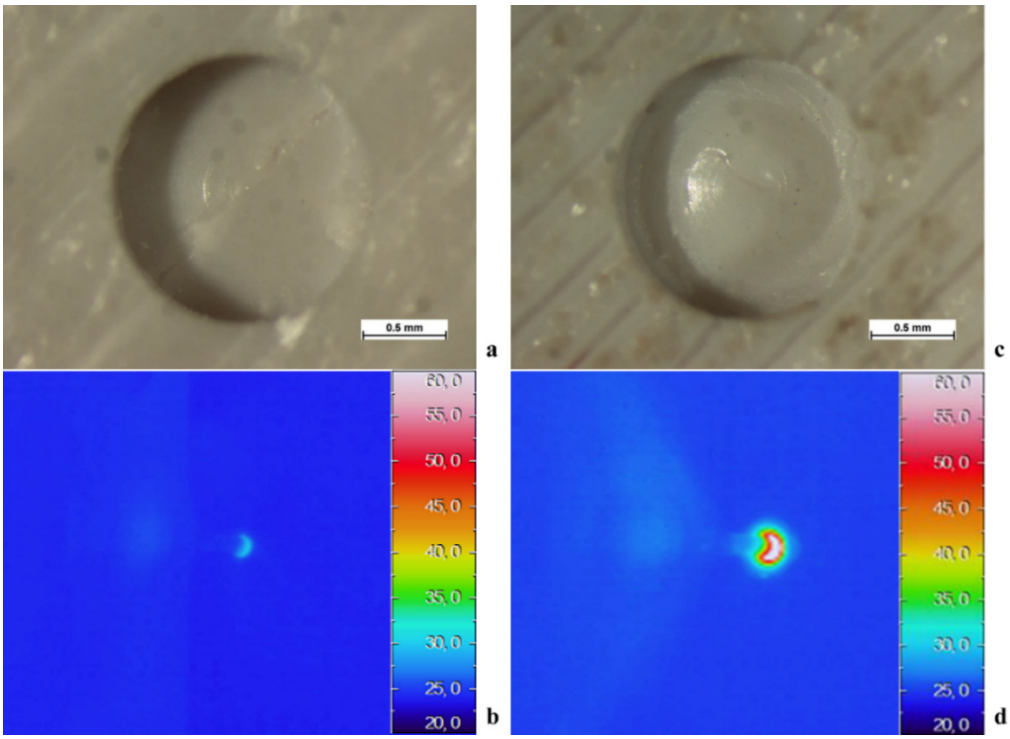

Figure 9.4 Hole macrography and temperatures maps comparison between 5000 rpm (a, b) and 50000 rpm (c, d).

The temperatures comparison between Figure 9.4b and Figure 9.4d shows that increasing the drilling speed from 5000 to 50000 rpm leads to an increase of temperature from 31.9 °C to 77.9 °C. This could explain the difference in the hole quality between the two drilling speeds as reported in Figure 9.4a and Figure 9.4c. The hole bottom is flat and regular for the 5000 rpm drilling speed whereas, for 50000 rpm, there is a central bulge that is probably due to a local boiling of the ABS material during the drilling process.

In Figure 9.5 an example of fringe patter for a 0/90° has been reported. These type of images, that have been obtained subtracting two intensity patterns in different drilling steps, encode the information about the displacement experienced by the sample along the sensitivity vector. Employing a four-step temporal phase shifting algorithm is possible to obtain the displacement maps near the drilled hole (Figure 9.6).

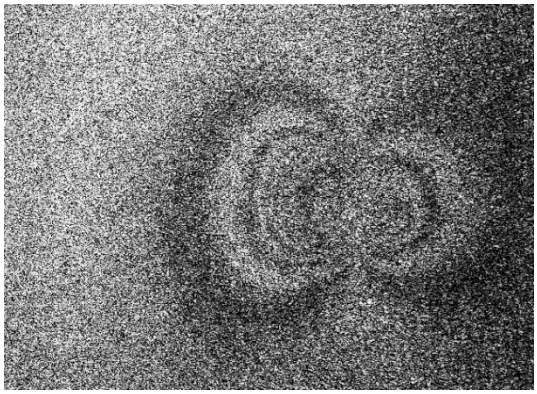

Figure 9.5 Example of fringe pattern for the sample 0/90°

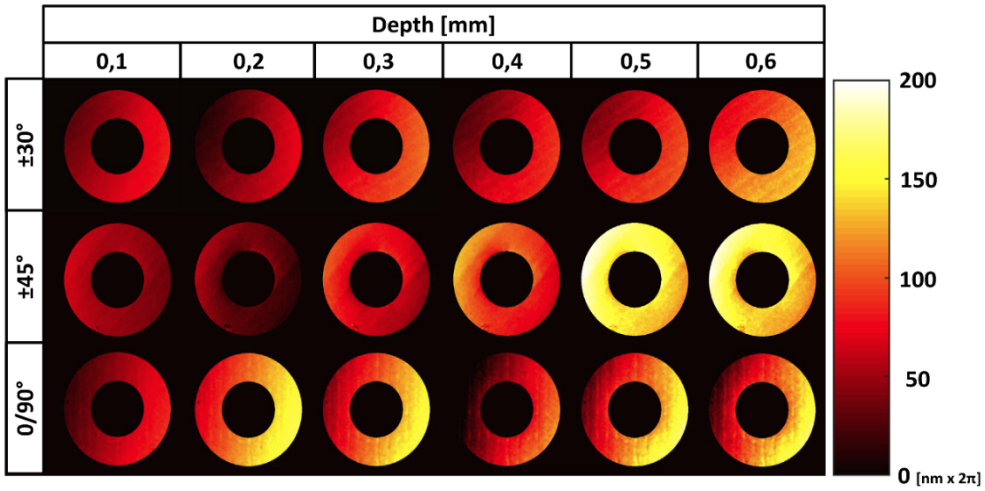

Figure 9.6 Example of displacements maps in some stacking sequences

The Figure 9.7 and Figure 9.8 show the residual stresses trends, σ_x, σ_y and τ_{xy}, for the four stacking sequences. The residual stresses on each side of the specimen, i.e. top and bottom, are the average values calculated based on the data of the three drilled holes per side. In general, as can be point out in Figure 9.7, for σ_x and σ_y there are some differences between the stacking sequences analysed. These differences are remarkable near the surface of the specimens, i.e. until 0.2 mm, but after this depth, there are no clear differences between the configurations. The residual stresses for the ± 30° configuration (Figure 9.7b and Figure 9.7g), in absolute value, are higher than the other configurations both on the top and on the bottom of the specimens. Moreover, this stacking sequence shows the highest value of residual stress recorded during this experimental campaign (Figure 9.7g). Indeed, the σ_y residual stress on the bottom reaches a value 6 MPa near 0.3 mm of depth. Considering that the yielding point of ABS is 26 MPa, a value of 6 MPa is more than 20% of the yielding point of the material. The ± 45° should be the best configuration to have low residual stresses in the specimens. In the σ_x (Figure 9.7b) and τ_{xy} (Figure 9.8) directions, the residual stresses are near the zero on both the top and the bottom of the specimens. The σ_y (Figure 9.7f) direction shows values higher than the other two directions but, however, lower than the other configurations.

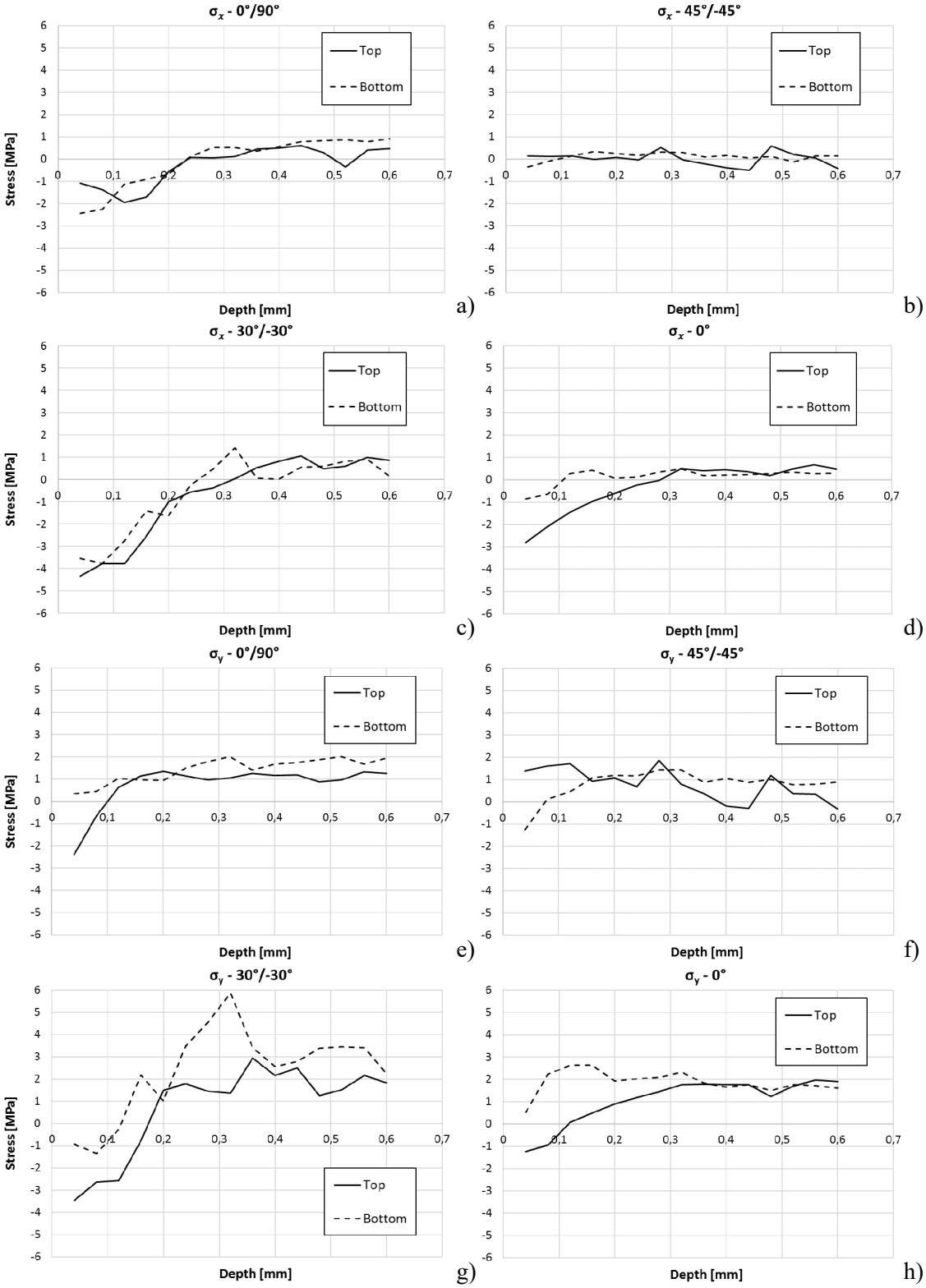

Figure 9.7 Residual stresses measured in σ_x and σ_y directions on the top and the bottom of the specimens

As can be point out in Figure 9.8, for the τ_{xy} cannot be observed any significant difference among the stacking sequences and the side of the specimens. Indeed, the values of residual stress are roughly between -1 MPa and 1 MPa in all configurations.

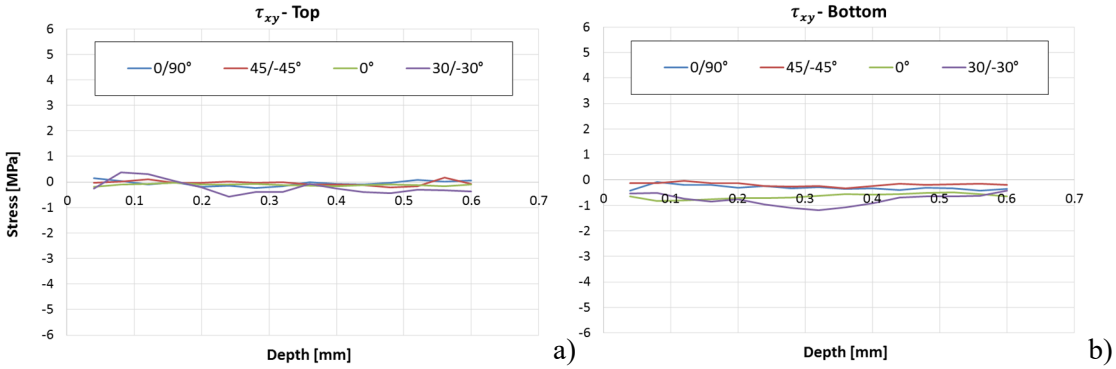

Figure 9.8 Residual stresses measured in τ_{xy} direction on the top and the bottom of the specimens

Although the bottom of the FDM part that tends to warp during the printing phase and it has been constrained by the glue, there are no clear differences between the top and the bottom of the specimens in all configurations. Generally, for the σ_x direction, there are compression values near the surface of the specimens until the depth of 0.2 mm. After this value of depth, the specimens show low value of tensile residual stress in all configurations. A similar trend with lower value of residual stress near the surface and tensile stress in the inner part of the sample can be highlighted also for the σ_y. Although in this direction, the magnitude of the residual stress in the inner part of the specimen is higher than the σ_x direction.

9.4. Summary and conclusions

In this chapter, the measure of the residual stresses in FDM printed specimens has been carried out by the hole-drilling method. An optical technique, i.e. ESPI, has been employed to measure the displacements produced during the hole drilling procedure. This technique allows avoiding local reinforcement due to strain gauge rosette that is a serious issue in materials, such as ABS, that have a low Young's module. Furthermore, the effect of the stacking sequences on the residual stress distribution has been investigated. Four stacking sequences have been studied, i.e. ±30°, ±45°, 0°/90° and 0° only. Moreover, the residual stress distribution on each side of the specimen has been studied, measuring the stresses on the top and the bottom of the samples. The specimens have been made of ABS and they have the dimensions of 80 x 40 x 7 mm.

Some preliminary tests have been carried out to determine the optimal drilling parameters. These have highlighted that the local increase of temperature due to the drilling procedure can seriously influence the quality of the hole. The thermographic analysis shows an increment of the temperature from 31.9 °C for 5000 rpm to 77.9 °C for 50000 rpm. This is confirmed by the macrographs that show a regular hole with a flat bottom for the lower drilling speed, whereas for the higher, there is a central bulge. This is probably due to a local boiling of the material during the process.

The results show that, whereas for τ_{xy} cannot be observed any difference among the stacking sequences as well as the sides of the specimens, for σ_x and σ_y there are some differences. These

are remarkably near the surface of the specimens, i.e. until 0.2 mm, but after this depth, there are no clear differences among the studied configurations. Whereas the ± 30° configuration is the worst stacking sequence because it shows the highest values of residual stresses, the ± 45° should be the best configuration to have low residual stresses in the specimens. Moreover, the comparison between the top and the bottom of the specimens shows no clear differences in all configurations. Finally, the highest value of residual stress recorded during this experimental campaign is 6 MPa and considering that the yielding point of ABS is 26 MPa, a value of 6 MPa is more than 20% of the yielding point of the material. This result confirms that residual stress management in FDM part is an important issue that must be properly addressed and taken into account in order to reduce warping effects and delayering problems in the finished part.

10. Conclusion

This chapter presents an overview of the research activities and the most important results reached into this dissertation. The purpose of the research was to study the residual stress issue in innovative manufacturing techniques, i.e. Friction Stir Welding and Fused Deposition Modelling. In FSW, though the temperature does not reach the fusion temperature of the materials, the residual stresses values can be important. This is due to the relevant force involved during the weld and, thus, the rigid clamping used in FSW. This avoids the contraction of the materials during the cooling phase and results in generation of residual stresses.

On the other hand, in FDM, the model is built as a layer-by-layer deposition of a feedstock material. Due to this approach, it is possible to build a part with almost any shape, both internal and external. However, the part cools down layer by layer during the deposition and, consequently, there is thermal variation and different cooling rates from one layer to the other. This produces internal stresses between layers, uneven shrinkage, de-layering problems, warping, and the relatively associated problems especially with larger parts. Often the warpage of the part can prevent the finalization of the objects due to unsticking problems from the bed.

Taking into account the previous considerations, the study of the residual stresses is really important for these two innovative manufacturing techniques. In order to carry out this study, the two lines of investigation have been divided into steps:

1. Residual stress in Friction stir welding:
    - The experimental setup to measure the temperature field on both FSW and LAFSW has been developed. Using a thermocamera, the whole temperature field can be measured and recorded. This allowed to carry out a study on the influence of the distance laser spot - FSW tool and of the laser source power on the temperature. The results showed that the distance between laser spot and FSW tool is a critical parameter that can influence in a strong manner the beneficial effect of the presence of the laser in FSW. Indeed, using a shorter distance between laser and FSW can be reached a higher temperature in front of the tool also by a lower laser power.
    - The experimental thermal results of the previous point have been employed to validate the FSW and LAFSW numerical models. These can predict the temperature and residual stresses changing the process parameters or the clamping configurations. The validation of the models has been done also by X-Ray diffraction residual stress measurements. The results showed that there is a good agreement with the experimental data for both thermal and residual stress values.
    - Because the clamp system constrains in FSW are a big issue for residual stress generation, employing the previous numerical model, a study on the influence of the clamps

configuration on residual stresses has been done. The results showed that small changes in the clamp configuration could influence the residual stress in a serious manner. This highlighted that an accurate design of the clamp system should be done, also employing numerical model.

- The comparison between traditional FSW and LAFSW has been done. The results showed that the longitudinal residual stresses are lower for the LAFSW technique compared to traditional FSW. On the other hand, the transverse residual stresses are not influenced by the laser pre-heating effect. Finally, changing the pre-heating laser power, the residual stress values do not change in an appreciable way.
- X-Ray diffraction experimental measurements have been done on FSW aluminium-titanium lap-joint. In particular, the effect of the welding speed on the residual stresses has been studied. The comparison among the three different speeds showed that, for the longitudinal residual stress, there is not significant difference changing the welding speed. On the other hand, the transverse residual stress showed, on the welding, higher compressive residual stresses increasing the welding speed.
- Finally, the comparison between traditional FSW and in-process cooled FSW has been done. The results showed that the residual stresses are in general lower for the in-process cooled FSW technique compared to traditional one for both the longitudinal and transverse residual stress. Consequently, the use of mean to cool down the weld after the tool passage is positive to lower the residual stress values.

2. Residual stress in Fused deposition modelling:
    - A preliminary study on the mechanical behaviour of FDM parts has been carried out. This has been divided into two main section. In the first, the Classical Laminate Theory has been employed to describe the FDM parts behaviour, in the second, a study on tensile-impact of FDM specimens has been done. The results have proven that FDM parts show an orthotropic behaviour on both static and dynamic loads and that the CLT can predict in good manner the elastic behaviour of FDM parts under quasi-static loads. These studies were also useful to establish the appropriate behaviour of the material to employ in the residual stress calculation.
    - In order to carry out the residual stress measurement into FDM parts, an orthotropic finite element model has been developed. Through the comparison between the displacements recorded from ESPI hole-drilling and the data from the numerical model, the residual stresses could be calculated.
    - Finally, the measurement of the residual stress in FDM parts employing the ESPI hole-drilling method has been done. The effect of the stacking sequences and a comparison

between the sides of the specimen on the residual stress have been carried out. The results showed that, whereas for τ_{xy} cannot be observed any difference among the stacking sequences as well as the sides of the specimens, for σ_x and σ_y there are some differences that are remarkably near the surface of the specimens. The ± 30° stacking sequence is the worst configuration because it shows the highest values of residual stresses, on the other hand, the ± 45° should be the best configuration to have lower residual stress values. Moreover, the comparison between the top and the bottom of the specimens shows no clear differences in all configurations.

In conclusion, the results of this dissertation have shown that the residual stresses in both the studied techniques FSW and FDM can be a serious issue that influence the quality and the behaviour of the final products. Moreover, it has been shown that the use of numerical model can help to predict the residual stresses due to the change of process parameters. This allows to have a better understanding of the behaviour of the final products but also can reduce the amount of the trials and errors decreasing the costs to obtain a good final product.

Bibliography

1. Totten, G.E., *Handbook of residual stress and deformation of steel*. 2002: ASM international.
2. Withers, P. and H. Bhadeshia, *Residual stress. Part 1–measurement techniques.* Materials science and Technology, 2001. **17**(4): p. 355-365.
3. Soul, F. and N. Hamdy, *Numerical Simulation of residual stress and strain behavior after temperature modification*. 2012: INTECH Open Access Publisher.
4. Kandil, F., et al., *A review of residual stress measurement methods.* A Guide to Technique Selection, NPL, Report MATC (A), 2001. **4**.
5. Schajer, G.S. and C.O. Ruud, *Overview of Residual Stresses and Their Measurement*, in *Practical Residual Stress Measurement Methods*. 2013, John Wiley & Sons, Ltd. p. 1-27.
6. Measurements, V.M., *Measurement of residual stresses by the hole drilling strain gage method*. 2007, Tech Note TN-503-6.
7. Schajer, G.S. and T.J. Rickert, *Incremental Computation Technique for Residual Stress Calculations Using the Integral Method*, in *Experimental and Applied Mechanics, Volume 6: Proceedings of the 2010 Annual Conference on Experimental and Applied Mechanics*, T. Proulx, Editor. 2011, Springer New York: New York, NY. p. 185-191.
8. Schajer, G.S. and M.B. Prime, *Use of inverse solutions for residual stress measurements.* Journal of engineering materials and technology, 2006. **128**(3): p. 375-382.
9. ASTM, *Standard Test Method for Determining Residual Stresses by the Hole-Drilling Strain-Gage Method*, in *E837-13a*. 2013, ASTM International, West Conshohocken, PA: www.astm.org.
10. Schajer, G.S. and P.S. Whitehead, *Hole Drilling and Ring Coring*, in *Practical Residual Stress Measurement Methods*. 2013, John Wiley & Sons, Ltd. p. 29-64.
11. Nelson, D., *Residual stress determination by hole drilling combined with optical methods.* Experimental Mechanics, 2010. **50**(2): p. 145-158.
12. Focht, G. and K. Schiffner, *Determination of residual stresses by an optical correlative hole-drilling method.* Experimental mechanics, 2003. **43**(1): p. 97-104.
13. Dıaz, F., G. Kaufmann, and G. Galizzi, *Determination of residual stresses using hole drilling and digital speckle pattern interferometry with automated data analysis.* Optics and Lasers in Engineering, 2000. **33**(1): p. 39-48.
14. Schajer, G. and M. Steinzig, *Full-field calculation of hole drilling residual stresses from electronic speckle pattern interferometry data.* Experimental Mechanics, 2005. **45**(6): p. 526-532.

15. Kujawinska, M., *Use of phase-stepping automatic fringe analysis in moire interferometry.* Applied optics, 1987. **26**(22): p. 4712-4714.
16. Ghiglia, D.C. and M.D. Pritt, *Two-dimensional phase unwrapping: theory, algorithms, and software*. Vol. 4. 1998: Wiley New York.
17. Fitzpatrick, M., et al., *Determination of residual stresses by X-ray diffraction.* 2005.
18. Cullity, B.D., *Elements of X-ray Diffraction.* 2001.
19. Noyan, I.C. and J.B. Cohen, *Residual stress: measurement by diffraction and interpretation*. 2013: Springer.
20. Altenkirch, J., et al., *The effect of tensioning and sectioning on residual stresses in aluminium AA7749 friction stir welds.* Materials Science and Engineering: A, 2008. **488**(1–2): p. 16-24.
21. Pyzalla, A., *Methods and feasibility of residual stress analysis by high-energy synchrotron radiation in transmission geometry using a white beam.* Journal of Nondestructive Evaluation, 2000. **19**(1): p. 21-31.
22. Jiles, D., *Review of magnetic methods for nondestructive evaluation.* NDT international, 1988. **21**(5): p. 311-319.
23. Mishra, R.S. and Z.Y. Ma, *Friction stir welding and processing.* Materials Science and Engineering: R: Reports, 2005. **50**(1-2): p. 1-78.
24. Rhodes, C., et al., *Effects of friction stir welding on microstructure of 7075 aluminum.* Scripta materialia, 1997. **36**(1): p. 69-75.
25. Jata, K. and S. Semiatin, *Continuous dynamic recrystallization during friction stir welding of high strength aluminum alloys*. 2000, DTIC Document.
26. Mishra, R.S., et al., *High strain rate superplasticity in a friction stir processed 7075 Al alloy.* Scripta Materialia, 1999. **42**(2): p. 163-168.
27. Mishra, R.S. and M.W. Mahoney. *Friction stir processing: a new grain refinement technique to achieve high strain rate superplasticity in commercial alloys*. in *Materials Science Forum*. 2001. Trans Tech Publ.
28. Padmanaban, G. and V. Balasubramanian, *Selection of FSW tool pin profile, shoulder diameter and material for joining AZ31B magnesium alloy–an experimental approach.* Materials & Design, 2009. **30**(7): p. 2647-2656.
29. Lee, W.-B. and S.-B. Jung, *The joint properties of copper by friction stir welding.* Materials Letters, 2004. **58**(6): p. 1041-1046.
30. Fernández, J.R. and A.J. Ramirez. *Dissimilar friction stir welding of steel to Ni-based alloy 625-Butt and lap joints*. in *The Twenty-third International Offshore and Polar Engineering Conference*. 2013. International Society of Offshore and Polar Engineers.

31. Bagheri, A., T. Azdast, and A. Doniavi, *An experimental study on mechanical properties of friction stir welded ABS sheets.* Materials & Design, 2013. **43**: p. 402-409.
32. Farias, A., et al., *Tool wear evaluations in friction stir processing of commercial titanium Ti–6Al–4V.* Wear, 2013. **302**(1): p. 1327-1333.
33. Khodir, S., et al., *Microstructures and mechanical properties evolution during friction stir welding of SK4 high carbon steel alloy.* Materials Science and Engineering: A, 2012. **558**: p. 572-578.
34. Liu, P., et al., *Microstructure and XRD analysis of FSW joints for copper T2/aluminium 5A06 dissimilar materials.* Materials letters, 2008. **62**(25): p. 4106-4108.
35. Kohn, G., et al., *Laser-assisted friction stir welding.* Welding journal, 2002. **81**(2): p. 46-48.
36. Gibson, B., et al., *Friction stir welding: process, automation, and control.* Journal of Manufacturing Processes, 2014. **16**(1): p. 56-73.
37. Schmidt, H.B. and J.H. Hattel, *Thermal modelling of friction stir welding.* Scripta Materialia, 2008. **58**(5): p. 332-337.
38. Schmidt, H., J. Hattel, and J. Wert, *An analytical model for the heat generation in friction stir welding.* Modelling and Simulation in Materials Science and Engineering, 2004. **12**(1): p. 143.
39. Padhy, G., C. Wu, and S. Gao, *Auxiliary energy assisted friction stir welding–status review.* Science and Technology of Welding and Joining, 2015. **20**(8): p. 631-649.
40. Zhang, H., H. Liu, and L. Yu, *Effect of water cooling on the performances of friction stir welding heat-affected zone.* Journal of materials engineering and performance, 2012. **21**(7): p. 1182-1187.
41. Fratini, L., G. Buffa, and R. Shivpuri, *Mechanical and metallurgical effects of in process cooling during friction stir welding of AA7075-T6 butt joints.* Acta Materialia, 2010. **58**(6): p. 2056-2067.
42. Liu, X., S. Lan, and J. Ni, *Experimental study of Electro-Plastic Effect on Advanced High Strength Steels.* Materials Science and Engineering: A, 2013. **582**: p. 211-218.
43. Kopanev, A.A., *The nature of the electroplastic effect in metals.* Strength of Materials, 1991. **23**(1): p. 55-59.
44. Okazaki, K., M. Kagawa, and H. Conrad, *A study of the electroplastic effect in metals.* Scripta Metallurgica, 1978. **12**(11): p. 1063-1068.
45. Long, X. and S.K. Khanna, *Modelling of electrically enhanced friction stir welding process using finite element method.* Science and Technology of Welding and Joining, 2005. **10**(4): p. 482-487.

46. Potluri, H., J.J. Jones, and L. Mears. *Comparison of electrically-assisted and conventional friction stir welding processes by feed force and torque*. in *ASME 2013 International Manufacturing Science and Engineering Conference collocated with the 41st North American Manufacturing Research Conference*. 2013. American Society of Mechanical Engineers.

47. Pitschman, M., et al. *Application of electric current in friction stir welding*. in *ASME 2010 International Manufacturing Science and Engineering Conference*. 2010. American Society of Mechanical Engineers.

48. Fratini, L., G. Buffa, and R. Shivpuri, *In-process heat treatments to improve FS-welded butt joints.* The International Journal of Advanced Manufacturing Technology, 2008. **43**(7): p. 664.

49. Sabari, S.S., S. Malarvizhi, and V. Balasubramanian, *Influences of tool traverse speed on tensile properties of air cooled and water cooled friction stir welded AA2519-T87 aluminium alloy joints.* Journal of Materials Processing Technology, 2016. **237**: p. 286-300.

50. Reynolds, A.P., et al., *Structure, properties, and residual stress of 304L stainless steel friction stir welds.* Scripta Materialia, 2003. **48**(9): p. 1289-1294.

51. Peel, M., et al., *Microstructure, mechanical properties and residual stresses as a function of welding speed in aluminium AA5083 friction stir welds.* Acta Materialia, 2003. **51**(16): p. 4791-4801.

52. Prime, M., et al., *Residual stress measurements in a thick, dissimilar aluminum alloy friction stir weld.* Acta Materialia, 2006. **54**(15): p. 4013-4021.

53. Darvazi, A.R. and M. Iranmanesh, *Prediction of asymmetric transient temperature and longitudinal residual stress in friction stir welding of 304L stainless steel.* Materials & Design, 2014. **55**: p. 812-820.

54. Xu, W., et al., *Temperature evolution, microstructure and mechanical properties of friction stir welded thick 2219-O aluminum alloy joints.* Materials & Design, 2009. **30**(6): p. 1886-1893.

55. Hwang, Y.-M., et al., *Experimental study on temperature distributions within the workpiece during friction stir welding of aluminum alloys.* International Journal of Machine Tools and Manufacture, 2008. **48**(7-8): p. 778-787.

56. Maeda, M., et al., *Temperature Field in the Vicinity of FSW-Tool During Friction Stir Welding of Aluminium Alloys.* Welding in the World, 2005. **49**(3): p. 69-75.

57. Song, M. and R. Kovacevic, *Thermal modeling of friction stir welding in a moving coordinate system and its validation.* International Journal of Machine Tools and Manufacture, 2003. **43**(6): p. 605-615.

58. *ANSYS® Academic Research Release 16.2 Users' Manual*. Swanson Analysis System Inc.

59. Chao, Y.J., X. Qi, and W. Tang, *Heat transfer in friction stir welding—experimental and numerical studies.* Journal of manufacturing science and engineering, 2003. **125**(1): p. 138-145.

60. Khanna, S.K., et al., *Residual stresses in spot welded new generation aluminium alloys Part A–thermophysical and thermomechanical properties of 6111 and 5754 aluminium alloys.* Science and Technology of Welding & Joining, 2013.

61. Donne, C.D., et al. *Investigations on residual stresses in friction stir welds*. in *3Õrd International Symposium on Friction Stir Welding*. 2001.

62. Sutton, M., et al., *A study of residual stresses and microstructure in 2024-T3 aluminum friction stir butt welds.* Journal of Engineering Materials and Technology, 2002. **124**(2): p. 215-221.

63. Khandkar, M.Z.H., et al., *Predicting residual thermal stresses in friction stir welded metals.* Journal of Materials Processing Technology, 2006. **174**(1): p. 195-203.

64. Chen, C. and R. Kovacevic, *Finite element modeling of friction stir welding—thermal and thermomechanical analysis.* International Journal of Machine Tools and Manufacture, 2003. **43**(13): p. 1319-1326.

65. Kalpakjian, S., *Manufacturing engineering and technology*. 2001: Pearson Education India.

66. Caulfield, B., P.E. McHugh, and S. Lohfeld, *Dependence of mechanical properties of polyamide components on build parameters in the SLS process.* Journal of Materials Processing Technology, 2007. **182**(1–3): p. 477-488.

67. Chua, C.K., S.M. Chou, and T.S. Wong, *A study of the state-of-the-art rapid prototyping technologies.* The International Journal of Advanced Manufacturing Technology, 1998. **14**(2): p. 146-152.

68. Yan, X. and P. Gu, *A review of rapid prototyping technologies and systems.* Computer-Aided Design, 1996. **28**(4): p. 307-318.

69. Ziemian, C., M. Sharma, and S. Ziemi, *Anisotropic Mechanical Properties of ABS Parts Fabricated by Fused Deposition Modelling.* 2012.

70. Bellehumeur, C., et al., *Modeling of bond formation between polymer filaments in the fused deposition modeling process.* Journal of Manufacturing Processes, 2004. **6**(2): p. 170-178.
71. Ahn, S.-H., et al., *Anisotropic material properties of fused deposition modeling ABS.* Rapid Prototyping Journal, 2002. **8**(4): p. 248-257.
72. Stephens, B., et al., *Ultrafine particle emissions from desktop 3D printers.* Atmospheric Environment, 2013. **79**(0): p. 334-339.
73. Zein, I., et al., *Fused deposition modeling of novel scaffold architectures for tissue engineering applications.* Biomaterials, 2002. **23**(4): p. 1169-1185.
74. Zhong, W., et al., *Short fiber reinforced composites for fused deposition modeling.* Materials Science and Engineering: A, 2001. **301**(2): p. 125-130.
75. Allahverdi, M., et al., *Processing of advanced electroceramic components by fused deposition technique.* Journal of the European Ceramic Society, 2001. **21**(10–11): p. 1485-1490.
76. Promakhov, V., et al., *On the possibility to fabricate ceramics using fused deposition modeling.* AIP Conference Proceedings, 2016. **1772**(1): p. 030003.
77. Mireles, J., et al., *Development of a Fused Deposition Modeling System for Low Melting Temperature Metal Alloys.* Journal of Electronic Packaging, 2013. **135**(1): p. 011008-011008.
78. Mireles, J., et al., *Fused deposition modeling of metals.* 2013.
79. Masood, S.H. and W.Q. Song, *Development of new metal/polymer materials for rapid tooling using Fused deposition modelling.* Materials & Design, 2004. **25**(7): p. 587-594.
80. Novakova-Marcincinova, L., et al. *Special materials used in FDM rapid prototyping technology application*. in *2012 IEEE 16th International Conference on Intelligent Engineering Systems (INES)*. 2012.
81. Mohamed, O.A., S.H. Masood, and J.L. Bhowmik, *Optimization of fused deposition modeling process parameters: a review of current research and future prospects.* Advances in Manufacturing, 2015. **3**(1): p. 42-53.
82. Gibson, I., D. Rosen, and B. Stucker, *Additive manufacturing technologies: 3D printing, rapid prototyping, and direct digital manufacturing*. 2014: Springer.
83. Pandey, P.M., N.V. Reddy, and S.G. Dhande, *Real time adaptive slicing for fused deposition modelling.* International Journal of Machine Tools and Manufacture, 2003. **43**(1): p. 61-71.

84. Kantaros, A. and D. Karalekas, *Fiber Bragg grating based investigation of residual strains in ABS parts fabricated by fused deposition modeling process.* Materials & Design, 2013. **50**: p. 44-50.

85. Lee, B.H., J. Abdullah, and Z.A. Khan, *Optimization of rapid prototyping parameters for production of flexible ABS object.* Journal of Materials Processing Technology, 2005. **169**(1): p. 54-61.

86. Anitha, R., S. Arunachalam, and P. Radhakrishnan, *Critical parameters influencing the quality of prototypes in fused deposition modelling.* Journal of Materials Processing Technology, 2001. **118**(1–3): p. 385-388.

87. Sood, A.K., R.K. Ohdar, and S.S. Mahapatra, *Parametric appraisal of mechanical property of fused deposition modelling processed parts.* Materials & Design, 2010. **31**(1): p. 287-295.

88. Lee, C.S., et al., *Measurement of anisotropic compressive strength of rapid prototyping parts.* Journal of Materials Processing Technology, 2007. **187–188**(0): p. 627-630.

89. Croccolo, D., M. De Agostinis, and G. Olmi, *Experimental characterization and analytical modelling of the mechanical behaviour of fused deposition processed parts made of ABS-M30.* Computational Materials Science, 2013. **79**(0): p. 506-518.

90. Casavola, C., et al., *Preliminary Study on Residual Stress in FDM Parts*, in *Residual Stress, Thermomechanics & Infrared Imaging, Hybrid Techniques and Inverse Problems, Volume 9*. 2017, Springer International Publishing. p. 91-96.

91. Nelson, D.V., *Optical Methods*, in *Practical Residual Stress Measurement Methods*. 2013, John Wiley & Sons, Ltd. p. 279-302.

92. Turnbull, A., A.S. Maxwell, and S. Pillai, *Residual stress in polymers - evaluation of measurement techniques.* Journal of Materials Science, 1999. **34**(3): p. 451-459.

93. Nau, A., et al., *Application of the hole drilling method for residual stress analyses in components made of polycarbonate.* Zeitschrift Kunststofftechnik/Journal of Plastics Technology, 2011(3): p. 66-85.

94. Magnier, A., A. Nau, and B. Scholtes. *Some aspects of the application of the hole drilling method on plastic materials*. in *Conference Proceedings of the Society for Experimental Mechanics Series*. 2016.

95. Zhang, Y. and Y. Chou, *Three-dimensional finite element analysis simulations of the fused deposition modelling process.* Proceedings of the Institution of Mechanical Engineers, Part B: Journal of Engineering Manufacture, 2006. **220**(10): p. 1663-1671.

96. Akbari, S., F. Taheri-Behrooz, and M.M. Shokrieh, *Characterization of residual stresses in a thin-walled filament wound carbon/epoxy ring using incremental hole drilling method.* Composites Science and Technology, 2014. **94**: p. 8-15.